Title

Synthesis, Postmodification, Metalation, and Gas Adsorption in Chemically Stable Metal Organic Frameworks and Zeolitic Imidazolate Frameworks.

Author
Morris, William

Publication Date
2012

UNIVERSITY OF CALIFORNIA
LOS ANGELES

Synthesis, Postmodification, Metalation, and Gas Adsorption in Chemically Stable Metal Organic Frameworks and Zeolitic Imidazolate Frameworks.

A dissertation in partial satisfaction of the
Requirements for the degree Doctor of Philosophy
in Chemistry.

by
William Morris

2012

ABSTRACT OF THE DISSERTATION

Synthesis, Postmodification, Metalation, and Gas Adsorption in Chemically Stable Metal Organic Frameworks and Zeolitic Imidazolate Frameworks

By

William Morris

Doctor of Philosophy in Chemistry

University of California, Los Angeles, 2012

Professor Omar M. Yaghi, Chair

Metal Organic Frameworks (MOFs) and Zeolitic Imidazolate Frameworks (ZIFs) are porous crystalline materials comprised of organic units (links) and metal oxide units (secondary building units) with surface areas often exceeding 1000 m^2/g. These materials are finding increased applications in gas storage, gas separation, and catalysis. In this thesis new MOFs and ZIFs are synthesized to further these applications. Special attention is paid to the synthesis of frameworks, which can be postsynthetically modified with new functionalities including metal centers. Design metrics for postmodification are realized, including pore size, chemical stability, and incorporation of metalation sites into frameworks. Finally, enhancement of gas adsorption across a series of frameworks is investigated.

The dissertation of William Morris is approved.

Miguel A. Garcia Garibay

Richard B. Kaner

Yong Chen

Omar M. Yaghi, Committee Chair

University of California, Los Angeles

Table of Contents

List of tables

List of Figures and Schemes

Figures

Schemes

Acknowledgements

There are so many people to thank; it is hard to know where to start. I would like to first thank all the Yaghi group members, both senior and junior to me, in my five years there has been over forty different members. Dr Rahul Banerjee, Dr David Tranchmontage, and Dr Christian Doonan for, helping me solve my first crystal structures, making my first MOF, and everything else in between, respectively. I thank Hiro for staying in the lab longer than me, preparing grant reports, paper editing, and general advice which was priceless. I thank Joe Hunt, Qiaowei, Yongok, Anh, Fernando, Jon Brown, Kyle Cordova, Grant, Bo, Caitlin, Parisa Mahjoor, Zheng Lu, Jeremy, Kenichi Hamada, Felipe Gandara, Dani Peri, Adam Duong, Mitsuharu Suzuki and Rong Ye for taking coffee breaks and with some of you the many coffee breaks we took. I would like to thank the people I have mentored including Belinda, Jon, Caitlin, Selcuk, Kelvin, and Boris, you helped me more than I imagine I helped you in synthesizing and characterizing many reactions. Thank you to Dr. Carolyn Knobler for diligently reading everything I have written, never getting mad at my terrible grammar. A special acknowledgement to the lab safety tsars David Britt, DJ, and Lisa, for their excellent safety standards; keeping lab safety out of my hands for five years.

I would like to thank my advisor; Professor Yaghi with out you this work would of not been possible. You have provided me with constant support over the five-year period, but also encouraging me to be independent. You have given me many opportunities including travel, paper writing, and working with collaborators. You have even pushed me into several opportunities I did not want at the time including, grant reporting and presentations in front of funding bodies, which with the benefit of hindsight

I know will make me a better independent researcher. I would like to thank my committee members Professor Kaner, Professor Garcia-Garibay, and Professor Chen.

I would like to thank my collaborators who I have worked on many projects with producing several papers, many presentations, and grant reports. As part of the EFRC-UCLA I have had the privilege to work with Professor Laird (Kansas), Dr Ning He (Kansas), Professor Asta (Berkeley), Keith Ray, and many others. I would also like to thank Dongwhan Lee (Indiana) and all the people at ECBC including ex lab alumni Grant Glover for help with the many DTRA projects we worked on. I would like to thank Psaras Mcgrier and Sir Fraser Stoddart for help with intricate organic synthesis I would of struggled and probably failed to tackle alone.

I thank my family (mum, dad, sister, and brother) and my extended family, for their constant support never holding me back, wonderful family holidays, and weekly skype conservations. Finally I thank my fiancée, Ellen, for her constant support, rides to school, acceptance of my long hours, many movies watched, and nights out.

Thank you,

VITA

2007 **Manchester University**
M.S in Chemistry

Publications:

Crystals as Molecules: Postsynthesis Covalent Functionalization of Zeolitic Imidazolate Frameworks, W. Morris, C. Doonan, H. Furukawa, R. Banerjee, O. M. Yaghi, *J. Am. Chem. Soc.*, **2008**, *130*, 12626-12627.

Isoreticular Metalation of Metal-Organic Frameworks, C. J. Doonan, W. Morris, H. Furukawa, and O. M. Yaghi, *J. Am. Chem. Soc.,* **2009**, *131*, 9492-9493.

A Combined Experimental - Computational Investigation of Carbon Dioxide Capture in a Series of Isoreticular Zeolitic Imidazolate Frameworks, W. Morris, B. Leung, H. Furukawa, O. K. Yaghi, N. He, H. Hayashi, Y. Houndonougbo, M. Asta, B. B. Laird, O. M. Yaghi, *J. Am. Chem. Soc.*, **2010**, *132*, 11006–11008.

Postsynthetic Modification of a Metal-Organic Framework for Stabilization of a Hemiaminal and Ammonia Uptake, W. Morris, C. J. Doonan, O. M. Yaghi, *Inorg. Chem.*, **2011**, *50*, 6853-6855.

Framework Mobility in the Metal-Organic Framework Crystal IRMOF-3: Evidence for Aromatic Ring and Amine Rotation, W. Morris, R. E. Taylor, C. Dybowski, O. M. Yaghi, M. A. Garcia-Garibay, *J. Mol. Struct.*, **2011, *1004*, 94-10.**

Synthesis, Structure, and Metalation of Two New Highly Porous Zirconium Metal-Organic Frameworks, W. Morris, B. Volosskiy, S. Demir, F. Gándara, P. L. McGrier, H. Furukawa, D. Cascio, J. F. Stoddart, O. M. Yaghi, *Inorganic Chemistry*, **2012**, *51*, 6443-6445.

NMR and X-ray Study Revealing the Rigidity of Zeolitic Imidazolate Frameworks, W. Morris, C. J. Stevens, R. E. Taylor, C. Dybowski, O. M. Yaghi, M. A. Garcia-Garibay, *J. Phys. Chem. C*, **2012**, 116, 13307−13312.

Patents:

Porous reactive frameworks Yaghi, Omar M.; Czaja, Alexander U.; Morris, William; Hunt, Joseph R.; Britt, David Kyle; Lee, Chain. PCT Int. Appl. (2010).

Organo-metallic frameworks and methods of making same Doonan, Christian J.; Morris, William; Yaghi Omar M.; Wang, Bo; Deng, Hexiang. PCT Int. Appl. (2010).

Oral Presentations:

Metal organic frameworks (MOFs) for uptake and breakdown of harmful gases, Morris, William; Yaghi, Omar M. **CBD S&T Conference**, Orlando, Fl, November 2010

Understanding gas adsorption in Zeolitic Imidazolate Frameworks, Morris, William; Leung, Belinda; He, Ning; Ray, Keith; Houndonougbo, Yao; Laird, Brian B.; Asta, Mark; Yaghi, Omar M, **241st ACS National Meeting & Exposition**, Anaheim, CA, United States, March 2011

Metalation of Metal Organic Frameworks (MOFs) , Morris, William; Yaghi, Omar M. **Materials Chemistry 10 (MC10),** University of Manchester, UK, July 2011

Ammonia adsorption in metal organic frameworks, William Morris, Selcuk Demir, Boris Volosskiy, Jon Brown, Omar M. Yaghi **, Chemical/Biological Filtrations strategies workshop**, Arlington, VA, September 2011

Metalation of Metal Organic Frameworks (MOFs) – Metalation of a Zirconium based metal organic framework, Morris, William; Yaghi, Omar M. **EFRC annual review on carbon capture technologies,** Berkeley, CA, September 2011

Expanding the chemistry of Zirconium based métal-organic frameworks, Morris, William; Yaghi, Omar M. **EFRC research seminar,** Berkeley, CA, June 2012

Poster Presentations:

Synthesis of three highly chemically stable zirconium based porphyrin MOFs Morris, William; Yaghi, Omar M. **Gordon Research seminar in Crystal Enginnering**, Wattervalley, NH, United States, June 2012.

Highly stable zirconium based metal organic frameworks (MOFs) for uptake and breakdown of harmful gases, Morris, William; Yaghi, Omar M. **CBD S&T Conference**, Las Vegas, NV, November 2011

BORGs and robust dynamics Morris, William; Deng, Hexiang; Yaghi, Omar M. **FENA annual review**, UCLA, January 2010.

Incorporation of metal centers into a porous metal organic framework chemistry, Morris, William; Doonan, Christian J.; Yaghi, Omar M. **Gordon Research seminar in inorganic chemistry**, University of New England in Biddeford, ME, United States, June 2010.

Crystals as molecules: Isoreticular functionalization of zeolitic imidazolate frameworks Morris, William; Doonan, Christian J.; Yaghi, Omar M. Abstracts of Papers, **237th ACS National Meeting, Salt Lake City**, UT, United States, March 22-26, 2009 2009

Chapter One

Introduction

Metal-organic frameworks (MOFs) and zeolitic imidazolate frameworks (ZIFs) are expanding classes of crystalline porous materials constructed from metal oxide units and organic units, typically in a solvothermal reaction.[1] The porous nature of these frameworks can be measured after removal of solvents to yield an activated MOF, and some MOFs now have surface areas exceeding 10,000 m^2/g (BET).[2] Often coupled with their high porosity is their high thermal stability; these materials are stable to 500 ˚C before framework degradation.[3] The potential applications of these frameworks are numerous and include gas adsorption, catalysis, drug delivery, and sensors.[4-7]

Other porous materials, including amorphous carbons and zeolites, are currently limited in their possibilities for synthetic expansion. Structural resolution of amorphous carbons remains a problem due to a lack of long-range order, and building blocks for zeolite synthesis remain limited.[8,9] However, MOF frameworks do not suffer from these limitations. There is a wide array of organic units and metal centers that can be incorporated into MOFs, an incredibly diverse range of materials that is rapidly growing in numbers, and they do not suffer from the limitations of other porous materials in the expansion of the class. MOFs are only limited by the organic links that can be synthesized and the metal oxide units with which they can be combined to make new frameworks. For example, when considering the zinc cluster $Zn_4O(-CO_2)_6$, one of over ten zinc clusters reported, in combination with a bidentate and a tridentate link, different MOFs, MOF-5 and MOF-177, with **pcu** and **qom** topologies, respectively, are obtained

(**Scheme 1A**).[1, 10-12] These frameworks can be further expanded by applying two basic principles, isoreticular modification and expansion.[2,13] Firstly, isoreticular modification is used to append different functionalities to the organic unit; this has been highlighted in the IRMOF series, where over twenty modifications have been reported (**Scheme 1B**).[13] Isoreticular modification has been used to enhance gas adsorption properties of a MOF and to make MOFs suitable for postmodification.[14-15] By expanding the length of the organic unit, isoreticular expansion, pore size and surface area can be enhanced (**Scheme 1C**).[2] Isoreticular modification and expansion can be applied to any MOF, and therefore this area has seen rapid expansion in recent years. Furthermore, unlike the case of amorphous carbons, the structure determination is possible for these frameworks due to the crystallinity that arises from the regular order of the MOF backbone.

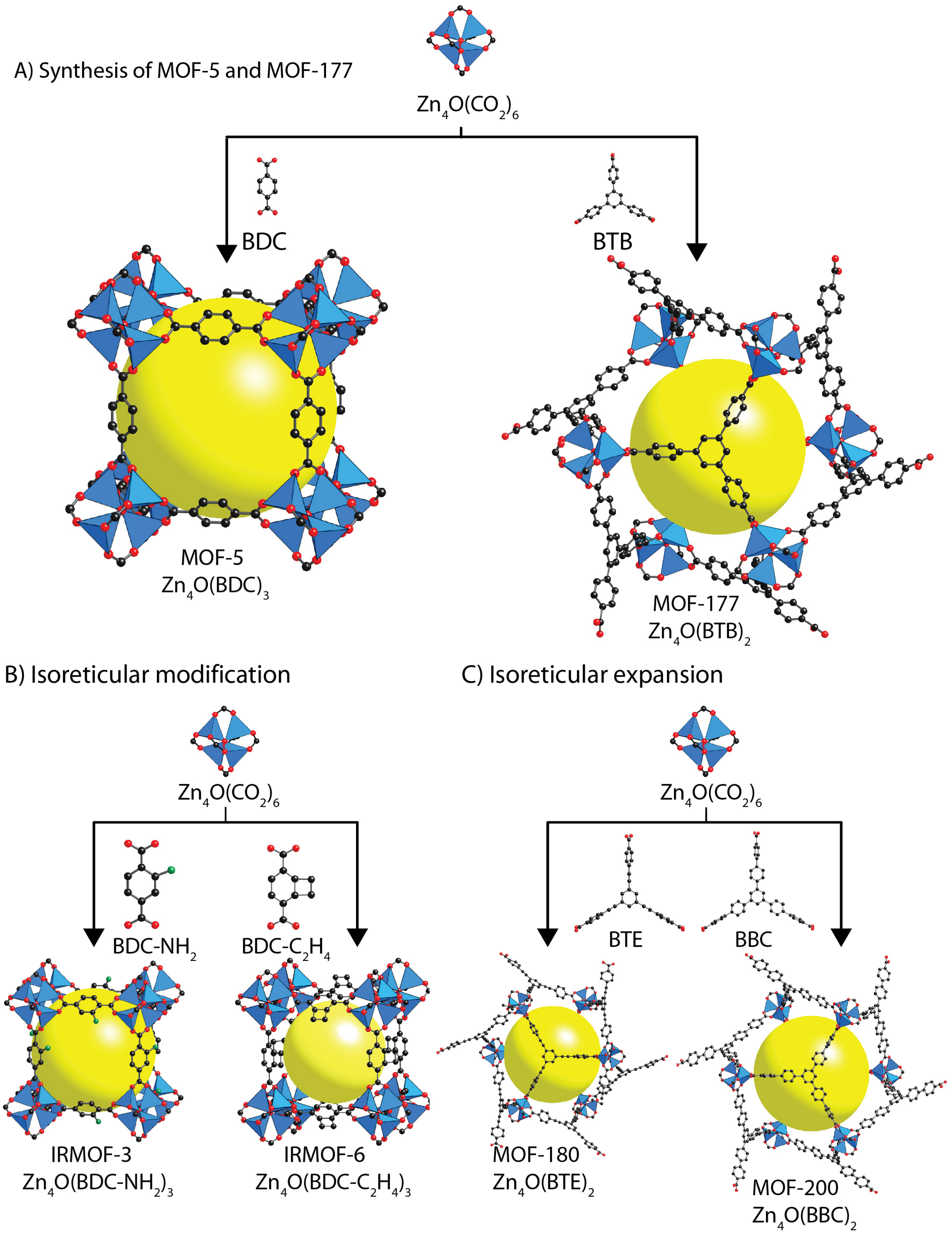

Scheme 1) A) Synthesis of MOF-5 and MOF-177.[11-12] B) Isoreticular modification of MOF-5.[13] C) Isoreticular expansion of MOF-177.[2]

A key limitation in the choice of MOFs is the solvothermal method that is used in their synthesis. Solvothermal synthesis limits the types of organic functionalities and the metal centers that can be incorporated into the MOF to those compatible with the synthetic techniques. To overcome the limitations of solvothermal synthesis, we have sought to carry out organic chemistry synthetic methods in the solid state. Organic covalent modifications in extended materials remain relatively limited, especially when contrasted with the organic chemistry of small molecules in solution. The chemistry of organic molecules in solution has been developed over several centuries, and new unique organic transformations are being reported every day. One key challenge is the adaptation of this great range of organic chemistry synthesis techniques to the solid state; porous MOFs offer for this purpose an ideal heterogeneous interface between a solution containing reactants and a solid-state material. This process has been termed postmodification, and, if successful, it proceeds in a topotactic manner with retention of porosity and crystallinity.[15] The first example of covalent modification was reported in 2007 when IRMOF-3 was modified with acetic anhydride, to form an alkylated amine (**Scheme 2**).[17] Development of this chemistry will be key in overcoming the limitations of solvothermal synthesis, allowing the deployment of MOF and ZIFs in an ever increasing range of applications.

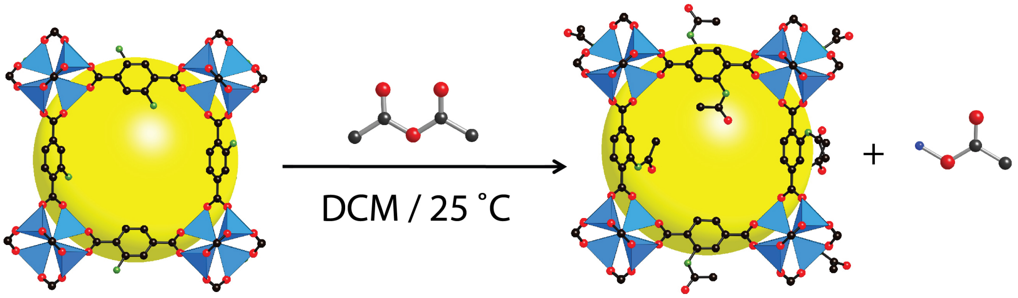

Scheme 2) Postmodification of IRMOF-3 with acetic anhydride.

In addition to postmodification, a second approach, the use of organic links with predefined metal binding sites, is taken to incorporate additional metal centers into MOFs. Although limited by the harsh conditions of solvothermal synthesis, several units have been identified including bipyridine and porphyrin units that are compatible with this synthesis and that also contain metal binding sites (**Figure 1A**).[18-19] We chose to utilize the porphyrin-based unit with its square planar metal binding unit as a suitable motif to bind metals. This unit has been successfully incorporated into many MOFs; however, these MOFs often have 2-D non-porous structures with low chemical stability; this limits their applications in catalysis and gas adsorption (**Figure 1B**).[20-21] We have identified porphyrin binding units with multiple points of extension, and have successfully synthesized highly chemically stable 3-D MOFs. Coupled with exceptional chemical stability, these MOFs have the largest pores and surface areas for porphyrin-containing MOFs.

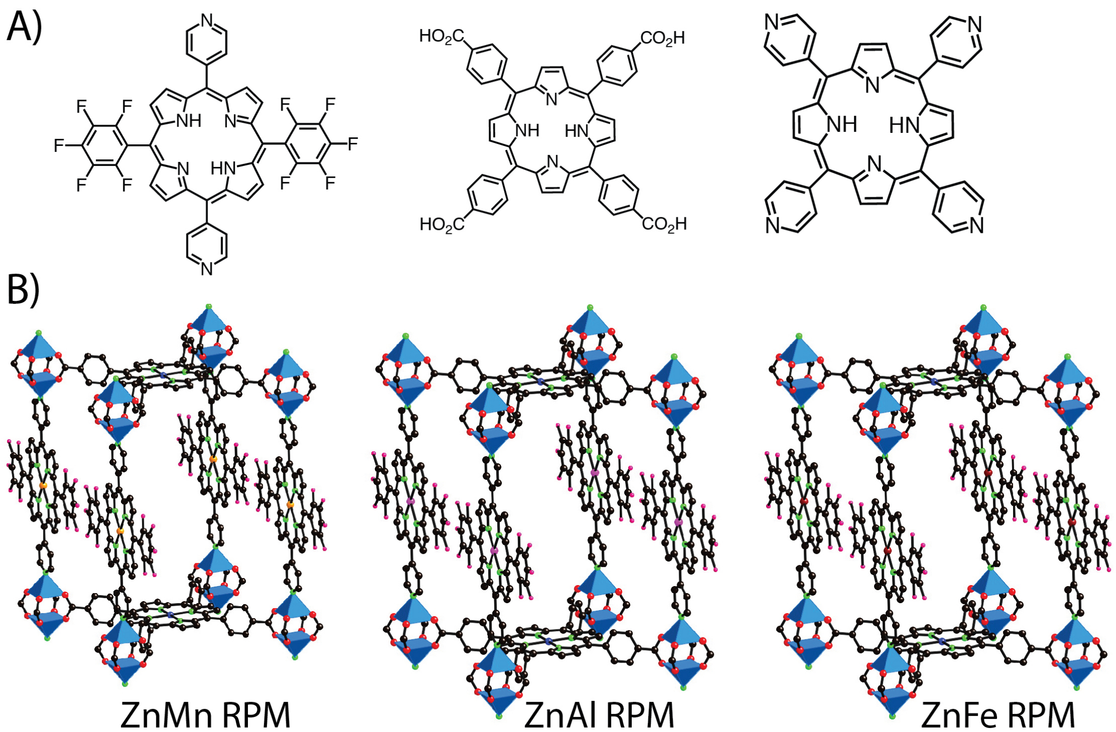

Figure 1) A) Porphyrin containing organic links. B) Zinc based porphyrin contain MOFs.[19]

Within this dissertation, new techniques including postmodification, metalation, and choice of metal chelating ligand have been discussed. These developments will lead to enhancement of the functionality in MOFs and ZIFs, which will allow these substances to be considered for targeted applications in gas adsorption and catalysis. Therefore, a wide range of new MOFs and ZIFs have been synthesized that are amenable to postmodification and metalation. These frameworks have been successfully modified by postmodification and, where applicable, metalated. In doing so, many factors have been considered, including chemical stability, pore structure, and surface area.

To utilize a full range of postmodification and metalation reactions one must consider the chemical stability of the framework being used, because degradation of that structure during the reaction would make any chemical modification of no use. One weakness of zinc-based MOFs is their lack of chemical stability; they lose their structures when exposed to water and certain organic solvents. However, ZIFs have been shown to be highly chemically stable; ZIF-8 maintains crystallinity and porosity in a wide range of chemical environments.[3] In addition, a series of zirconium MOFs with the **fcu** topology were reported, designed around a chemically stable zirconium unit $Zr_6(OH)_4O_4(-CO_2)_{12}$ and terephalate units (**Figure 2**).[22] High chemical stability of MOFs and ZIFs is of prime importance, since this will allow a more diverse set of reactions to be employed.

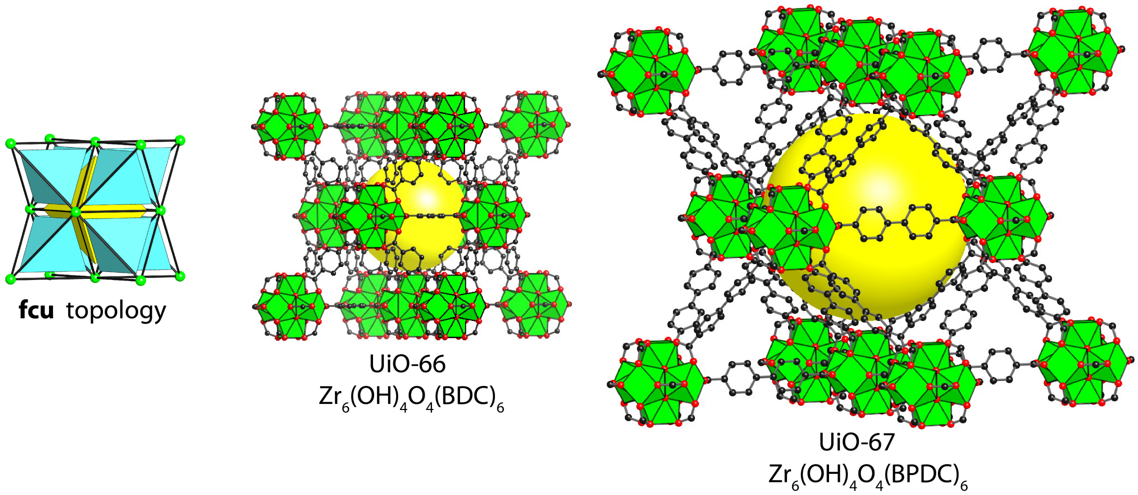

Figure 2) The **fcu** topology and series of UiO-66 MOFs.[22]

Thousands of MOF structures have been reported. MOFs with high gas adsorption will have a high surface area and specific interactions between the framework and the target gas. Organic functionalities offer sites of specific interaction through hydrogen bonding and dipole interactions, shown to enhance gas adsorption in MOFs and ZIFs.[2] Open metal sites have been shown to enhance CO_2 adsorption; Mg-MOF-74, a MOF that incorporates an open magnesium site, has record breaking CO_2 adsorption.[23] Synthesis of frameworks that contain open metal sites is often serendipitous. Incorporation of new functionalities beyond those reported in MOFs is limited by the potential instability caused by the solvothermal reaction. Postmodification offers the ability to incorporate new metal centers and organic functionalities into MOFs by targeted synthetic routes instead of relying on a serendipitous discovery.

Chapter 1 describes the synthesis and postmodification of ZIF-90, a highly chemically stable ZIF with the **sod** topology. This ZIF is appended with aldehyde functionalities suitable for postmodification (**Scheme 3A**). Two reactions are carried out on the ZIF, reduction of the aldehyde and an imine condensation reaction (**Scheme 3A**). Both of these reactions proceeded in high yields and with maintenance of crystallinity as evidenced by solid state NMR and powder X-ray diffraction (PXRD), respectively. This example of postmodifcation of ZIF-90 is the first example of postmodification in a ZIF. By utilizing a ZIF with high chemical stability, a wider range of postmodification reactions could be carried out with retention of crystallinity and porosity. However, a key limitation was observed; pore blocking was observed upon postmodification with an amine. Pore blocking prevents applications in catalysis, gas adsorption, and drug delivery.

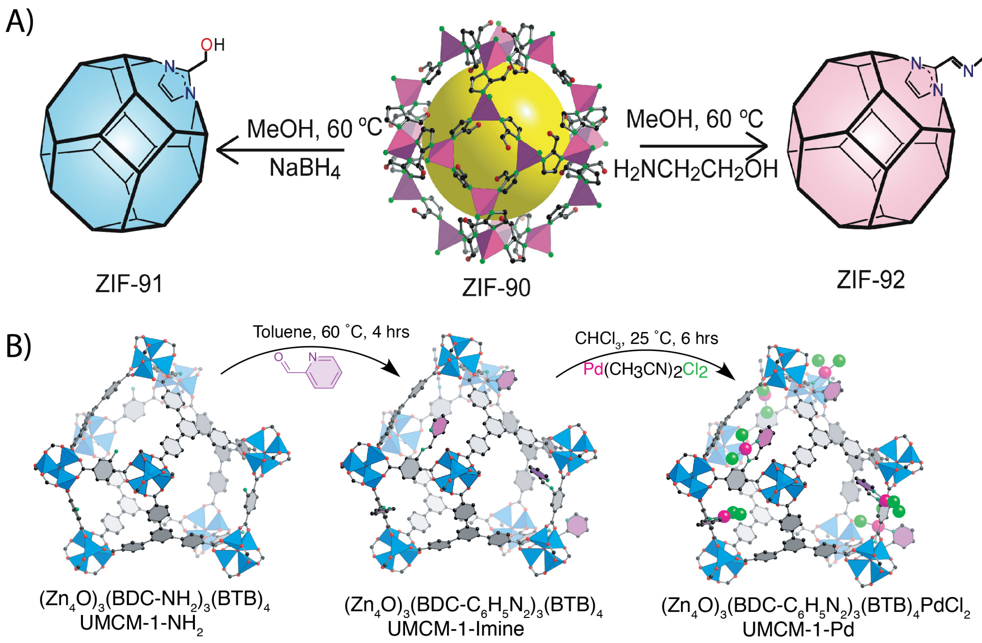

Scheme 3) A) postmodification of ZIF-90. B) Metalation of UMCM-1-NH_2

To overcome the problems related to pore size, in chapter two we describe the synthesis of a MOF with pores over two nanometers large, UMCM-1-NH_2.[24] This MOF with large pores and amine functionalities is ideal for postmodification. We chose to incorporate metal centers via postmodification into UMCM-1-NH_2; previous attempts to metalate a MOF via postmodification resulted in pore blockage.[25] A two-step postmodification process was used to quantitatively metalate UMCM-1-NH_2 with palladium centers (**Scheme 3B**). The palladium complex was concisely characterized by X-ray absorption techniques. A small reduction in crystallinity was observed upon postmodification, highlighting the weakness of this hydrolytically unstable framework in postmodification applications.

Chapters one and two emphasized the need for larger pored MOFs with high chemical stability for postmodification, if potential applications are to be realized.

Recently, a report of a highly hydrolytically stable MOF was reported, UiO-66; this MOF is comprised of terephthalic acid and a metal oxide unit ($Zr_6(OH)_4O_4(CO_2)_{12}$. UiO-66 is not suitable for postmodification, as it contains no additional organic functionalities. In chapter three, the use of isoreticular expansion for the synthesis of a framework with the highly chemically stable zirconium metal oxide unit and aminoterephalic acid for postmodification is described. This framework has been postmodified with acetyl aldehyde to form hemiaminal and aziridine functionalities; reactions have been characterized by ^{15}N solid state NMR. Yields of the reactions have been determined by direct excitation ^{15}N NMR. In addition, the ammonia adsorption of these frameworks was investigated because of their high chemical stability. Ammonia adsorption in MOFs has previously led to loss of crystallinity and structure; however, in these highly chemically stable frameworks reversible ammonia adsorption was observed with maintenance of crystallinity and porosity (**Figure 3**).

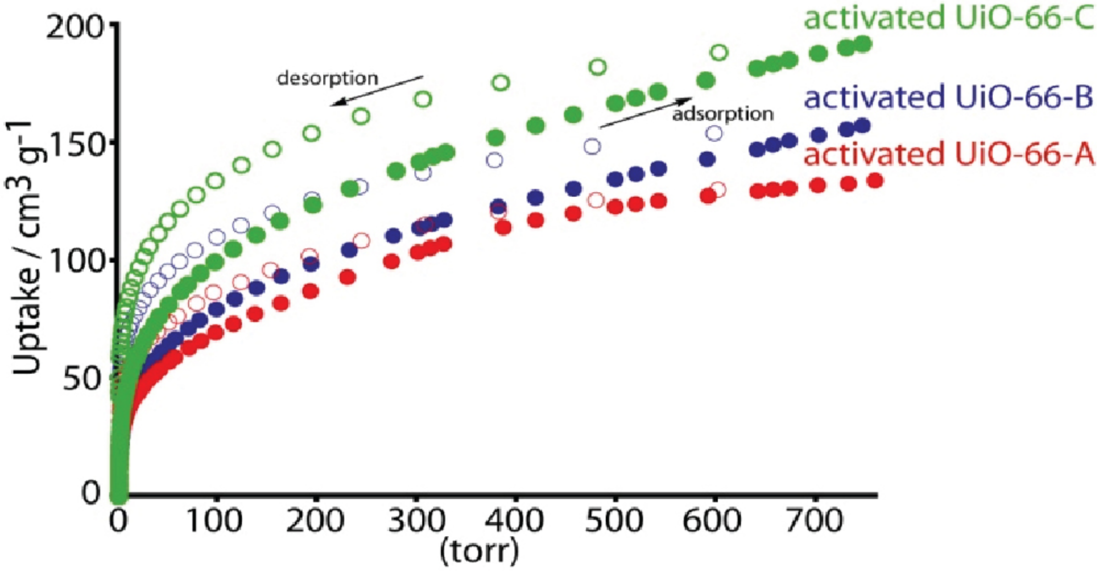

Figure 3) Ammonia adsorption at 298 K in UiO-66-A, UiO-66-B, and UiO-66-C.

The **fcu** topology of UiO-66 is found to interpenetrate when the pores exceed 10 Å in size.[26] This limits the potential of the topology for postmodification and metalation. Therefore, in chapter four we describe the discovery of new zirconium based topologies suitable for metalation. To prepare such a zirconium MOF we selected an organic link, tetracarboxyphenylporphyrin (H_4-TCPP-H_2) with four points of extension; varying the points of extension has often led to the formation of new MOF topologies. In addition, H_4-TCPP-H_2 offers a pre-defined metal binding site within the porphyrin unit; the site has a high affinity for many metals but not for zirconium. Three new MOFs were isolated when zirconium was combined with H_4-TCPP-H_2, MOF-525, MOF-545, and MOF-565 with the **ftw**, **csq**, and **she** topology (**Scheme 4**). Synthesis of three topologies was possible because zirconium adopts three different cluster shapes, cubeoctahedra, cubes, and hexagons in the **ftw**, **csq**, and **she** topology, respectively. MOF-525 has the highest surface area reported for a zirconium based MOF, and MOF-545 has the largest pores, 36 Å in diameter, for a zirconium based MOF. Record breaking surface area, pore size, chemical stability and free porphyrin metal binding sites made these frameworks ideal for metalation. This metal binding site was metalated with iron (III) and copper (II) by two routes, pre-metalation and post-metalation. Metalation proceeded with complete retention of porosity and crystallinity.

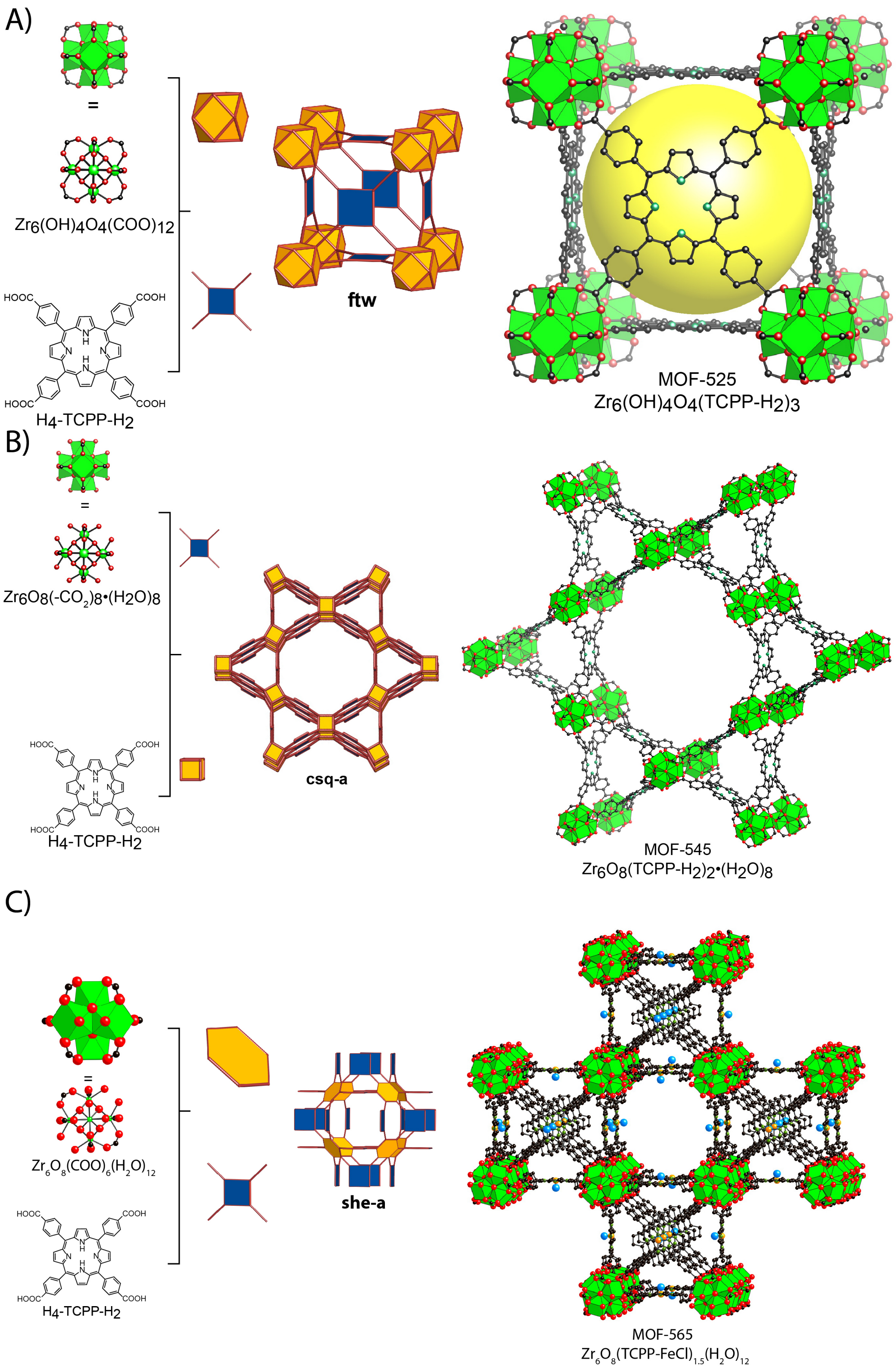

Scheme 4) Structure of MOF-525, MOF-545, and MOF-565

Finally, in chapter 5 gas adsorption applications of ZIFs are discussed, paying special attention to the role of functionality on gas adsorption. It has already been shown that $–NO_2$ functionalities enhanced CO_2 adsorption in **gme** ZIFs.[27] We further investigated the role of functionality on CO_2 and CH_4 adsorption in a series of ZIFs with the **rho** topology, namely ZIF-25 ($Zn(C_5H_7N_2)_2$), ZIF-71 ($Zn(C_3HN_2Cl_2)_2$), ZIF-93 ($Zn(C_5H_5N_2O)_2$), ZIF-96 ($Zn(C_4H_3N_4)_2$), and ZIF-97 ($Zn(C_5H_7N_2O)_2$). In contrast to other studies, the pore sizes and apertures in these **rho** ZIFs are nearly constant across the series. The similarities across the **rho** series allow conclusions to be drawn about a wide series of functionalities. Detailed experimental studies of the activated materials are carried out, including measurement of the surface area, measurement of variable temperature isotherms, and calculations of enthalpy of adsorption. These experimental results were coupled with computational results, which show excellent agreement with the experiment and identify key binding sites of gas molecules within the MOF (**Figure 4**).

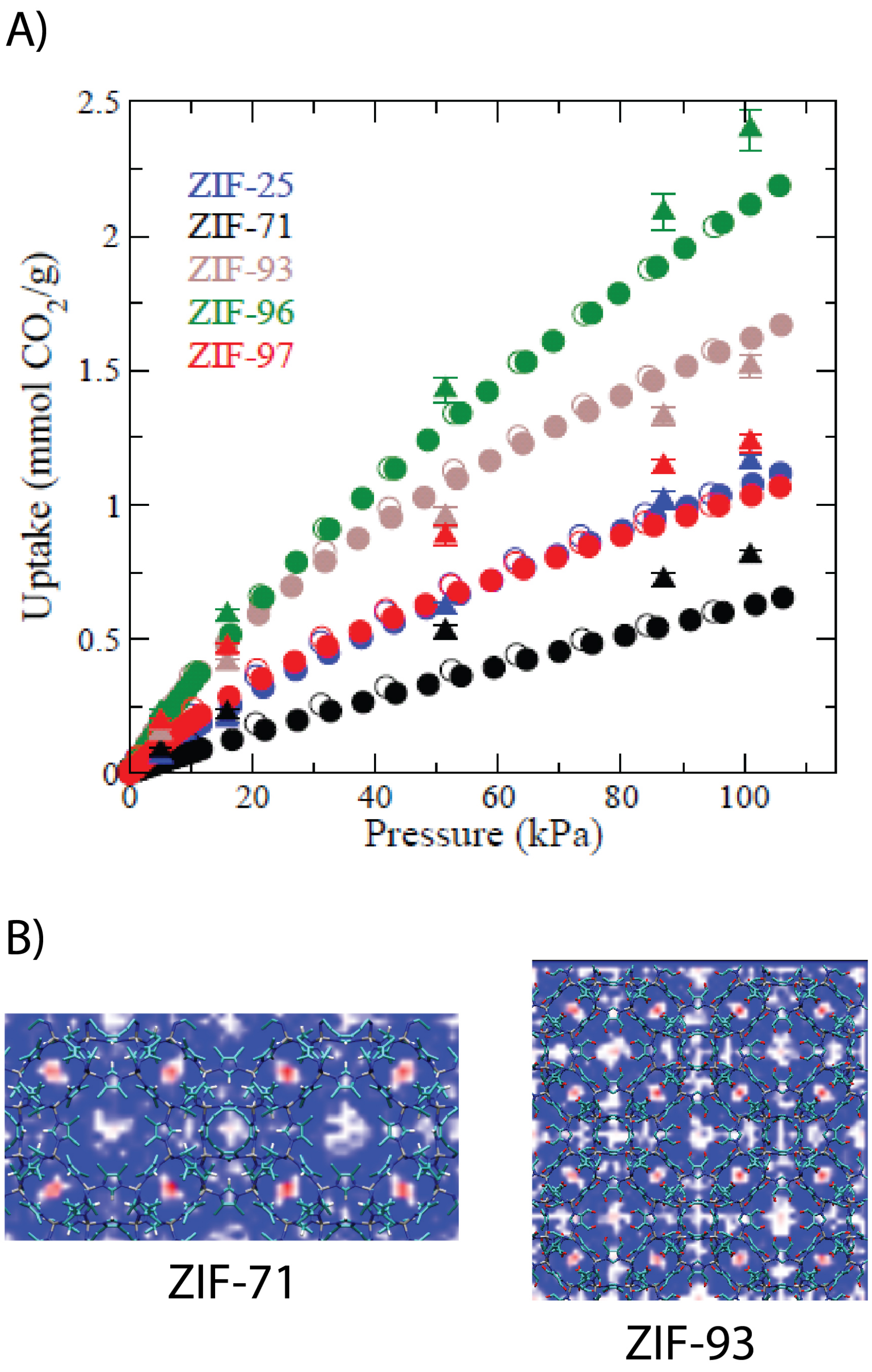

Figure 4) A) CO$_2$ adsorption in series of **rho** ZIFs at 298 K. B) Charge density maps of CO$_2$ adsorption at 1 bar in ZIF-71, and ZIF-93 at 298 K.

References

1) Banerjee, R.; Phan, A.; Wang, B.; Knobler, C.; Furukawa, H.; O'Keeffe, M.; Yaghi, O. M. *Science*. **2008**, *319*, 939-943. b) Rowsell, J. L. C.; Yaghi, O. M. *Microporous Mesoporous Mater.* **2004**, *73*, 3-14 c) Eddaoudi, M.; Moler, D. B.; Li, H.; Chen, B.; Reineke, T. M.; O'Keeffe, M.; Yaghi, O.M. *Accounts of Chemical Research*. **2001**, *34*, 319-330.

2) Furukawa, H.; Ko, N.; Go, Y. B.; Aratani, N.; Choi, S. B.; Choi, E.; Yazaydin, A. O.; Snurr, R. Q.; O'Keeffe, M.; Kim, J.; Yaghi, O. M. *Science*, **2010**, *239,* 424 – 428.

3) Park, K. S.; Ni, Z.; Côté, A. P.; Choi, J. Y.; Huang, R.; Uribe-Romo, F. J.; Chae, H. K.; O'Keeffe, M.; Yaghi, O. M. *Proc. Natl. Acad. Sci. U.S.A.* **2006**, *103*, 10186-10191.

4) Rosi, N. L.; Eckert, J.; Eddaoudi, M.; Vodak, D. T.; Kim, J.; O'Keeffe, M.; Yaghi, O. M. *Science*. **2003**, *300*, 1127-1130.

5) Wu, C.; Hu, A.; Zhang, L.; Lin, W. *J. Am. Chem. Soc.* **2005**, *127*, 8940-8941.

6) Ferey, G.; Mellot-Draznieks, C.; Serre, C.; Millange, F.; Dutour, J.; Surble, S.; Margiolaki, I. *Science*. **2005**, *309*, 2040-2042.

7) White, K. A.; Chengelis, D. A.; Gogick, K. A.; Stehman, J.; Rosi, N. L.; Petoud, S. *J. Am. Chem. Soc.* **2009**, *131*, 18069-18071.

8) Lee, J.; Kim, J.; Hyeon, T. *Advanced Materials*. **2006**, 18, 2073-2094

9) G. T. Kokotailo, S. L. Lawton, D. H. Olson and W. M. Meier, *Nature*. **1978**, *272*, 437-438.

10) Tranchemontagne, D. J.; Mendoza-Cortes, J. L.; O'Keeffe, M. Yaghi, O. M. *Chem. Soc. Rev.* **2009**, *38*, 1257-1283.

11) Chae, H. K.; Siberio-Perez, D. Y.; Kim, J.; Go, Y.-B.; Eddaoudi, M.; Matzger, A. J.; O'Keeffe, M.; Yaghi, O. M. *Nature*. **2004**, *427*, 523-527.

12) Li, H.; Eddaoudi, M.; O'Keeffe, M.; Yaghi, O. M. *Nature*. **1999**, *402*, 276-279

13) Eddaoudi, M.; Kim, J.; Rosi, N. L.; Vodak, D. T.; Wachter, J.; O'Keeffe, M.; Yaghi, O. M. *Science*. **2002**, *295*, 469-472.

14) Morris, W.; Leung, B.; Furukawa, H.; Yaghi, O. K.; He, N.; Hayashi, H.; Houndonougbo, Y.; Asta, M.; Laird, B. B.; Yaghi, O. M. *J. Am. Chem. Soc.* **2010**, *132*, 11006 – 11008.

15) Doonan, C. J.; Morris, W.; Furukawa, H.; Yaghi, O. M. *J. Am. Chem. Soc.* **2009**, *131*, 9492.

16) Tanabe, K. K.; Cohen, S. M. *Chem. Soc. Rev.* **2011**, *40*, 498–519

17) Wang, Z.; Cohen, S. M. *J. Am. Chem. Soc.* **2007**, *129*, 12368.

18) Bloch, E. D.; Britt, D.; Lee, C.; Doonan, C. J.; Uribe-Romo, F. J.; Furukawa, H.; Long, J, R.; Yaghi. O. M. *J. Am. Chem. Soc.* **2010**, *132*, 14382.

19) Abrahams, B. F.; Hoskins, B. F.; Michail, D. M.; Robson, R. *Nature.* **1994**, 369, 727.

20) Choi, E.-Y.; Barron, P. M.; Novotny, R. W.; Son, H.-T.; Hu, C.; Choe, W. *Inorg. Chem.* **2009**, *48*, 426–428.

21) Farha, O. K.; Shultz, A. M.; Sarjeant, A. A.; Nguyen, S. T.; Hupp, J. T. *J. Am. Chem. Soc.* 2011, 133, 5652.

22) Cavka, J. H.; Jakobsen, S.; Olsbye, U.; Guillou, N.; Lamberti, C.; Bordiga, S.; Lillerud, K. P. *J. Am. Chem. Soc.* **2008**, *130*, 13850.

23) Britt, D.; Furukawa, H.; Wang, B.; Glover, T. G.; Yaghi, O. M. *Proc. Natl. Acad. Sci. USA*, **2009**, 106, 20637-20640

24) Koh, K.; Wong-Foy, A.; Matzger, A. J. *Angew. Chem. Int. Ed.* **2008**, *47*, 677.

25) Ingelson, M. J.; Barrio, J. P.; Guilbaud, J.-B.; Khimyak, Y. Z.; Rosseinsky, M. J. *Chem. Commun.* **2008**, 2680.

26) Schaate, A.; Roy, P.; Preube, T.; Lohmeier, S. J.; Godt, A.; Behrens, P. *Chem. Eur. J.* **2011**, *17*, 9320.

27) Banerjee, R.; Furukawa, H.; Britt, D.; Knobler, C.; O’Keeffe, M.; Yaghi, O. M. *J.Am.Chem. Soc*. **2009**, *131*, 3875-3877.

Chapter Two

Crystals as molecules postmodification of ZIF-90.

Introduction

Zeolitic imidazolate frameworks (ZIFs) are porous crystalline materials comprised of tetrahedral metal centers (Zn^{2+}, Cd^{2+}, and Cu^{2+}) bridged by imidazolate units.[1-6] The angles formed in ZIFs are analogous to those of zeolites, often leading to the formation of similar structure topologies.[2] ZIFs are analogous to MOFs in that they are highly porous crystalline extended frameworks. In addition to the properties mentioned above, ZIFs are highly chemically stable.[3] High chemical stability extends the potential applications of these materials in catalysis, gas adsorption, and separation of gas mixtures.

Postmodification of extended crystalline frameworks involves reactions on a MOF framework following its formation.[7-11] Successful postmodification reactions will proceed in high yields with retention of porosity and crystallinity. The first example of postmodification was reported in 2000, and the first example of covalent postmodification being the reaction of acetic anhydride with IRMOF-3 (Scheme 1).[7-8] This reaction proceeded with high yields, bringing to a MOF a new functionality to that could not be incorporated during solvothermal synthesis. A wide range of postmodification reactions have now been carried out on MOFs.[9-11] In this chapter we extend the principals of postmodification to ZIFs. ZIFs have high chemical stability making them ideal candidates for postmodification. High chemical stability will allow for a wider range of organic transformations to be carried out on the framework, under a diverse range of conditions using an extended arsenal of reagents.

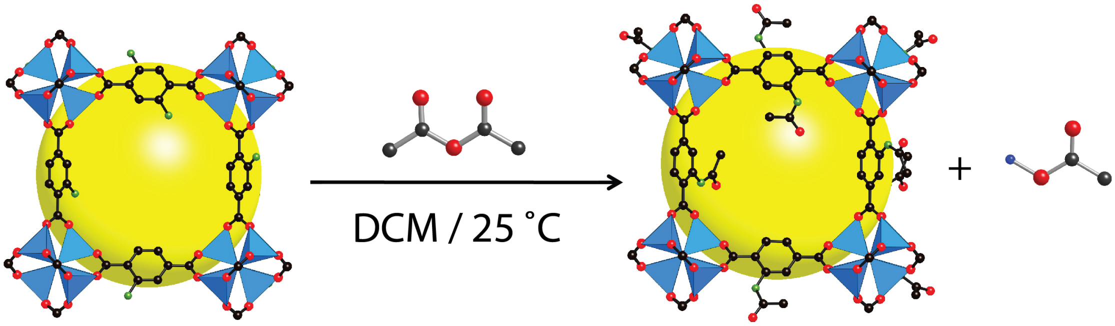

Scheme 1) Postmodification of IRMOF-3.[8]

A large group of ZIF frameworks have been synthesized using high-throughput techniques and conventional solvothermal methods; these materials encompass a diverse range of framework topologies (**Scheme 2**).[4] However, the incorporation of functionalities amenable to postmodification by solvothermal synthesis has not been achieved. Therefore, a new ZIF was synthesized, ZIF-90, which contains an aldehyde functionality suitable for postmodification. Two routes were used to synthesize ZIF-90, traditional solvothermal methods and base diffusion at room temperature. Base diffusion techniques already used in MOFs were extended to ZIFs due to the poor yield of the solvothermal reaction of ZIF-90.[12] Base diffusion produced higher yields than solvothermal methods, and powder X-ray Diffraction confirmed the phase purity of ZIF-90 formed by base diffusion. ZIF-90 was shown to form in the **sod** topology and to have high porosity, analogous to other ZIFs with the same topology. Further characterization of the framework was carried out with ^{13}C CP/MAS solid state NMR, FTIR, and a digestion electrospray mass spectrum.

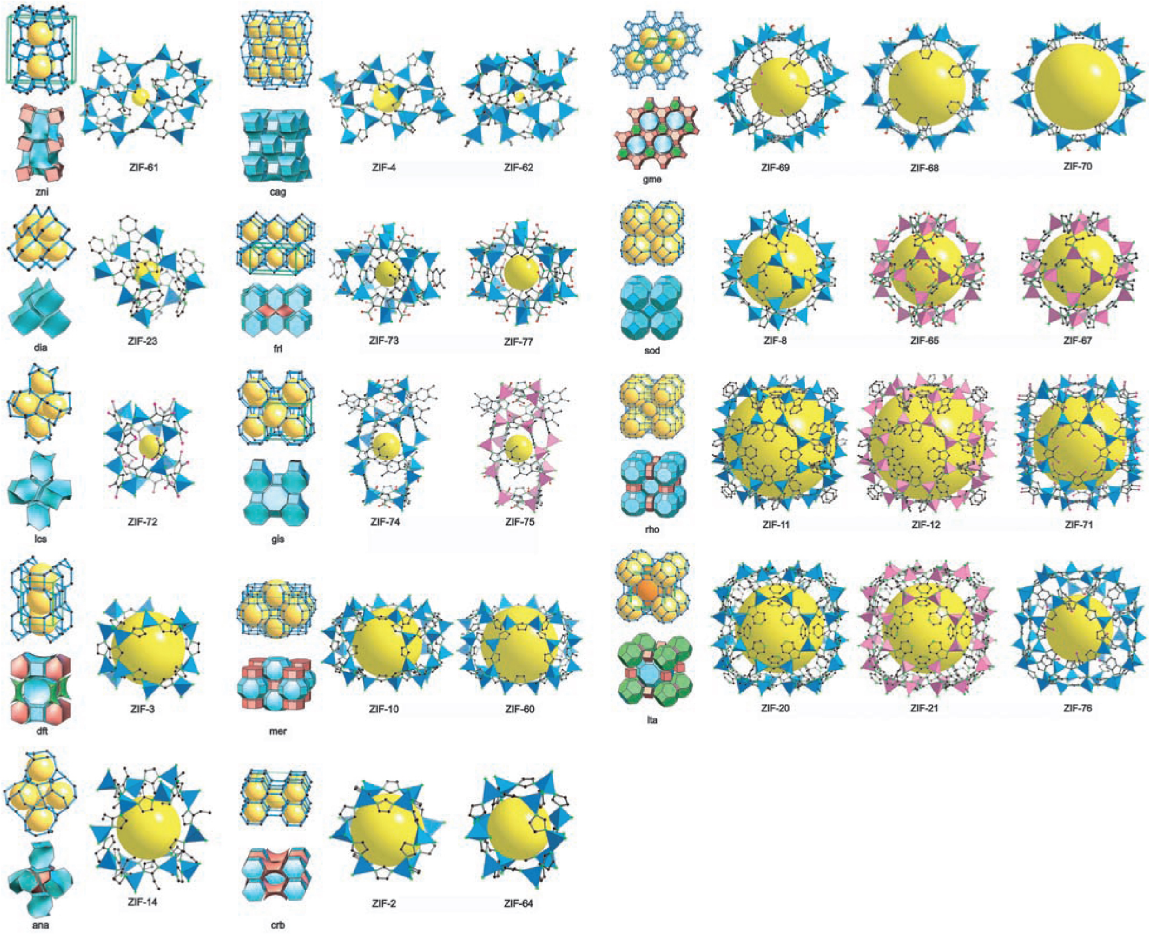

Scheme 2) Structures of ZIFs reported by high-throughput synthesis.[4]

This well characterized ZIF is ideal for testing a range of organic transformations in the solid-state. A range of reactions can be performed on an aldehyde functionality, including reduction to an alcohol, oxidation to a carboxylic acid, and imine formation with amine. The high chemical stability of the ZIF allowed a harsher range of reagents and reaction conditions to be used for these transformations. Successful reduction and imine formation were observed in high yields with retention of structure to form ZIF-91 and ZIF-92, respectively (**Scheme 2**). Organic transformations on the ZIF were characterized by PXRD, gas adsorption, ^{13}C CP/MAS solid state NMR, FTIR, digestion electrospray mass spectra, and digestion ^{1}H NMR spectroscopy (**Scheme 3**).

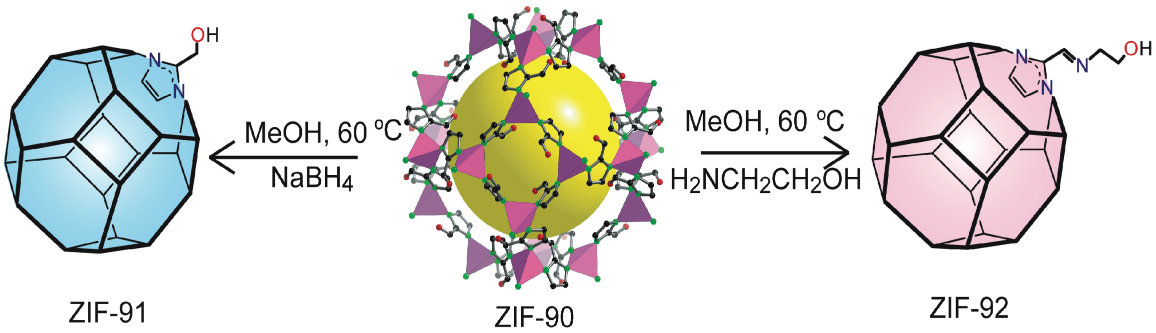

Scheme 3) Postmodification of ZIF-90 to form ZIF-91 and ZIF-92.

Experimental

Materials and general procedures. All reagents were obtained from commercial sources (Alfa Aesar, Cambridge isotope laboratories, Sigma Aldrich) and no further purification was carried out. Yields reported are unoptimized. Elemental microanalyses were performed at University of California Los Angeles.

Synthetic procedure for ZIF-90.

Solvothermal procedure. Single crystals of ZIF-90 were obtained by heating a solution of zinc nitrate tetrahydrate ($Zn(NO_3)_2 \cdot 4H_2O$) (0.054 g, 0.21 mmol) and imidazole-2-carboxyaldehyde (0.029 g, 0.30 mmol) in N,N-dimethylformamide (DMF, 3 mL) for 18 h at 100 ºC.

Vapor diffusion. A solution of Zinc nitrate tetrahydrate ($Zn(NO_3)_2 \cdot 4H_2O$) (0.13 g, 0.50 mmol) and imidazole-2-carboxyaldehyde (0.07 g, 0.75 mmol) in DMF (10 mL) was placed in a desiccator under an atmosphere of triethylamine (5 mL) in hexane (200 mL). The reaction was allowed to remain at room temperature for 24 h. The crystalline powder obtained was filtered and washed with methanol (3 × 5 mL). The product was activated with methanol (3 × 10 mL) over a three-day period before being dried under vacuum (10^{-}

^{2} Torr) for 24 h at room temperature. Yield (0.08 g, 61.5%) CHN calculated for $C_8H_6N_4O_2Zn$: C, 37.60; H, 2.37; N, 21.92% Found: C, 37.63; H, 2.76; N, 20.48%.

Procedure for covalent post synthetic modification of ZIF-91 and ZIF-92.

ZIF-91 $Zn(C_4H_3N_2O)_{0.4}(C_4H_5N_2O)_{1.6}$ Dried ZIF-90 crystals (0.10 g, 0.39 mmol) were suspended in methanol (10 mL) and $NaBH_4$ (0.06 g, 1.56 mmol), and refluxed for 24 h. The reaction mixture was filtered and the solid was washed 2-3 times with fresh methanol (20 mL). The microcrystalline solid was further exchanged with fresh methanol (20 mL) for 24 h. The solid was dried under vacuum (10^{-2} Torr) for 24 h at room temperature. Yield (0.09 g, 89%), conversion 77 %. It should be noted that higher conversion of ZIF-90 to ZIF-91 may be achieved with reaction times exceeding 24 h; however, a reduction in crystallinity is observed.

ZIF-92 $Zn(C_6H_8N_3O)_2$ Dried ZIF-90 crystals (0.15 g, 0.59 mmol) was suspended in methanol (10 mL) and ethanolamine (0.11 mL, 1.76 mmol), and refluxed for 24 hours. The reaction mixture was filtered and the solid was washed 2-3 times with fresh methanol (20 mL). The solid was further exchanged with fresh methanol (20 mL) for 24 h. The solid was dried under vacuum (10^{-2} Torr) for 24 h at room temperature. Yield (0.16 g, 80%), conversion 100%.

Powder X-ray diffraction.

Powder X-ray data were collected using a Bruker D8-Discover θ-2θ diffractometer in reflectance Bragg-Brentano geometry employing Ni filtered Cu Kα line focused radiation at 1600 W (40 kV, 40 mA) power and equipped with a Vantec Line detector. Radiation was focused using parallel focusing Gobel mirrors. The system was also outfitted with an anti-scattering shield that prevents incident diffuse radiation from hitting the detector, preventing the normally large background at 2θ < 3. Samples were mounted on zero background sample holders by dropping powders from a wide-blade spatula and then leveling the sample with a razor blade.

^{13}C CP/MAS solid state NMR

High-resolution solid-state nuclear magnetic resonance (NMR) spectra were recorded at ambient pressure on a Bruker DSX-300 spectrometer using a standard Bruker magic angle-spinning (MAS) probe with 4 mm (outside diameter) zirconia rotors. The magic angle was adjusted by maximizing the number and amplitudes of the signals of the rotational echoes observed in the ^{79}Br MAS FID signal from KBr. Cross-polarization with MAS (CP/MAS) was used to acquire ^{13}C data at 75.47 MHz. The ^{1}H and ^{13}C ninety-degree pulse widths were both 4 ms. The CP contact time varied from 1.5 to 5 ms. High power two-pulse phase modulation (TPPM) ^{1}H decoupling was applied during data acquisition. The decoupling frequency corresponded to 72 kHz. The MAS sample-spinning rate was 10 kHz. Recycle delays between scans varied between 3 and 10 s, depending upon the compound as determined by observing no apparent loss in the ^{13}C signal from one scan to the next. The ^{13}C chemical shifts are given relative to tetramethylsilane as zero ppm, calibrated using the methylene carbon signal of adamantane assigned to 37.77 ppm as the secondary reference.

Digestion ^{1}H solution NMR.

Solution NMR ^{1}H nuclear magnetic resonance spectroscopy. Solution nuclear magnetic resonance (NMR) spectra were obtained at ambient temperature using a Bruker 400 MHz instrument. The signals are presented relative to TMS as 0 ppm using the water peak as a secondary reference at 4.79 ppm.

Gas adsorption measurements.

Low-pressure gas adsorption isotherms were measured volumetrically on an Autosorb-1 analyzer (Quantachrome Instruments). A liquid nitrogen sample bath (77 K) was used for N_2, Ar, and H_2 isotherm measurements. The N_2, Ar, H_2 and He gases used were UHP grade. For measurement of the apparent surface areas (S_{Lang}), the Langmuir or BET method was applied using the adsorption branches of the N_2 isotherms assuming a N_2 cross-sectional area of 16.2 $Å^2$/molecule. The total pore volumes (V_p) were determined using the Dubinin-Raduskavich (DR) method.

ESI mass spectrometry.

Single crystal X-ray diffraction data collection, structure solution and refinement procedures.

General Data Collection and Refinement Procedures: Data were collected on a Bruker SMART APEXII three circle diffractometer equipped with a CCD area detector and operated at 1200 W power (40 kV, 30 mA) to generate Cu Kα radiation (λ = 1.5418 Å). The incident X-ray beam was focused and monochromated using Bruker Excalibur Gobel mirror optics. A crystal of ZIF-90 was mounted on a nylon CryoLoops (Hampton Research) with Paraton-N (Hampton Research).

Initial scans of each specimen were performed to obtain preliminary unit cell parameters and to assess the mosaicity (i.e. breadth of spots between frames) of the crystal to select the required frame width for data collection. In every case frame widths of 0.5° were judged to be appropriate and full hemispheres of data were collected using the Bruker APEX21 software suite to carry out overlapping φ and ω scans at three different detector (2θ) settings (2θ = 28, 60, 100º). Following data collection, reflections were sampled from all regions of the Ewald sphere to redetermine unit cell parameters for data integration and to check for rotational twinning using CELL_NOW2. In no data collection was evidence for crystal decay encountered. Following exhaustive review of collected frames the resolution of the dataset was judged. Data were integrated using Bruker APEX2 V 2.13 software with a narrow frame algorithm and a 0.400 fractional lower limit of average intensity. Data were subsequently corrected for absorption by the program SADABS4. The absorption coefficient (μ) is 1.94 cm-1 for the ZIF reported in this paper. However it is noteworthy that the calculation of μ is based on the atomic contents and this is uncertain for most ZIF structures. The precise solvent molecule content is not known due to the diffuse electron density. The space group determination and tests for merohedral twinning were carried out using XPREP3. In all cases, the highest possible space group was chosen.

All structures were solved by direct methods and refined using the SHELXTL 975 software suite. Atoms were located from iterative examination of difference F-maps following least squares refinements of the earlier models. Final models were refined anisotropically (if the number of data permitted) until full convergence was achieved. Hydrogen atoms were placed in calculated positions (C—H = 0.93 Å) and included as riding atoms with isotropic displacement parameters 1.2–1.5 times Ueq of the attached C atoms. Modeling of electron density within the voids of the frameworks did not lead to identification of guest entities in this structure due to the disordered contents of the large pores in the frameworks. The problem, which is typical for highly porous crystals that contain solvent filled pores, lies in the raw data where observed strong (high intensity) scattering becomes limited to ~1.0 Å at best, with higher resolution data sometimes present but weak (low intensity). A common strategy for improving X-ray data, increasing the exposure time of the crystal to X-rays did not improve the quality of the high angle data in this case, as the intensity from the low angle data saturated the detector and minimal improvement in the high angle data was achieved. Additionally, diffuse scattering from the highly disordered solvent in the void spaces within the crystal and from the loop used to mount the crystal contributes to the background noise and the 'washing out' of high angle data. The only optimal crystals suitable for analysis were generally small and weakly diffracting, and unfortunately, larger crystals, which would usually improve the quality of the data, presented a lowered degree of crystallinity and attempts to optimize the crystal growing conditions for large high-quality specimens has not yet been fruitful. For ZIF-90, it was found that data collection at -173 ºC was optimal for obtaining the best data. In such cases the modeling of the disordered guest entities becomes intractable because at the lower temperature they become frozen into highly disordered arrays. Thus, electron density within void spaces, which could not be assigned to any definite guest entity, was modeled as isolated oxygen and/or carbon atoms, and the foremost errors in all the models lies with assignment of guest electron density. To prove the correctness of the atomic positions in the framework the application of the SQUEEZE routine of A. Spek has been performed. The assignment and refinement of the metal-organic ZIF framework atoms was unambiguous, as judged by the resulting bond and angle metrics which are chemically accurate and precise values. All structures were examined using the Adsym subroutine of PLATON7 to assure that no additional symmetry could be applied to the models. All ellipsoids in ORTEP diagrams are displayed at the 30 % probability level unless noted otherwise. For all structures we note that the elevated R-values are commonly encountered in MOF crystallography, for the reasons expressed above, by us and other research groups.

Results and Discussion

Synthesis and characterization of ZIF-90. ZIF-90 was synthesized by two-routes, solvothermally and by base diffusion at room temperature. Solvothermal reactions between zinc nitrate and imidazole-2-carboxaldehyde at 100 ˚C yielded single crystals of ZIF-90 in low yields. The structure of ZIF-90 was resolved from single crystal diffraction and shown to belong to the **sod** topology with tetrahedral zinc units bridged by imidazolate units (**Figure 1**). The **sod** cages of ZIF-90 are decorated with aldehyde functionalities, with a diameter of 11.2 Å and pore windows 3.5 Å in diameter. Solvothermal synthesis resulted in low yields unsuitable for scale-up; to perform postmodification larger quantities of ZIF-90 are required. Therefore, new techniques for ZIF synthesis were developed; namely, base diffusion at room temperature was the method of choice. This procedure relied on diffusion of a base at room temperature, in this case triethylamine diffusing into a solution of zinc nitrate and imidazole-2-carboxaldehyde, resulting in high yields of microcrystalline powder, which were shown to be analogous to ZIF-90 formed from solvothermal synthesis by PXRD (**Figure 2**).

To access the porosity and characterize ZIF-90 further, the solvents must first be removed from the pores. Solvent removal was achieved by washing with methanol and then applying a vacuum for 24 hrs. The N_2 isotherm was Type one in shape indicative of a microporous material with permanent porosity (**Figure 3**). The hysteresis loop observed in ZIF-90 was due to the small pore aperture hindering N_2 access to the pore (**Figure 3**). This hysteresis loop was not observed on adsorption of argon, which has a smaller kinetic diameter than N_2. (**Figure 4**). Although a hysteresis was observed, it was possible to calculate Langmuir and BET surface areas from the N_2 isotherm data; for ZIF-90 these were 1320 and 1270 m^2 g^{-1}, respectively. ZIF-90 was shown to be stable to 500 ˚C by thermogravimetric analysis and high chemical stability is maintained, after exposure to a range of aqueous and organic conditions ZIF-90 maintained crystallinity. The high surface area and chemical stability of ZIF-90 make it ideal for studies of postmodification.

To further characterize the phase purity of ZIF-90 in the solid-state, ^{13}C cross polarization magic angle spinning (CP/MAS) NMR and FTIR spectra were carried out. The ^{13}C CP/MAS NMR spectrum displayed the correct resonances including the aldehyde functionality at 178 ppm (**Figure 5**). In addition, FTIR contained a strong band at 1678 cm^{-1} indicative of the aldehyde functionality. FTIR and solid state NMR provide valuable characterization techniques for monitoring the postmodification of ZIF-90.

Postmodification of ZIF-90 to form ZIF-91. The first reaction to be attempted on ZIF-90 was the reduction of the aldehyde to the alcohol (**Scheme 2**). A fully activated sample of ZIF-90 was placed in MeOH and a large excess of $NaBH_4$ was added to the reaction. After the reaction was allowed to proceed for 12 hrs the ZIF was washed with MeOH to remove unwanted reactants to yield ZIF-91. To access the properties of ZIF-91 it was first activated under analogous conditions to that of ZIF-90. An analogous PXRD to that of ZIF-90 confirmed the **sod** structure had been maintained (**Figure 6**). The Langmuir and BET surface area of ZIF-91 were accessed from the N_2 isotherm and found to be 1070 and 1010 m^2 g^{-1}, respectively. The small decrease in surface area that is observed from ZIF-90 to ZIF-91 is attributed to the smaller pore aperture of ZIF-91 (**Figure 6**) and not to damage caused by the reaction.

To confirm that reduction of the aldehyde had proceeded, ^{13}C CP/MAS NMR was measured (**Figure 7**). The ^{13}C NMR spectrum showed resonances attributed to both the aldehyde and the alcohol functionality, showing the reaction had not proceeded to completion. Four resonances from imidazolate, were observed confirming the presence of two imidazolate species in ZIF-91. To obtain a yield for the reaction the ZIF-91 was digested in 20 % DCl/D_2O and the ^1H NMR spectrum was measured; the integrals showed the reaction had proceeded with approximately 80 % completion (**Figure 7**). In addition, the electrospray ionization mass spectrum of the digested aliquot showed the negative parent ions of the aldehyde and alcohol imidazolate links at 95.2 and 97.3 m/z, respectively. Attempts to increase the reaction yield by increasing the concentration of $NaBH_4$ and the reaction time proved to reduce the framework crystallinity. In addition, replacement of $NaBH_4$ with $LiAlH_4$ a stronger reductant, resulted in reduction of Zn^{2+} and destruction of the framework.

Postmodification of ZIF-90 to form ZIF-92. The second transformation to be accessed on ZIF-90 was imine formation. ZIF-90 was reacted with ethanolamine in MeOH at 60 ˚C to form ZIF-92 (**Scheme 2**). The reaction proceeded to completion in three hours. The reaction was again characterized by ^{13}C CP/MAS NMR, which showed no evidence of the aldehyde functionality, showing the reaction had proceeded with 100 % yield (**Figure 5**). In addition, the NMR spectrum showed an imine resonance at 154 ppm and one set of imidazolate carbons at 149 ppm and 128 ppm. Further confirming that the reaction proceeded to completion, FTIR displayed a characteristic imine stretch at 1637 cm^{-1} and no aldehyde stretch at 1678 cm^{-1}. As in the case of ZIF-91, PXRD of ZIF-92 confirmed that the structure of ZIF-92 was analogous to the parent ZIF-90 (**Figure 6**). Most interestingly ZIF-92 was found to be non-porous (**Figure 3**). This reduction in porosity with maintenance of crystallinity was attributed to blocking of the pores of ZIF-92 by the imine functionality (**Figure 3**). The high yields of imine formation show that diffusion into the MOF proceeded more quickly than imine formation.

Conclusions

A new ZIF, ZIF-90, suitable for postmodification was synthesized. Two routes to synthesis of ZIF-90 were developed, including the first example of base diffusion to form a ZIF framework. The ZIF incorporated aldehyde functionalities on the imidazolate, which decorated the **sod** cage. This ZIF was porous and crystalline making it suitable for postmodification. Two reactions proceeded in high yields with retention of structure, reduction and imine formation to form ZIF-91 and -92, respectively. These reactions were characterized by techniques including ^{13}C solid state NMR, FTIR, and digestion ^{1}H NMR. These first examples show that postmodification can be extended to ZIFs.

Surface area measurements highlighted one factor, pore size, that must be considered for future postmodifications of porous materials. ZIF-92 showed a complete reduction in surface area upon postmodification, highlighting the need for large pores in future postmodification studies if porosity must be maintained upon postmodification. However, this reduction in porosity could also be used to encapsulate molecules in the pores of ZIF-90. The need for highly chemical stable frameworks remains crucial; considerations still have to be made about framework stability in these stable ZIFs when considering organic reactants. For example, complete loss of crystallinity was observed when ZIF-90 was exposed to a stronger reductant, $LiAlH_4$. Therefore, frameworks with higher chemical stability than ZIFs and larger pores are required if we want to release the potential of covalent organic transformations in extended porous frameworks.

Figures

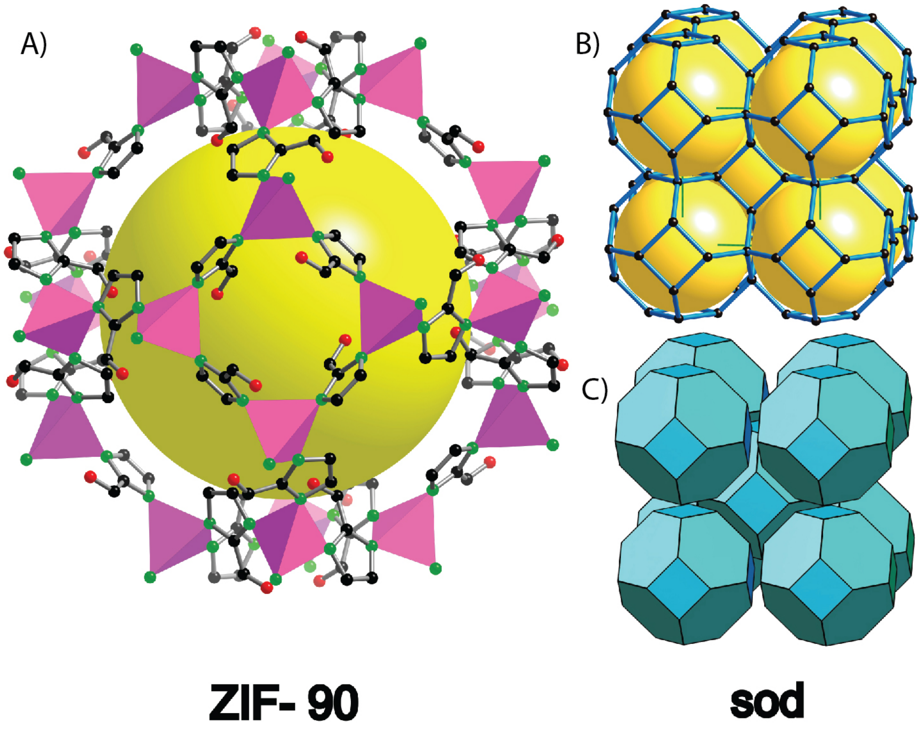

Figure 1) Structure of ZIF-90. A) Cut away view of one of the sod cages. B) Net representation of the structure C) Tiling to show the subdivision of space.

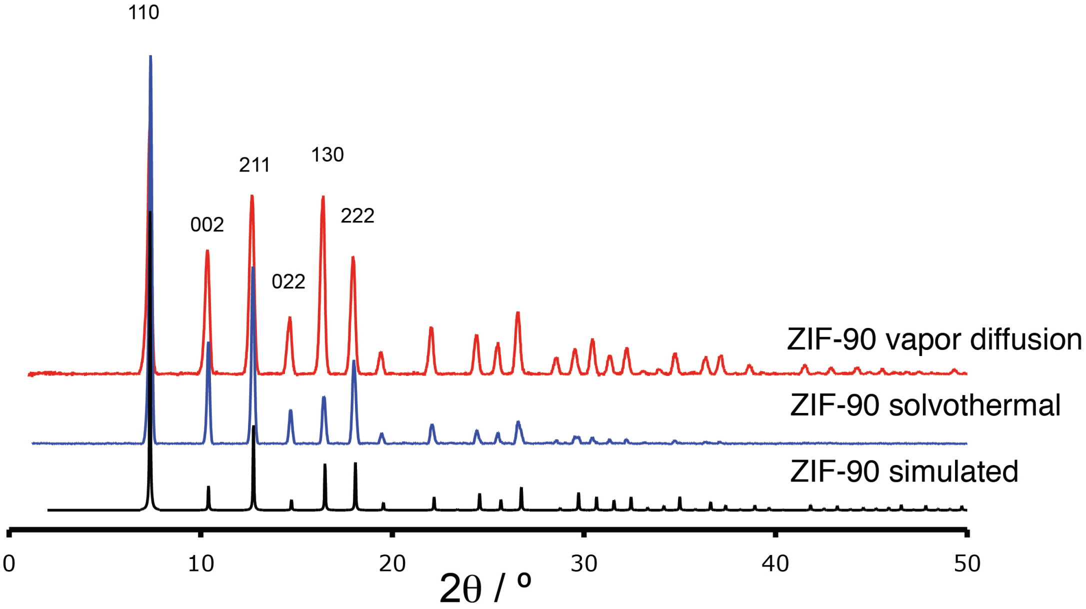

Figure 2) Powder X-ray diffraction of products formed by different techniques. ZIF-90 simulated (black), ZIF-90 solvothermal (blue), and ZIF-90 vapor diffusion (red).

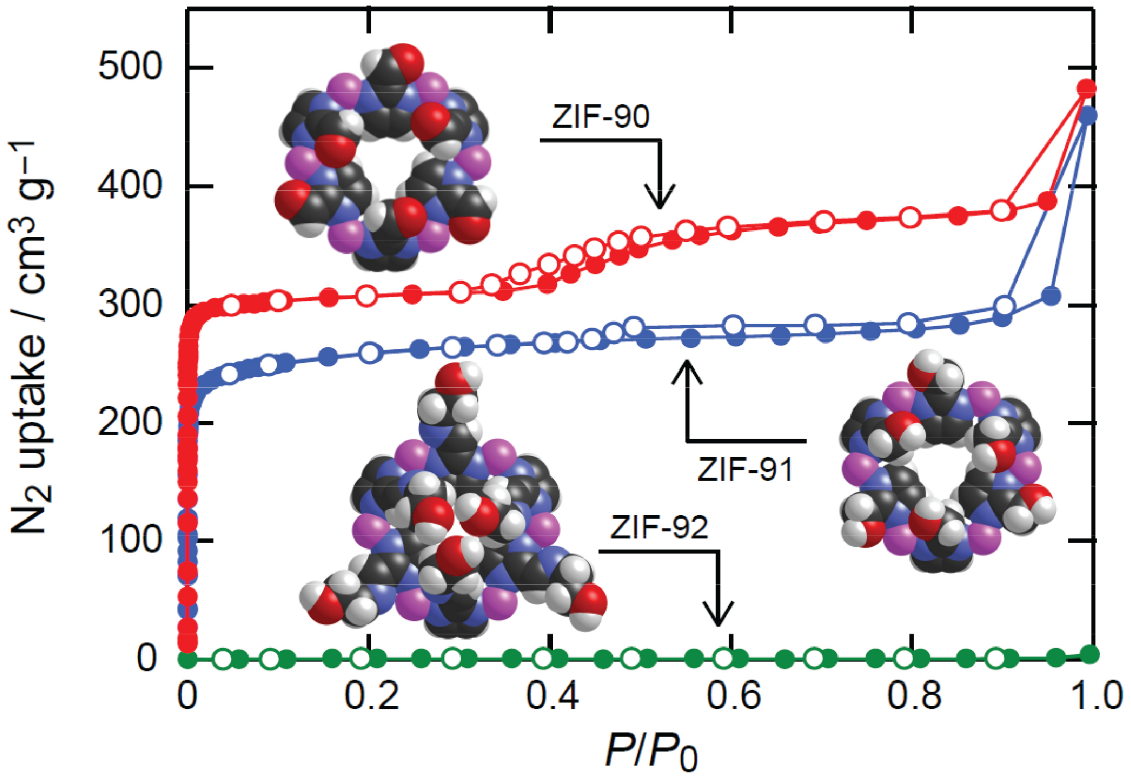

Figure 3) N$_2$ isotherms at 77 K and space filling representations of the pores of ZIF-90 (red), -91 (blue), and -92 (red).

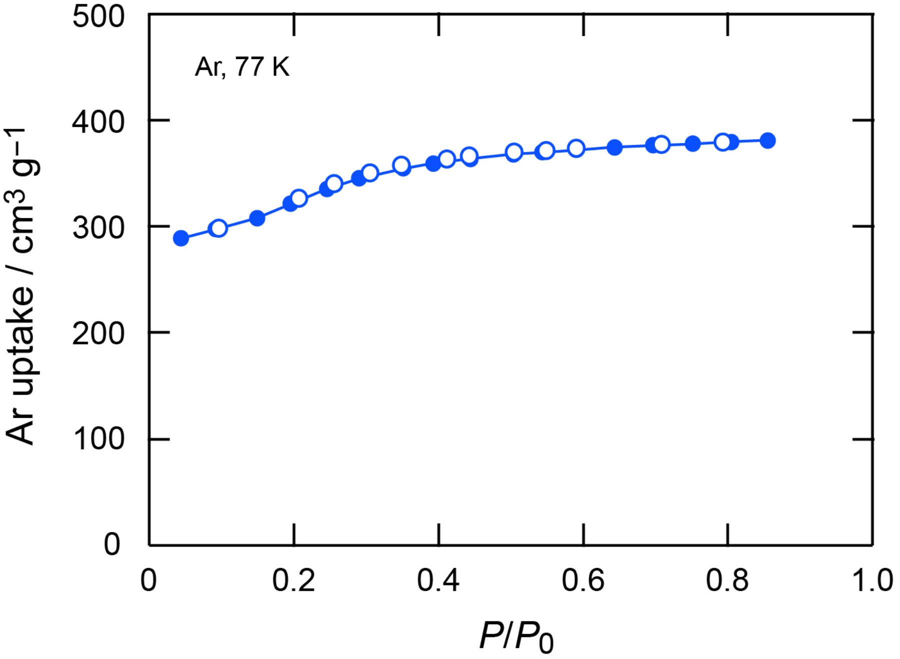

Figure 4) Ar isotherm at 77 K of ZIF-90

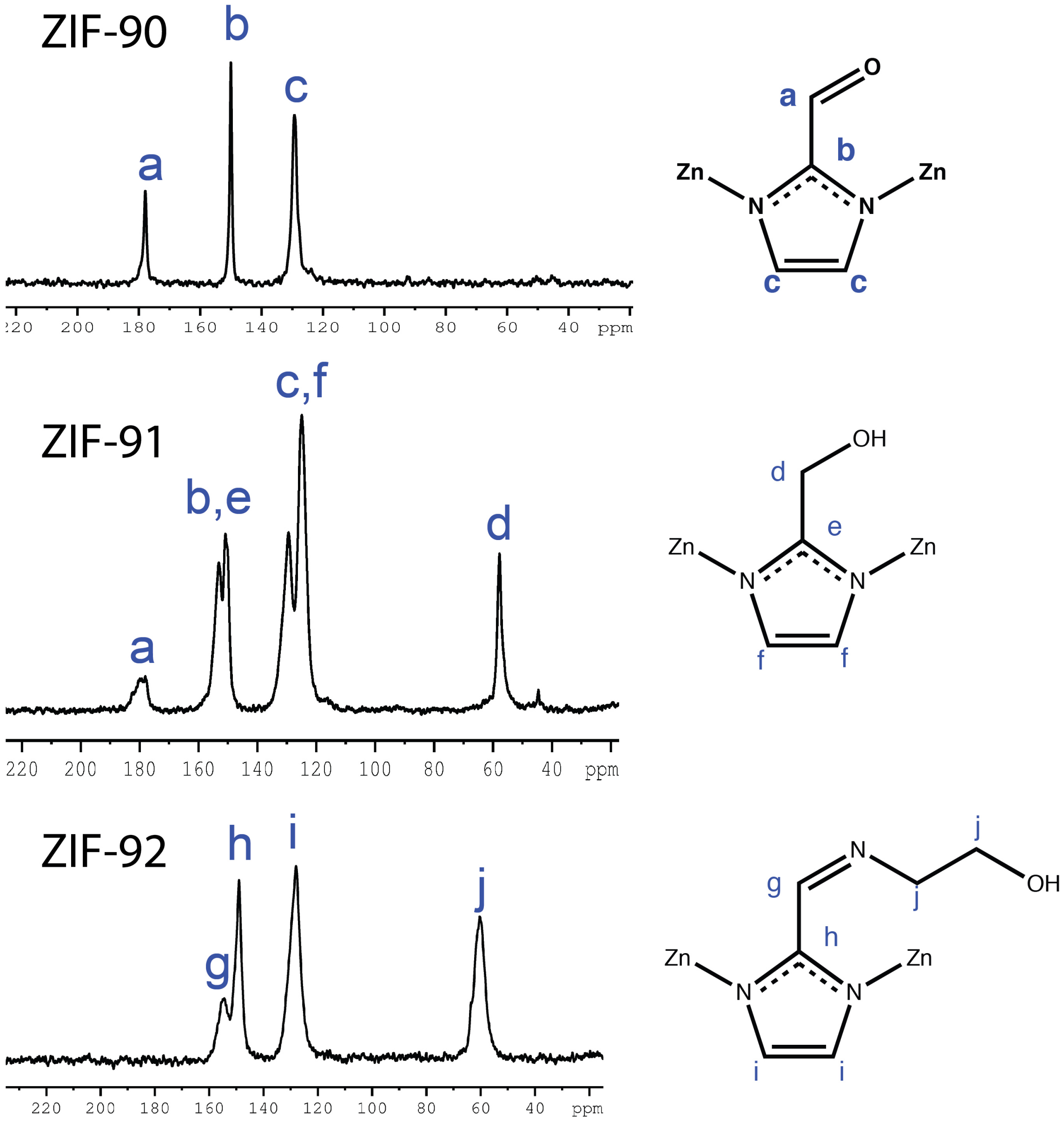

Figure 5) ^{13}C CP/MAS solid state NMR spectrum of ZIF-90, -91, and -92

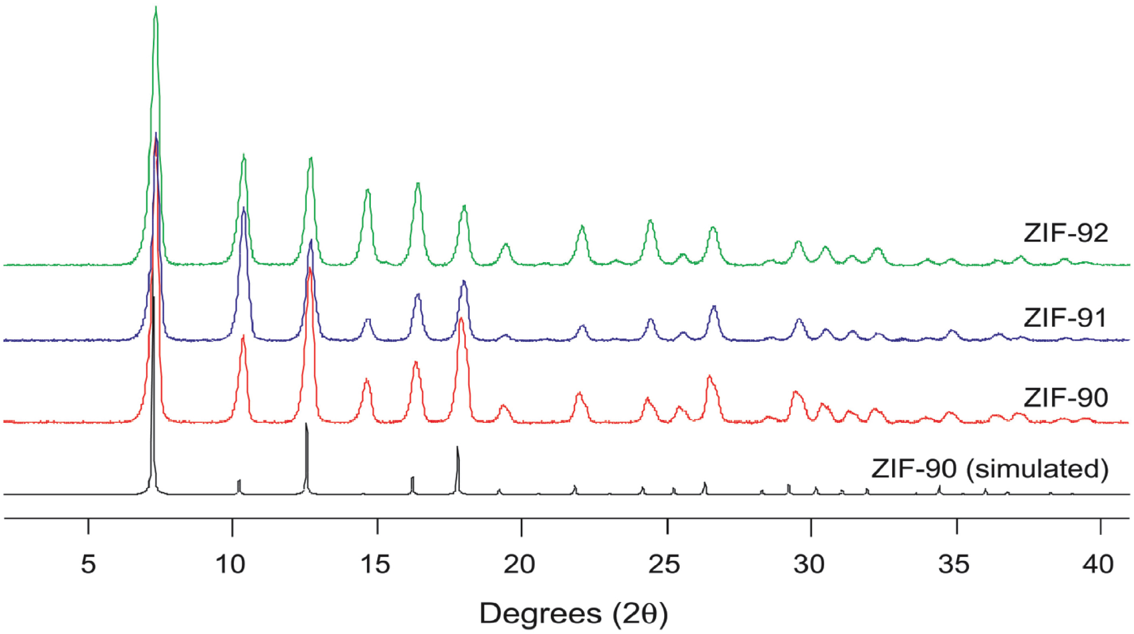

Figure 6) Powder X-ray Diffraction data of simulated ZIF-90 (black) ZIF-90 (red), -91 (blue), and -92 (red).

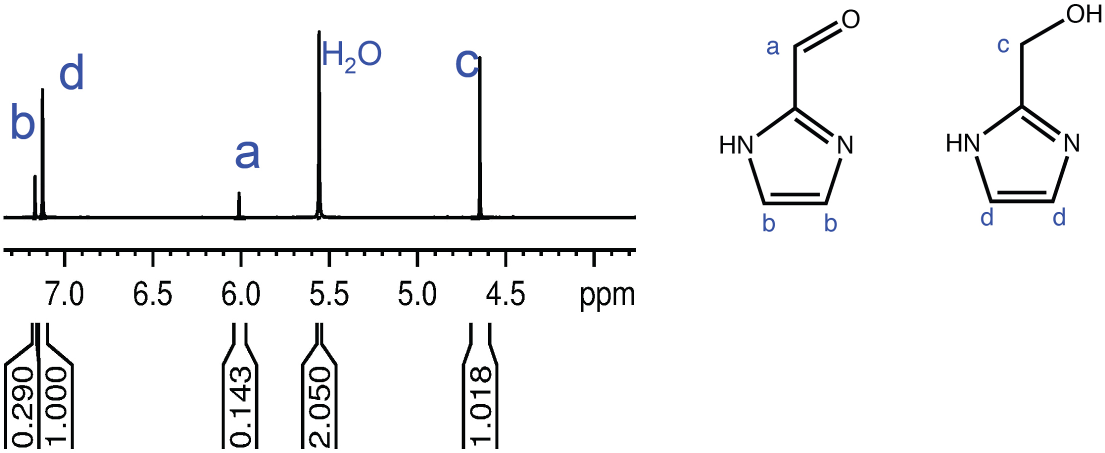

Figure 7) ^{1}H NMR of digested ZIF-91

References

1) Phan, A.; Doonan, C.; J. Uribe-Romo, F.; Knobler, C. B.; O'Keeffe, M.; Yaghi, O. M. *Acc. Chem. Res*. **2009**, 43, 58-67

2) Banerjee, R.; Phan, A.; Wang, B.; Knobler, C.; Furukawa, H.; O'Keeffe, M.; Yaghi, O. M. *Science.* **2008**, *319*, 939.

3) Park, K. S.; Ni, Z.; Cote, A. P.; Choi, J. Y.; Huang, R. D.; Uribe-Romo, F. J.; Chae, H. K.; O'Keeffe, M.; Yaghi, O. M. *Proc. Natl. Acad. Sci. U.S.A.* **2006**, *103*, 10186.

4) Banerjee, R.; Furukawa, H.; Britt, D.; Knobler, C.; O'Keeffe, M.; Yaghi, O. M. *J. Am. Chem. Soc*. **2009**, *131*, 3875-3877

5) Huang, X. -C.; Lin, Y. Y.; Zhang, J. P.; Chen, X. M. *Angew. Chem., Int. Ed*. **2006**, 45, 1557–1559.

6) Hayashi, H.; Cote, A. P.; Furukawa, H.; O'Keeffe, M.; Yaghi, O. M. *Nat. Mater*. **2007**, 6, 501–506

7) Seo, J. S.; Whang, D.; Lee, H.; Jun, S. I.; Oh, J.; Jeon, Y. J.; Kim, K. *Nature* **2000**, *404*, 982.

8) Wang, Z.; Cohen, S. M. *J. Am. Chem. Soc.* **2007**,*129*, 12368.

9) Tanabe, K. K.; Wang, Z.; Cohen, S. M. *J. Am. Chem. Soc.***2008**, *130*, 8508.

10) Costa, J. S.; Gamez, P.; Black, C. A.; Roubeau, O.; Teat, S. J.; Reedijk, J. *Eur. J. Inorg. Chem.* **2008**, 1551.

11) Wang, Z.; Cohen, S. M. *Angew. Chem., Int. Ed.* **2008**, *47*, 4699. b) Ingelson, M. J.; Barrio, J. P.; Guilbaud, J.-B.; Khimyak, Y. Z.; Rosseinsky, M. J. *Chem. Commun.*

2008, *23*, 2680.

12) Tranchemontagne, D. J.; Hunt, J. R.; Yaghi, O. M. *Tetrahedron*, **2008**, *64*, 8553-8557.

Chapter 3

Metalation of a zinc based MOF with large pores.

Introduction

Formation of small molecule coordination complexes between metal centers and ligands has been well researched, including many well known examples (**Scheme 1**).[1-3] Small molecule coordination complexes have been used for many applications including homogenous catalysis,[1] drug therapies,[2] and as contrast agents.[3] Incorporation into solid state materials may lead to enhancements in catalysis, gas adsorption, and drug synthesis; however, production of these solid state materials remains challenging. Efforts by others have seen the incorporation of coordination complexes into mesoporous silica[4] and activated carbon[5] among others. However, these complexes are often hard to coordinate to the surfaces of solid-state materials, and as a result low yields are usuallly obtained. MOFs offer an ideal alternative to activated carbons and mesoporous silica, a highly ordered porous reaction space, which is decorated with organic moieties ideal for carrying out coordination chemistry in the solid-state.[6]

Scheme 1) Metal complexes. A) Grubbs Catalyst B) Cisplatin C) Antrirum

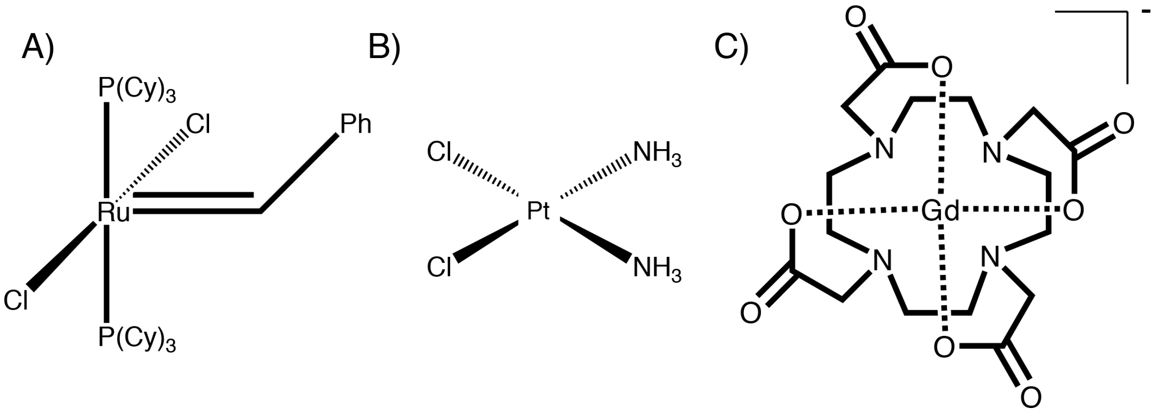

Solvothermal synthesis of MOFs have often limited the incorporation of coordination complexes into MOF frameworks; only a few examples have been reported.[7] To overcome the limitations of the solvothermal synthesis, we sought to incorporate coordination complexes by postmodification. Postmodification of organic functionalities incorporated during solvothermal synthesis offers a more general route to the incorporation of coordination complexes into MOF materials.[8] Attempts to metalate IRMOF-3 resulted in low yields and pore blocking; therefore, we selected a MOF with large pores (23.2 Å and 30.2 Å) and amine functionalities, UMCM-1-NH_2.[9,10]

A two-step postmodification reaction was used to incorporate a coordination complex within the MOF (**Scheme 2**). First, we chose to select a well-known small molecule ligand, the iminopyridine pyridine moiety, to incorporate into the MOF. Iminopyridine units are synthesized through an imine condensation reaction between an aldehyde and an amine functionality, which has already been shown to be compatible with MOF synthesis.[11] Unlike other solid-state materials, the MOF offered an ideal platform for this reaction as amine units are incorporated into the MOF structure. The synthesis of the iminopyridine moiety proceeded to completion without pore blocking because of the large pore size. The formation of the iminopyridine unit by postmodification was characterized by elemental analysis, color change, and mass spectrometry. The structural integrity following postmodification was confirmed by analysis of the Powder X-ray diffraction pattern and gas adsorption measurements of the surface area, which showed that porosity and crystallinity were maintained.

Scheme 2) Metalation of UMCM-1-NH_2. A) UMCM-1-NH_2, UMCM-1-Imine, and UMCM-1-Pd

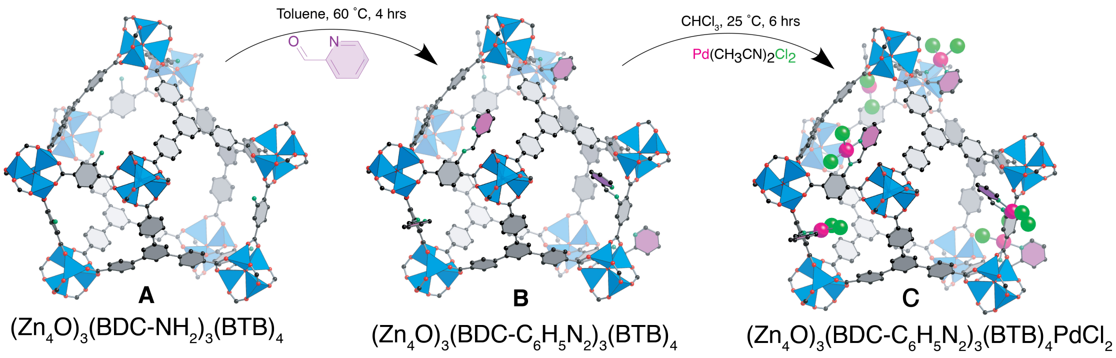

The iminopyridine moiety is attached to the MOF surface in a quantitative manner; these the postmodified MOF is ideal for the incorporation of a coordination complex. A palladium center was selected for the postmodification, as a large number of square planar palladium iminopyridine complexes have been reported as small molecules. $PdCl_2(CH_3CN)_2$ was added to the iminopyridine-appended MOF and was allowed to react for 48 hrs to yield a quantitatively metalated framework. Retention of crystallinity and porosity was observed, consistent with the maintenance of the underlying structure of the framework. Elemental microanalysis confirmed the expected Pd:Zn ratio; each iminopyridine complex is metalated with palladium. To confirm that the palladium was bound to the iminopyridine moiety and was not free in the MOF, the extended X-ray absorption fine structure (EXAFs) and X-ray absorption near edge structure (XANES) were measured, and these measurements confirmed binding within the iminopyridine moiety

Experimental

Materials and general procedures. All reagents unless otherwise stated were obtained from commercial sources (Alfa Aesar, Cambridge isotope laboratories, Sigma Aldrich) and were used without further purification and all manipulations were carried out in an Ar atmosphere. Yields reported were unoptimized. Elemental microanalyses were performed at the University of California, Los Angeles, Department of Chemistry and Biochemistry.

Synthesis and metalation of UMCM-1-NH_2

Synthetic procedure for $(Zn_4O)_3(BDC\text{-}C_6H_5N_2)_3(BTB)_4$. 200 mg $(Zn_4O)_3(BDC\text{-}NH_2)_3(BTB)_4$ was placed in a 20 ml glass vial and immersed in 10 ml of anhydrous toluene. 0.3 ml of 2-pyridinecarboxaldehyde was added to the vial and the mixture was allowed to stand unperturbed for 5 days. The resultant yellow crystals were washed with CH_2Cl_2 and dried under vacuum to yield $(Zn_4O)_3(BDC\text{-}C_6H_5N_2)_3(BTB)_4$ (0.190 g, 87%).

Synthetic procedure for $(Zn_4O)_3(BDC\text{-}C_6H_5N_2PdCl_2)_3(BTB)_4$. 100 mg of $(Zn_4O)_3(BDC\text{-}C_6H_5N_2)_3(BTB)_4$ was placed in a 20 ml vial immersed in 10 ml of anhydrous CH_2Cl_2. 0.20 g of $PdCl_2(CH_3CN)_2$ was added causing the yellow crystals to turn dark purple. The reaction mixture was allowed to stand unperturbed for 12 hours, after which the dark purple crystals were washed with CH_2Cl_2 and dried to yield $(Zn_4O)_3(BDC\text{-}C_6H_5N_2PdCl_2)_3(BTB)_4$ (0.098g, 85%)

Elemental analysis: Calcd for $C_{50}H_{28}N_2O_{13}Zn_4PdCl_2$: C, 46.07; H, 2.16; N, 2.15; Pd, 8.16; Zn, 20.06. Found: C, 44.28; H, 2.16; N, 2.94; Pd, 8.84; Zn, 22.09.

Synthetic procedure for the model compound: Dichloro(N-(2-pyridylmethylene)aniline-N,N')Palladium(II). 2.0g of (E)-N-((Pyridin-2-yl)methylene)benzenamine was reacted with $PdCl_2(CH_3CN)_2$ in acetone for 2 hrs. The resulting orange powder, dichloro(N-(2-pyridylmethylene)aniline-N,N')Palladium(II) (1.45g), was filtered dried in air and used without further purification.

XAS Data collection.

XAS measurements were conducted at the Stanford Synchrotron Radiation Laboratory (SSRL) with the SPEAR storage ring containing between 80 and 100 mA at 3.0 GeV. Pd Kedge data were collected on the structural molecular biology XAS beamline 7-3 operating with a wiggler field of 2 T. A Si(220) double-crystal monochromator was used. Beamline 7-3 is equipped with a rhodium-coated vertical collimating mirror upstream of the monochromator, and a downstream bent-cylindrical focusing mirror (also rhodium-coated). Harmonic rejection was accomplished by detuning the intensity of the incident radiation at the end of the scan by 50%. Incident and transmitted X-ray intensities were monitored using argon or nitrogen-filled ionization chambers. X-ray absorption was measured in transmittance mode. During data collection, samples were maintained at a temperature of approximately 10K using an Oxford instruments liquid helium flow cryostat. For each sample, three scans were accumulated, and the energy was calibrated by reference to the absorption of a Pd foil measured simultaneously with each scan, assuming a lowest energy inflection point of 24349.0 eV. The energy threshold of the extended X-ray absorption fine structure (EXAFS) oscillations was assumed to be 24370 eV.

XAS data analysis.

The EXAFS oscillations $\chi(k)$ were quantitatively analyzed by curve-fitting using the EXAFSPAK suite of computer programs[12] as previously described[13,14] using abinitio theoretical phase and amplitude functions calculated using the program FEFF version 8.25.[15,16] No smoothing, filtering or related operations were performed on the data.

Powder X-Ray diffraction.

Powder X-ray diffraction data were collected using a Bruker D8-Discover θ-2θ diffractometer in reflectance Bragg-Brentano geometry employing Ni filtered Cu Kα line focused radiation at 1600 W (40 kV, 40 mA) power and equipped with a Vantec Line detector. Radiation was focused using parallel focusing Gobel mirrors. The system was also outfitted with an antiscattering shield that prevents incident diffuse radiation from hitting the detector, preventing the normally large background at $2\theta < 3$. Samples were mounted on zero background sample holders by dropping powders from a wide-blade spatula and then leveling the sample with a razor blade. Samples were prepared by dissolving small amounts of the material in methanol followed by sonication for 10 min. The precipitate was then filtered before collecting data.

Mass spectrometry.

Samples of $(Zn_4O)_3(BDC\text{-}C_6H_5N_2)_3(BTB)_4$ were dissolved in MeOH and ESI-MS was run in the negative ion mode.

Gas Adsorption measurements.

Low-pressure Ar adsorption isotherms were measured volumetrically on an Autosorb-1 analyzer (Quantachrome Instruments). A liquid argon bath (87 K) was used for the measurements. The Ar and He gases used were UHP grade. From the Ar adsorption isotherms, the BET surface areas (accessible surface area) and total pore volumes of each material have were calculated. The pore volume of each material was estimated from the Dubinin-Radushkevich (DR) model with the assumption that the adsorbate is in the liquid state and the adsorption involves a pore-filling process. To estimate pore size distributions for MOFs, Ar isotherms were analyzed using nonlocal density functional theory (NLDFT) implementing a hybrid kernel for Ar adsorption at 87 K based on a zeolite/silica model containing cylindrical pores.[17] For porosity measurements, as-synthesized $(Zn_4O)_3(BDC\text{-}C_6H_5N_2)_3(BTB)_4$ was immersed in acetone for 24 h, during which the activation solvent was replenished three times. The sample was evacuated with supercritical CO_2 in a Tousimis Samdri PVT-3D critical point dryer.[18] The acetone-containing sample was placed in the chamber and acetone was exchanged with liquid CO_2. The chamber containing the sample and liquid CO_2 was then heated to approximately 40 ºC and kept under supercritical conditions (typically 1300 psi) for 1 h. The CO_2 was slowly vented (ca. 1 h) from the chamber at approximately 40 ºC, yielding porous material.

Results and Discussion

Synthesis and metalation of UMCM-1-NH$_2$ $(Zn_4O)_3(BDC\text{-}NH_2)_3(BTB)_4$. UMCM-1-NH$_2$ was selected for metalation because it offers large pores (30.7 Å, 23.2 Å) and is suitable for postmodification since it contains amine functionalities (**Figure 1**). UMCM-1-NH_2 was synthesized and activated using the synthetic conditions reported in the literature.[10] PXRD and Ar isotherms at 87 K showed that UMCM-1-NH_2 had an analogous structure to the reported UMCM-1-NH_2, respectively (**Figure 2-3**). In addition, it was possible to scale this MOF to produce quantities suitable for postmodification.

The amine functionality of UMCM-1-NH_2 was reacted with 1.5 equivalents of 2-pyridinecarboxaldehyde in anhydrous toluene over 5 days to form an iminopyridine moiety (**Figure 4**). Elemental analysis confirmed that reaction proceeded to completion to yield $(Zn_4O)_3(BDC\text{-}C_6H_5N_2)_3(BTB)_4$. In addition, the mass spectrum of the digested product showed the parent ion peak for the iminopyridine moiety at m/z 269 ($[M\text{-}H]^-$) confirming the postmodification of the framework (**Figure 5**). Upon activation of the framework, PXRD data confirmed that the crystallinity of the framework was maintained and the structure was topologically identical to UMCM-1-NH_2 (**Figure 2**). Furthermore, porosity was maintained as evidenced by the Argon isotherm at 87 K, highlighting the advantage of selecting a MOF with large pores (**Figure 3**).

The iminopyridine offers an ideal binding moiety for metal centers within the MOF framework. The addition of Pd (II) was achieved by addition of $Pd(CH_3CN)_2Cl_2$ to $(Zn_4O)_3(BDC\text{-}C_6H_5N_2)_3(BTB)_4$ to yield a fully metalated MOF $(Zn_4O)_3(BDC\text{-}C_6H_5N_2PdCl_2)_3(BTB)_4$. Following activation of the framework, the porosity was accessed by adsorption and the surface area was found to be 1700 m^2/g (BET) (**Figure 3**). In addition, crystallinity was maintained (**Figure 2**) confirming that the structure was maintained throughout the metal binding.

Conformation of metal binding. Elemental analysis confirmed the expected ratio of Zn:Pd (4:1) for a fully metalated framework; however, this did not confirm the position of the palladium in the MOF. The palladium sites incorporated are crystallographically disordered across the MOF framework, making determination of positions from the single crystal data impossible. Therefore two techniques were used to characterize the metal binding site, EXAFS and XANES. Both these techniques rely on absorption of X-rays and excitation of electrons within the K-edge of the palladium metal. Firstly, XANES (**Figure 6**) confirms the near edge of the MOF is analogous to that of a model compound ($PdCl_2(C_{13}N_2H_{10})$) and not the starting material $PdCl_2(CH_3CN)_2$. Secondly, a Fourier transform of EXAFs data was carried out (**Figure 7**); this allowed the determination of the immediate coordination environment of the palladium center, giving characteristic bond lengths of two Pd-Cl and two 2 Pd-N ligands at 2.276(2) and 1.993(2) Å, respectively (**Figure 8**). XANES and EXAFS data confirm the coordination environment of the metal center within the MOF, in a square planar geometry.

Conclusion

Expansion of coordination chemistry to the solid state remains a challenge to carry out and characterize. Within this chapter, we show that postmodification is a suitable technique for incorporating coordination complexes into a MOF. Furthermore, we use a combination of concise X-ray absorption spectra techniques to characterize the metal binding environment. By selection of a MOF with large pores and suitable organic functionalities, it was possible to incorporate a well-defined metal site into the MOF framework. X-ray techniques including EXAFs and XANEs were used to characterize the metal binding within the MOF, the expected coordination environment was obtained.

Throughout the organic transformations crystallinity was maintained as evidenced by retention of crystallinity and porosity. However, a reduction in porosity was observed in the final metalated product, which suggested a loss of some long-range order in metalated UMCM-1-NH_2. This resulted from consecutive transformations of the framework in this zinc based MOF. This loss of porosity highlights the importance of using chemically stable frameworks in postmodification applications in the future. The development of metalation by postmodification is a technique that can be applied to a wide range of MOFs. The ability to incorporate metal complexes in MOFs will allow the use of MOFs in a broader range of applications, including gas adsorption and catalysis.

Figures

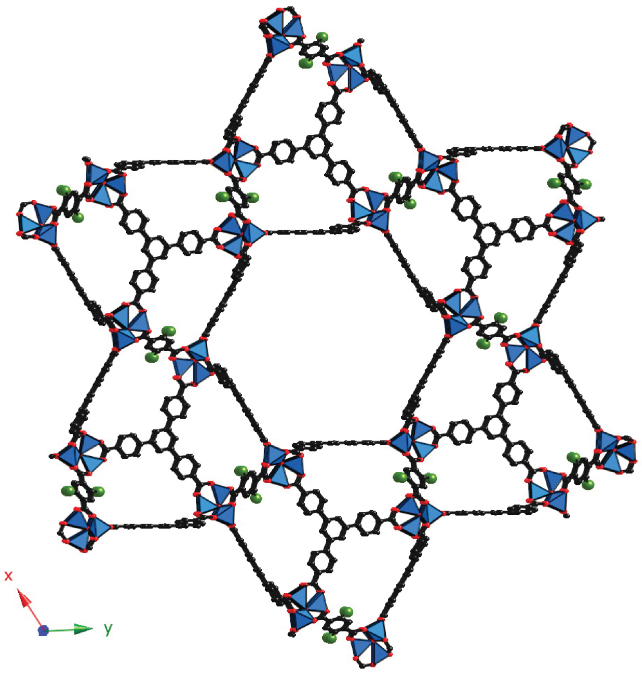

UMCM-1-NH_2

$(Zn_4O)_3(BDC\text{-}NH_2)_3(BTB)_4$

Space group = P6(3)/m

a = 41.25 Å

c = 17.50 Å

V = 25808 $Å^3$

Figure 1) Structure of UMCM-1-NH_2

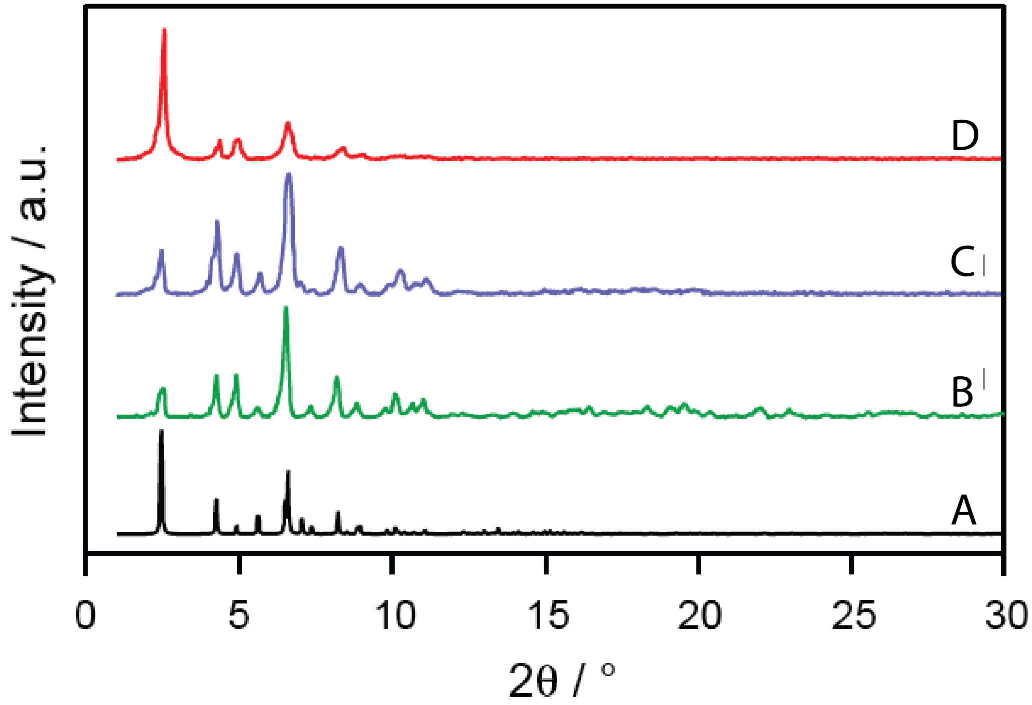

Figure 2) Powder X-ray diffraction (PXRD). A) Simulated PXRD of UMCM-1-NH_2, B) PXRD of UMCM-1-NH_2, C) PXRD of UMCM-1-NH_2-imine, and D) UMCM-1-NH_2-Pd.

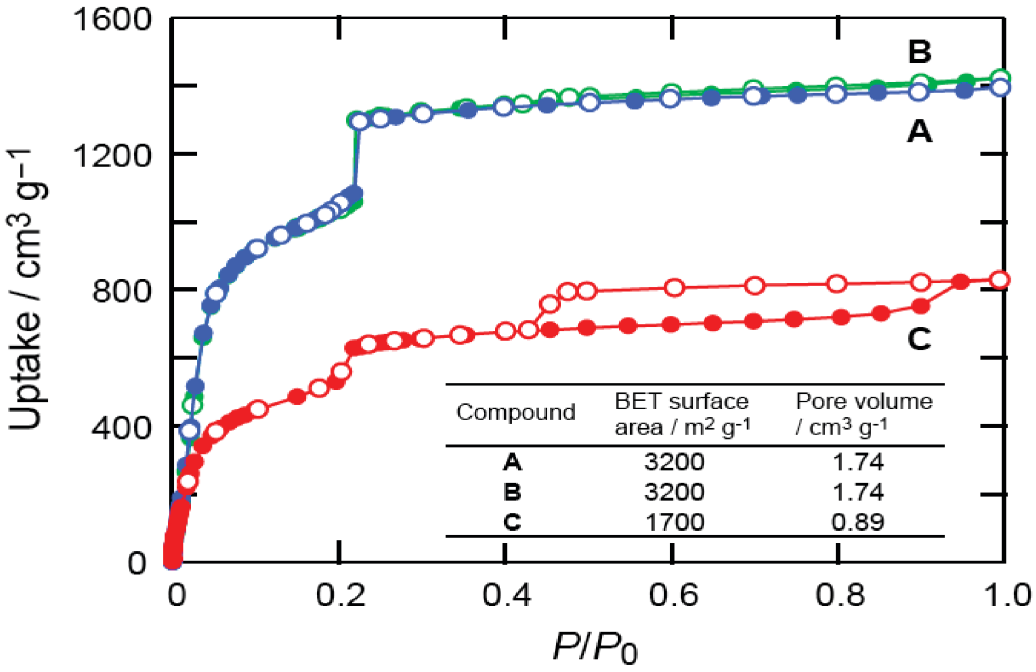

Compound	BET surface area / m^2 g^{-1}	Pore volume / cm^3 g^{-1}
A	3200	1.74
B	3200	1.74
C	1700	0.89

Figure 3) Argon gas adsorption isotherms for A (UMCM-1-NH_2), B (UMCM-1-Imine), and C (UMCM-1-Pd) at 87 K, with adsorption and desorption points represented by solid and open circles, respectively.

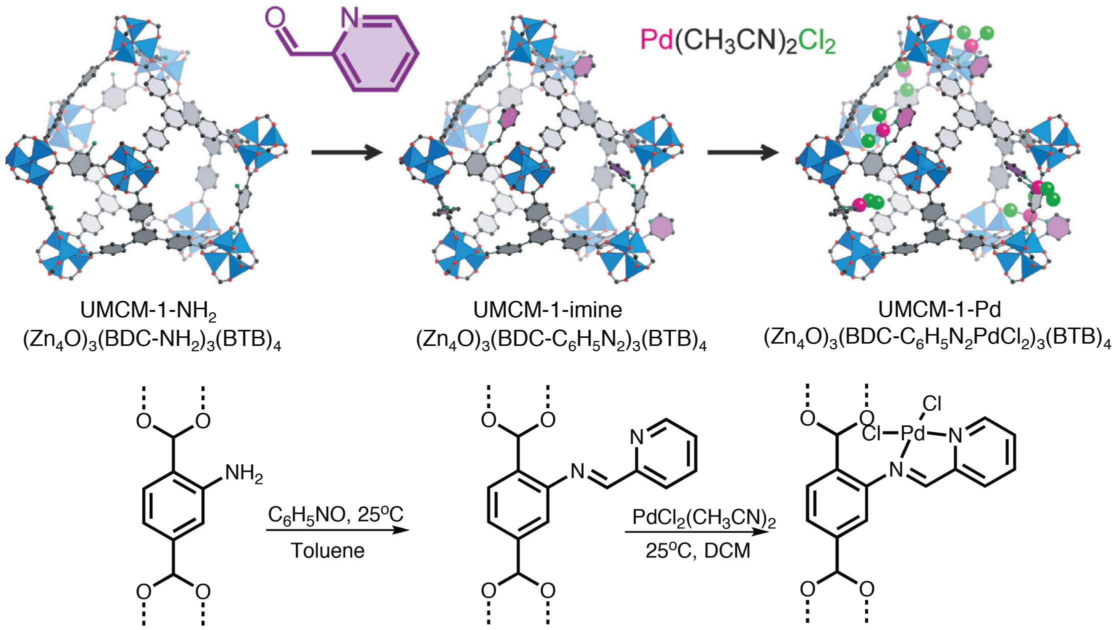

Figure 4) Isoreticular metalation of UMCM-1NH$_2$ followed by metalation. A) metalation of one cage of UMCM-1-NH$_2$ B) Organic transformations carried out on one organic link of UMCM-1-NH$_2$.

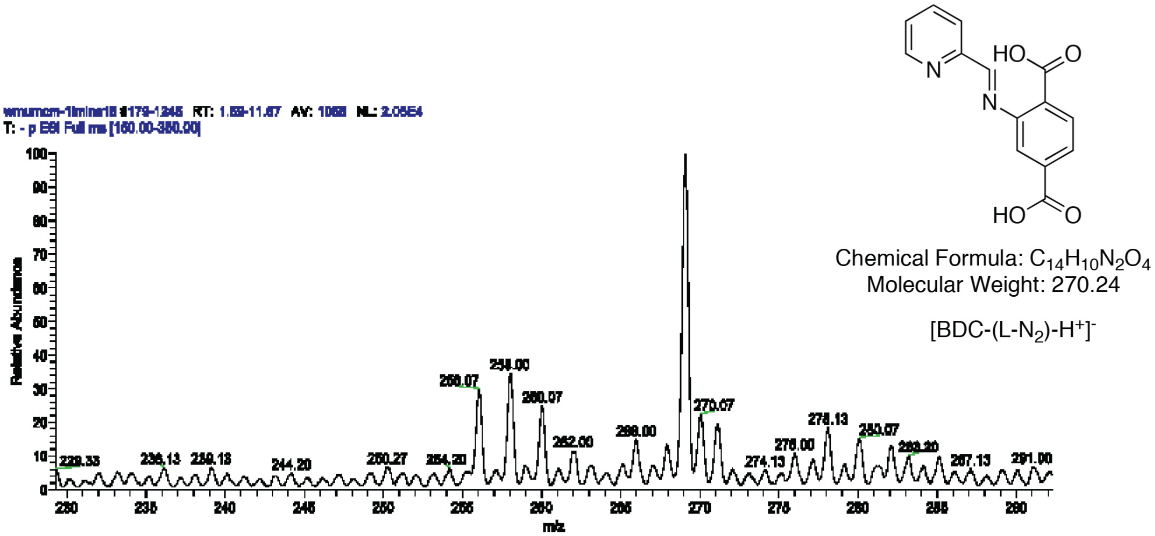

Figure 5) ESI mass spectrum of imine ligand fragment

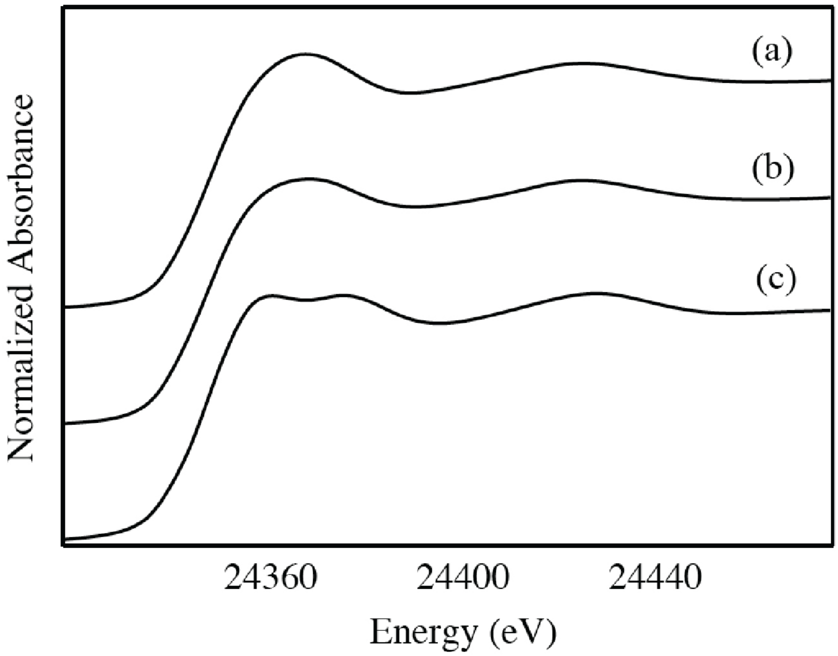

Figure 6) X-ray Absorption Near Edge Structure of a) Dichloro(N-(2-pyridylmethylene)aniline-N,N)Palladium(II) (Model compound) b) $(Zn_4O)_3(BDC-C_6H_5N_2PdCl_2)_3(BTB)_4$ (UMCM-1-Pd) c) $PdCl_2(CH_3CN)_2$ (starting material)

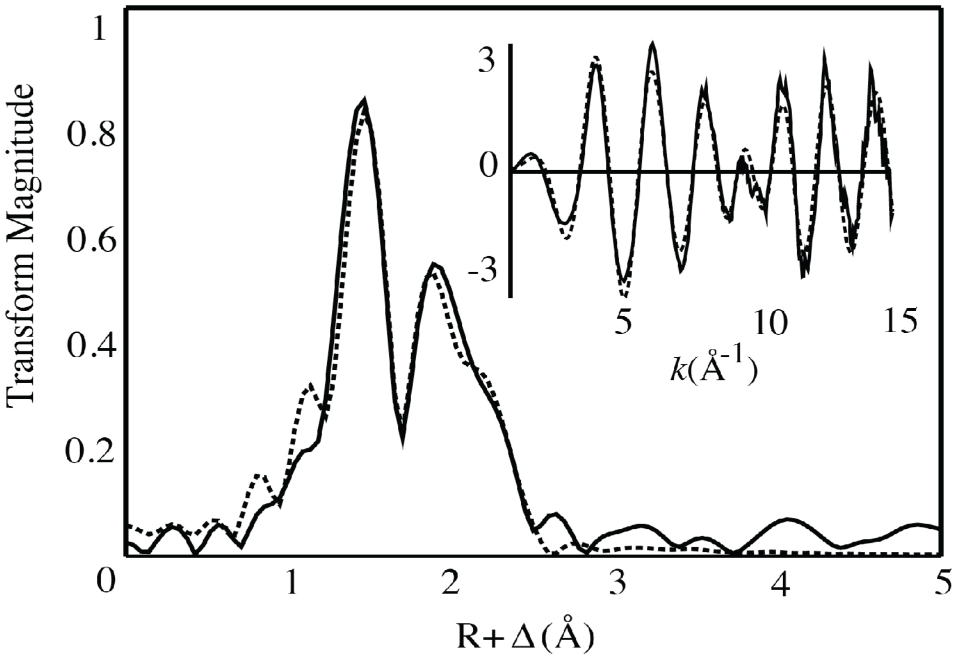

Figure 7) Pd K-edge EXAFS Fourier transforms and (inset) EXAFS spectra for C. Solid lines show the experimental data and dotted lines show the best fits using the parameters given in Table 1.

Tables

Table 1) EXAFS curve-fitting parameters[a]

N	R	σ^2	N	R	σ^2	N	R	σ^2	ΔE_0	F
Pd—Cl			Pd—N			Pd—C				
2	2.276(2)	0.0052(1)	2	1.993(2)	0.0013(1)	2	2.793(4)	0.0040(7)	-17.4(9)	0.273

[a] Coordination numbers, N, interatomic distances R (Å), Debye-Waller factors σ^2 (Å^2), and threshold energy shifts ΔE_0 (eV). Values in parentheses are the estimated standard deviations (precisions) obtained from the diagonal elements of the covariance matrix. The accuracies will be much greater than these values, and numbers and Debye-Waller factors. The fit-error function F is defined as $F = \sqrt{\sum k^6 \left(\chi_{calc} - \chi_{expt}\right)^2 / \sum \chi_{expt}^2}$, where the summations are over all data points included in the refinement.

References

1) Grubbs, R. H. Angewandte Chemie, International Edition **2006**, 45,23, 3760-3765
2) Caravan, P.; Ellison, J. J.; McMurry, T. J.; Lauffer, R. B. Chemical Reviews **1999**, 99, 2293-2352.
3) Rosenberg, B.; VanCamp, L.; Trosko, J. E.; Mansour, V. H. *Nature.* **1969**, 222, 385-6.
4) Corma, A. Chemical Reviews, 1997, 97, 2373-2419
5) Lee, J.; Kim, J.; Hyeon, T. Advanced Materials. **2006**, 18, 2073-2094
6) (a) Eddaoudi, M.; Kim, J.; Rosi, N.; Vodak, D.; Wachter, J.; O'Keeffe, M.; Yaghi, O. M. *Science* **2002**, *295*, 469. (b) Banerjee, R.; Furukawa, H.; Britt, D.; Knobler, C.; O'Keeffe, M.; Yaghi, O. M. *J. Am. Chem. Soc.* **2009**, *131*, 3875. (c) Surble, S.; Serre, C.; Mellot-Draznieks, C.; Millange, F.; Ferey, G. *Chem. Commun.* **2006**, 284. (d) Wu, C.-D.; Ma, L.; Lin, W. *Inorg. Chem.* **2008**, *47*, 11446.
7) Shultz, A. M.; Farha, O. K.; Hupp, J. T.; Nguyen, S. T. *J. Am. Chem.Soc.* **2009**,

131, 4204. (b) Szeto, K. C.; Lillerud, K. P.; Tilset, M.; Bjorgen, M.; Prestipino, C.; Zecchina, A.; Lamberti, C.; Bordiga, S. *J. Phys. Chem.B* **2006**, *110*, 21509. (c) Szeto, K. C.; Kongshaug, K. O.; Jakobsen, S.; Tilset, M.; Lillerud, K. P. *Dalton Trans.* **2008**, 2054. (d) Mulfort, K. L.; Farha, O. K.; Stern, C. L.; Sarjeant, A. A.; Hupp, J. T. *J. Am. Chem. Soc.* **2009**, *131*, 3866.

8) Wu, C.-D.; Hu, A.; Zhang, L.; Lin, W. *J. Am. Chem. Soc.* **2005**, *127*, 8940.

9) Ingelson, M. J.; Barrio, J. P.; Guilbaud, J.-B.; Khimyak, Y. Z.; Rosseinsky, M. J. *Chem. Commun.* **2008**, 2680.

10) Wang, Z.; Tanabe, K. K.; Cohen, S. M. *Inorg. Chem.* **2009**, *48*, 296.

11) Morris, W.; Doonan, C.; Furukawa, H.; Banerjee, R.; Yaghi, O. M. *J. Am. Chem. Soc.*, **2008**, *130*, 12626-12627

12) http://ssrl.slac.stanford.edu/exafspak.html

13) George, G. N.; Garrett, R. M.; Prince, R. C.; Rajagopalan, K. V. *J. Am. Chem. Soc.***1996**, *118*, 8588-8592.

14) Doonan, C. J.; Stockert, A.; Hille, R.; George G. N. *J. Am. Chem. Soc.* **2005**, *127*, 4518-4522.

15) Rehr, J. J.; Mustre de Leon, J.; Zabinsky, S. I.; Albers, R. C. *J. Am. Chem. Soc.* **1991**,*113*, 5135-5140.

16) Mustre de Leon, J.; Rehr, J. J.; Zabinsky, S. I.; Albers, R. C. *Phys. Rev. B* **1991**, *44*, 4146-4156.

17) Ravikovitch, P. I.; Wei, D.; Chueh, W. T.; Haller, G. L.; Neimark, A. V. *J. Phys. Chem. B* **1997**, 101, 3671-3679.

18) Nelson, A. P.; Farha, O. K.; Mulfort, K. L.; Hupp, J. T. *J. Am. Chem. Soc.* **2009**, *131*,458-460.

Chapter 4

Synthesis and postmodification of UiO-66-A a hydrolytically stable zirconium MOF

In 2008 the first zirconium based MOF was reported; UiO-66 ($Zr_6(OH)_4O_4(BDC)_6$, has 6 Å pore sizes (**scheme 1**).[1] The structure of this microcrystalline powder was derived from powder X-ray diffraction data and was shown to have the **fcu** topology (**Scheme 1**). The pore sizes of this MOF could be varied by increasing the number of phenyl rings in the organic link; by increasing the number of phenyl rings, UiO-67 ($Zr_6(OH)_4O_4(BPDC)_6$ and UiO-68 ($Zr_6(OH)_4O_4(TPDC)_6$ were formed. UiO-67 and UiO-68 both have the **fcu** topology and the pores are 8 Å and 10 Å, respectively. These variable pore metrics are coupled with exceptional chemical stability in solvents, including water. The high stability of this MOF is due to the high stability of the metal oxide unit, which is comprised of highly oxophilic zirconium in a high oxidation state. The high chemical stability of the MOF combined with variable pore metrics, make UiO-66 and its analogs attractive for postmodification. The high chemical stability will allow a range of organic conditions to be exploited in the postmodification of this MOF. In addition, the variable pore metrics could potentially be used to prevent pore blocking on postmodification of zirconium based MOFs.

Scheme 1) Structure of the **fcu** topology, UiO-66, and UiO-67

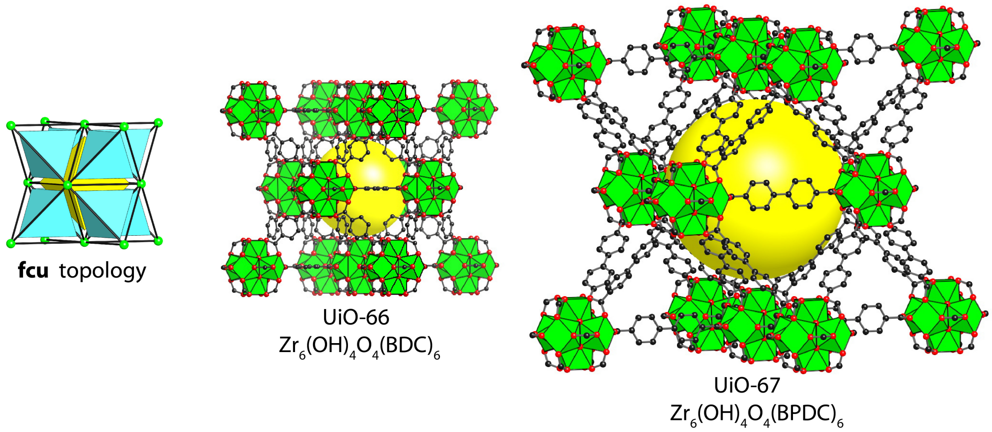

UiO-66 is not suitable for postmodification as it does not contain any organic functionality that can be covalently modified. Therefore the synthesis of new zirconium MOFs essential for suitability for postmodification. Isoreticular expansion and modification of MOFs has been extensively investigated; for example, the IRMOF series of zinc-based MOFs have been readily modified whilst maintaining the same underlying structure (**Scheme 2**).[2] In this chapter, isoreticular modification was applied to zirconium based MOFs to produce a framework suitable for postmodification, UiO-66-A $Zr_6(OH)_4(O_4(BDC\text{-}NH_2)_4(BDC\text{-}NH_3^+Cl^-)_2$. This framework was shown to be isoreticular with UiO-66 by investigation of X-ray diffraction, incorporating amine functionalities suitable for postmodification. Postmodification of amines has been extensively studied in IRMOF-3, a zinc based MOF. [3] However, these reactions are limited by the chemical stability of the zinc based MOF.[3] Therefore we chose to attempt chemical reactions that require a chemically stable Zr-MOF. The initial reaction that was targeted was reversible imine formation, which requires water as a reagent. Imine condensation reactions proceed between an aldehyde and an amine to form an imine; the equilibrium of this reaction can be controlled by addition of water to the reaction. Addition of water would normally lead to MOF breakdown; however, zirconium based MOFs are stable in water.[1] In the chemically stable MOF we hoped to demonstrate reversible binding to the surface of the MOF for the first time. Postmodification reactions yielded a different product, a hemiaminal, which is the intermediate of the reaction between an aldehyde and an amine.[4] This hemiaminal was found to be in a thermal equilibrium with an aziridine ring, a pathway atypical of reactions between aldehydes and amines.

Scheme 2) Isoreticular modifications of MOF-5.[2]

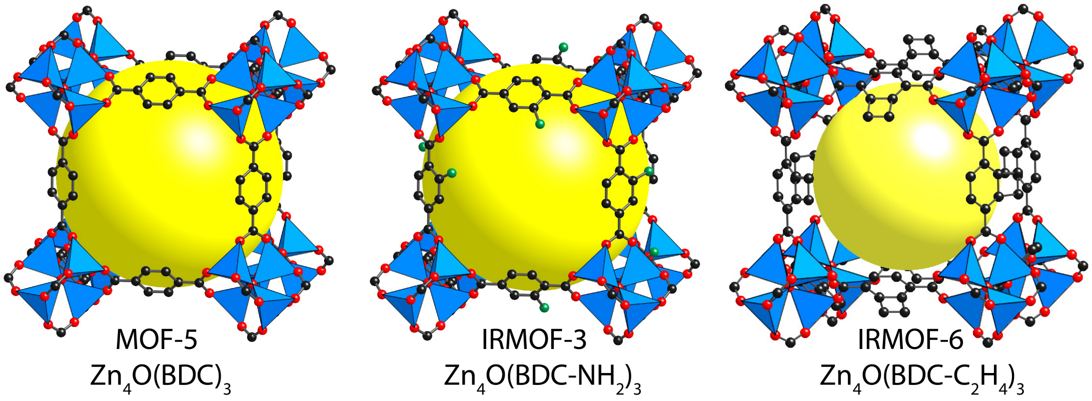

MOF-5 $Zn_4O(BDC)_3$

IRMOF-3 $Zn_4O(BDC\text{-}NH_2)_3$

IRMOF-6 $Zn_4O(BDC\text{-}C_2H_4)_3$

Many techniques have been used to characterize postmodification reactions in MOFs, including digestion of the MOF and analyzing the resulting solution, ^{13}C CP/MAS solid state NMR, and FTIR. These techniques have limitations; FTIR and ^{13}C CP/MAS solid state NMR offer no information about yield. Digestion techniques destroy the MOF frameworks under harsh acidic or basic conditions, making digestion unsuitable for characterizing reaction that are acid and base sensitive. Therefore the development of further techniques to characterize transformations in MOF frameworks is paramount. In this study, ^{15}N enrichment of organic units is used to provide information about reactions on the MOF with aldehyde containing molecules. ^{15}N solid state NMR is used at each stage of postmodification to characterize the transformations around the nitrogen containing amine center.

MOFs with high porosity have been used for the adsorption of gases including CO_2, CH_4, O_2, and H_2.[5] However, the application of MOFs for adsorption of corrosive gases including H_2S and NH_3 remains limited, as adsorption of these gases leads to degradation of the MOF.[6] For example, NH_3 adsorption in MOF-5 has been investigated with initial adsorption showing uptake of 300 mol/g.[6] However, subsequent ammonia adsorption is seen to reduce to zero, rendering the MOF useless as a reversible adsorption material. Therefore chemically stable frameworks must be investigated for their corrosive gas adsorption properties. Within this chapter we have investigated the NH_3 adsorption of chemically stable UiO-66-A and its postmodified analogs, which show reversible ammonia adsorption. Furthermore, adsorption of ammonia does not result in a loss of crystallinity as evidenced by PXRD.

Experimental

Materials and general procedures

All reagents unless otherwise stated were obtained from commercial sources (Alfa Aesar, Cambridge isotope laboratories, Sigma Aldrich, TCI) and were used without further purification. Yields reported were unoptimized. Elemental microanalyses were performed at the University of California, Los Angeles, Department of Chemistry and Biochemistry.

Synthesis of labeled compound

Diethyl 2-nitroterephalate-^{15}N. Labeled ^{15}N potassium nitrate (1.191g, 11.7 mmol) was added to nitromethane (10 mL) and stirred at room temperature. To the solution was added trifluoromethanesulfonic acid until the potassium nitrate was fully dissolved. Phosphorus pentoxide (3.43g, 27.8 mmol) was added to the solution. To the solution was added diethyl 2-terephthalate acid (1.5g, 6.8 mmol) in 10 mL of nitromethane. The solution was heated at 50 ˚C for 8 hrs. Upon cooling, water (50 mL) was slowly added to the solution to quench the unreacted phosphorus pentoxide. The solution was extracted with CH_3NO_2 (3x 20 ml). The organic phase was removed under reduced pressure to yield diethyl 2-nitroterephalate (1.3g, 4.9 mmol) yield 72 %.

Diethyl 2-aminoterephthalate -^{15}N. Diethyl 2-nitroterephthalate (1.3g, 4.9 mmol) was dissolved in dry tetrahydrofuran (50 mL) and placed in a Parr high-pressure reactor. To the solution was added Pd/charcoal (10% 0.1g) and the reaction was sealed. The reaction was pressurized to five bar with hydrogen, and stirred for 24 hrs at room temperature. The reaction mixture was filtered through celite to remove the Pd on carbon and washed with an excess of tetrahydrofuran. The organic phase was removed under reduced pressure to yield diethyl 2-aminoterephthalate (1.1g, 4.6 mmol) yield 94 %.

2-aminoterephthalic acid-^{15}N. Diethyl 2-aminoterephthalate (1.1g 4.6 mmol) was dissolved in methanol (35 mL) and water (15 mL). To the reaction was added potassium hydroxide (1.84g, 46 mmol); the reaction was stirred at room temperature for 24 hrs. The MeOH/H_2O was removed under reduced pressure and the precipitate was redissolved in a amount of minimum amount of water; 2-aminoterephthalic acid was precipitated out of the solution by addition of excess HCl (1 M). The product was isolated by filtration and washed with water (5 x 50 mL) to yield a yellow solid (0.7g, 3.8 mmol) yield 83 %

Synthesis of UiO-66-A

2-aminoterephthalic acid (0.543, 3 mmol) was added to N,N-dimethylformamide (10 mL) and fully dissolved. $ZrCl_4$ (0.233g, 1 mmol) was fully dissolved in *N*,*N*-dimethylformamide (30 mL). The two solutions were combined and heated at 120 ˚C for 24 hrs to form a microcrystalline powder. The microcrystalline powder was collected by filtration and washed with DMF (3 x 10 mL) over a thirty-minute period. The DMF was then replaced with MeOH (5 x 30 mL) over a five-day period. Finally, the volatile MeOH was removed by heating at 120 ˚C under vacuum (30 mtorr) for 48 hrs.

Postmodification of UiO-66-A

UIO-66-B. Activated UiO-66-B (0.3g) was added to $CHCl_3$ 20 mL and acetaldehyde 0.5 mL. The reaction mixture was allowed to stand at room temperature for 48 hrs. The solvent was initially exchanged with $CHCl_3$ (3 x 20 mL) over a thirty-minute period and then $CHCl_3$ (3 x 20 mL) over a three-day period to remove excess acetaldehyde. The compound was evacuated (30 mtorr) at room temperature for 24 hrs.

UiO-66-C UiO-66-B was heated to 85 ˚C under vacuum to form UiO-66-C.

Structure resolution from Powder X-Ray Diffractrometry of UiO-66-A (PXRD)

Powder X-ray data were collected using a Bruker D8-Discover θ-2θ diffractometer in reflectance Bragg-Brentano geometry employing Ni filtered Cu Kα line focused radiation at 1600 W (40 kV, 40 mA) power and equipped with a Vantec Line detector. Radiation was focused using parallel focusing Gobel mirrors. The system was also outfitted with an anti-scattering shield that prevents incident diffuse radiation from hitting the detector, preventing the normally large background at $2\theta < 3$. Samples were mounted on zero background sample holders by dropping powders from a wide-blade spatula and then leveling the sample with a razor blade. To determine the structure of UiO-66-A, crystal structure modeling was carried out, followed by Rietveld refinement.

Crystal structure modeling. The model for UiO-66-A, including cell parameters and atomic positions, was generated using Materials Studio chemical structure-modeling software[7] employing the Crystal Building module. The structure was generated using the relevant space group, the cell parameters were used as obtained, and atom positions were generated from the refined data of UIO-66.[8] The calculated structure was minimized with the Forcite module using the Geometry Optimization routine with the Universal force field (UFF).[8] The obtained model was used as the input for the Rietveld refinement.

Solid state ^{13}C/^{15}N CP/MAS nuclear magnetic resonance spectroscopy.

High Resolution solid-state nuclear magnetic resonance (NMR) spectra were recorded at ambient pressure on a Bruker DSX-300 spectrometer using a standard Bruker magic angle-spinning (MAS) probe with 4 mm (outside diameter) zirconia rotors. The magic angle was adjusted by maximizing the number and amplitudes of the signals of the rotational echoes observed in the ^{79}Br MAS FID signal from KBr.

Cross-polarization with MAS (CP/MAS) was used to acquire ^{13}C data at 75.47 MHz. The ^{1}H and ^{13}C ninety-degree pulse widths were both 4 ms. The CP contact time varied from 1.5 to 5 ms. High power two-pulse phase modulation (TPPM) ^{1}H decoupling was applied during data acquisition. The decoupling frequency corresponded to 72 kHz. The MAS sample-spinning rate was 10 kHz. Recycle delays between scans varied between 3 and 10 s, depending upon the compound as determined by observing no apparent loss in the ^{13}C signal from one scan to the next. The ^{13}C chemical shifts are given relative to tetramethylsilane as zero ppm, calibrated using the methylene carbon signal of adamantane assigned to 37.77 ppm as the secondary reference.

^{15}N CP MAS for the isotopically labeled materials were measured at 30.42 MHz. The ^{1}H and ^{15}N ninety-degree pulse widths were both 4 μs. The CP contact time varied from 1.5 to 5 ms. The direct excitation NMR was measured at recycle delays of up to 45 seconds to allow for complete relaxation. The ^{15}N chemical shifts are given relative to liquid N2 at zero ppm, calibrated using the nitrogen signal of glycine assigned to 36.2 ppm as the secondary reference.

^{15}N solution NMR spectra.

High Resolution solution nuclear magnetic resonance (NMR) spectra were recorded at ambient pressure on a Bruker 500 spectrometer

N_2 adsorption at 77 k.

Low-pressure gas adsorption isotherms were measured volumetrically on an Autosorb-1 analyzer (Quantachrome Instruments). A liquid nitrogen sample bath (77 K) was used for N_2 measurements. The N_2 gas used was UHP grade. For measurement of the apparent surface areas (S_{BET}), the BET method was applied using the adsorption branches of the N_2 isotherms assuming a N_2 cross-sectional area of 16.2 Å^2/molecule.

NH_3 adsorption at 298 k.

Low-pressure gas adsorption isotherms were measured volumetrically on an Autosorb-1 analyzer (Micromeritics). A constant temperature bath (298 K) was used for NH_3 measurements. The NH_3 gas used was high purity grade.

Results and Discussion

A new zirconium MOF was synthesized, UiO-66-A. UiO-66 was synthesized by reaction of 2-aminoterephthalic acid (0.543, 3 mmol) and $ZrCl_4$ (0.233g, 1 mmol) in *N*,*N*-dimethylformamide (40 mL). The solution was heated at 120 ˚C for 24 hrs to form a microcrystalline powder. The microcrystalline powder was collected by filtration and washed with DMF (3 x 10 mL) over a thirty-minute period. The DMF was then replaced with MeOH (5 x 30 mL) over a five-day period. The volatile MeOH was removed by heating at 120 ˚C under vacuum (30 mtorr) for 48 hrs. This microcrystalline MOF was shown to be isoreticular in structure to UiO-66 by analysis of the PXRD (**Figure 1**). The structure and position of each atom in UiO-66-A was confirmed by modeling and Rietveld analysis of the PXRD, with good refinement parameters (**Figure 2**) (**Table 1-2**). UiO-66-A is comprised of highly stable zirconium metal oxide units $Zr_6(OH)_4O_4(CO_2)_{12}$ bridged by aminoterephthalic acid, which gives an **fcu** topology (**Figure 3**). The **fcu** topology is comprised of tetrahedral and octahedral units, which are arranged to give a face centered cubic cell with the space group Fm-3m and a = 20.781(3) Å (**Table 1**). The pore size of this crystal is analogous to that of UiO-66, 6 Å, which makes it more suitable than ZIF-90 for a wider range of postmodification reactions.[9] To confirm the permanent porosity of UiO-66-A, a N_2 isotherm at 77 K was measured, which showed a type I shape indicative of permanent microporosity. The surface area was derived by the BET method and found to be 820 m^2/g (**Figure 4**).

UiO-66-A was characterized by ^{13}C and ^{15}N cross polarization magic angle spinning (CP/MAS) NMR spectra. ^{13}C solid state NMR showed the expected resonances at 170 ppm for the carbonyl carbon atoms and the aromatic carbon atoms of the phenylene links 120 - 150 ppm (**Figure 5**). To carry out the ^{15}N NMR experiments a ^{15}N labeled aminoterephalic acid was prepared by a three-step reaction, nitration using labeled KNO_3, hydrogenation of the nitrogen to the amine, and deprotection of the terephalate to form aminoterephalic acid. ^{15}N NMR CP/MAS of UiO-66-A showed resonances at 56 ppm and 137 ppm, the amine and amine salt, respectively (**Figure 6**), which was confirmed by solution NMR of the protonated amine (**Figure 7**). The amine salt formed as a result of the acidic medium that was generated during the solvothermal synthesis. Direct excitation solid state NMR was carried out with a 45 second relaxation time, which showed a 2:1 yield of the free amine to the amine salt (**Figure 8-9**). This ratio was confirmed by elemental analysis, giving UiO-66-A an empirical formula of $Zr_6O_4{}^{(OH)_4(BDC\text{-}NH_2)_4(BDC\text{-}NH_3{}^{+Cl-})_2}$.

UiO-66-A with appended free amines and high chemical stability is suitable for postmodification. We chose to investigate the reaction of an amine and an aldehyde in an imine condensation reaction, and the reversible hydrolysis of the imine (**Figure 9**). The first step of this reaction, imine condensation, is known to proceed with retention of porosity and crystallinity in MOFs.[3] Due to the restricted nature of the UiO-66 pore, a small aldehyde-containing reagent, acetyl aldehyde (CH_3CHO) was selected for postmodification of UiO-66-A (**Figure 9**). UiO-66-A was reacted with acetyl aldehyde over two days in $CHCl_3$. After two days the solvent was decanted and washed with $CHCl_3$ five times, followed by evacuation at 25 °C and 30 mtorr for 24 hrs. Activation yielded a solvent-free framework, UiO-66-B.

The ^{15}N solid state NMR spectrum of UiO-66-B containing enriched nitrogen did not show the expected imine resonance at approximately 280 ppm. Instead, resonances at 93 and 71 ppm were observed. The peak at 93 ppm is attributable to a hemiaminal nitrogen

(**Figure 6**). To support this functional group assignment UiO-66-A was reacted with labeled acetylaldehyde $^{13}CH_3{}^{13}CHO$. Solid state NMR of the product showed resonances at 85 and 49 ppm due to the secondary and primary carbon atoms of the hemiaminal, respectively (**Figure 5**). The additional peak at 71 ppm in the ^{15}N NMR spectrum is consistent with the presence of an aziridine ring, which is also supported by the isotopically enriched ^{13}C MAS NMR spectrum in the resonance at 20 ppm (**Figure 5-6**). Integration of a direct excitation NMR spectrum with a relaxation time of 45 seconds gives approximate yields of each reaction with 3:5:2 (1:1.74:0.72) of the protonated amine, hemiaminal, and aziridine, respectively. Others have observed that under certain conditions, reactions of amines with aldehydes have yielded unexpectedly stable hemiaminals (**Figure 8-9**).[4]

Upon heating the sample to 100 ˚C for 12 hours an unexpected color change was observed with the formation of a green solid, UiO-66-C. The ^{15}N NMR spectrum showed a decreased intensity of the hemiaminal peak at 93 ppm and an increased intensity of the aziridine resonance at 71 ppm (**Figure 6**). An analogous result was observed in the ^{13}C solid state NMR spectrum with an increase in intensity of the peaks resulting from the aziridine and a decrease in intensity of peaks of the hemiaminal (**Figure 5-6**). To further investigate this thermal transformation direct excitation ^{15}N was used to probe the yield, corresponding to a yield of 3:1:5 (1:0.28:1.68) for the protonated amine: hemiaminal: aziridine (**Figure 8-9**).

To confirm that each reaction preceded with maintenance of crystallinity and porosity the PXRD and N_2 isotherms were measured, respectively. The PXRD of UiO-66-B and UiO-66-C showed that each sample maintained the **fcu** topology (**Figure 1**).

Furthermore, the N_2 adsorption isotherm at 77 K demonstrated that UiO-66-B and UiO-66-C retained porosity confirming the advantage of a larger pored system (**Figure 3**). The BET surface area of UiO-66-B and UiO-66-C was found to be 780 and 800 m^2/g, respectively. No reduction is seen in crystallinity or porosity highlighting the advantage of a chemically stable framework for postmodification.

To further utilize the stability of the zirconium framework we chose to investigate the ammonia adsorption of UiO-66-A and its postmodified analogs, UiO-66-B and UiO-66-C. Ammonia adsorption in other MOFs has been shown to rapidly degrade the framework rendering it unsuitable for reversible ammonia adsorption. However, we hoped that due to the high chemical stability of UiO-66-A-C reversible ammonia adsorption would not lead to framework degradation. Ammonia isotherms were measured at 298 K for UiO-66-A, UiO-66-B, and UiO-66-C (**Figure 10**). The uptake capacity at 760 torr was found to be, 134 cm^3/g, (UiO-66-A); 159 cm^3/g, (UiO-66-B); 193 cm^3/g, (UiO-66-C). Following adsorption and desorption PXRD patterns were measured, which showed retention of crystallinity, confirming that the structure was not degraded upon ammonia adsorption (**Figure 11**).

Conclusion

A new zirconium-based framework suitable for postmodification was synthesized and shown to have the **fcu** topology from analysis of the PXRD data. Labeling of aminoterephalic acid with a ^{15}N label revealed that UiO-66-A contained a free amine and its salt. The framework was shown to have a surface area of 820 m^2/g and a pore diameter of 6 Å making it suitable for postmodification.

UiO-66-A was postmodified by addition of acetylaldehyde to form UiO-66-B, which was found to contain a hemiaminal and aziridine functionalities. These functionalities were confirmed by ^{15}N CP/MAS solid state NMR and ^{13}C CP/MAS solid state NMR with labeled compounds being employed for extra sensitivity. Yields were determined by direct excitation ^{15}N solid state NMR. Upon heating UiO-66-B the equilibrium between the hemiaminal and aziridine is shifted towards the aziridine to form UiO-66-C. The shift in equilibrium is again observed throughout by solid state NMR. Retention of structure and surface area in UiO-66-B and UiO-66-C were confirmed by PXRD and N_2 adsorption at 77 K.

Ammonia adsorption was investigated in these exceptionally chemically stable frameworks. Ammonia adsorption has led to degradation of other frameworks; however, we hoped porosity would be maintained due to the chemical stability of the zirconium-based MOF. The ammonia adsorption of UiO-66-A-C was measured and found to proceed with maintenance of porosity and crystallinity.

Zirconium MOFs with variable pore metrics and high chemical stability are promising materials for postmodification and gas adsorption applications. Initial studies show that UiO-66-A can be postmodifed with retention of porosity and can adsorb gases that have degraded other MOFs, with retention of crystallinity. To increase the potential of Zr-MOFs in both these applications, pore metrics must be investigated; larger pores are investigated through isoreticular expansion and discovery of new topologies.

Figures

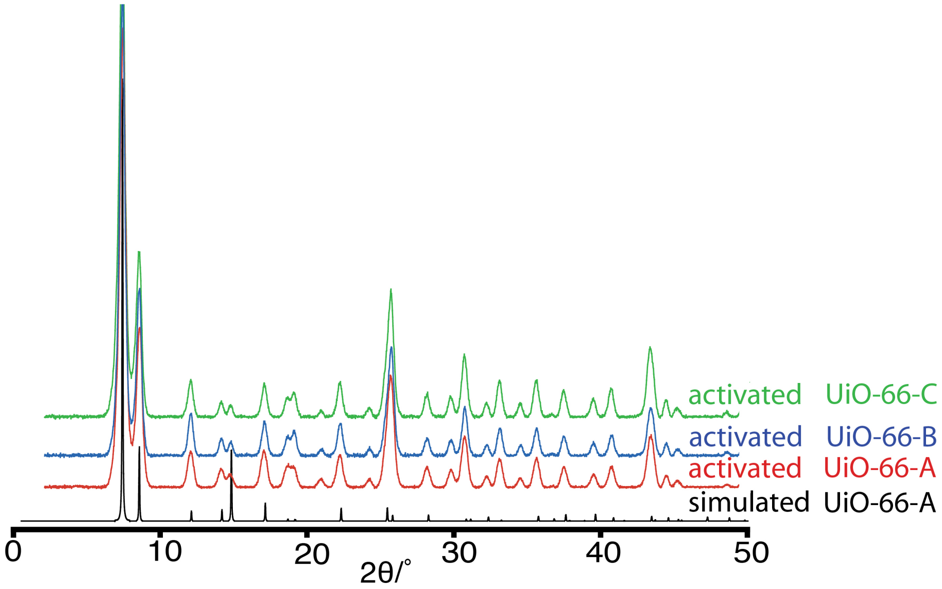

Figure 1) Powder X-ray diffraction patterns of UiO-66-A and the postmodified compounds (UiO-66-B and C). Simulated UiO-66-A (black), UiO-66-A (red), UiO-66-B (blue), and UiO-66-C (green).

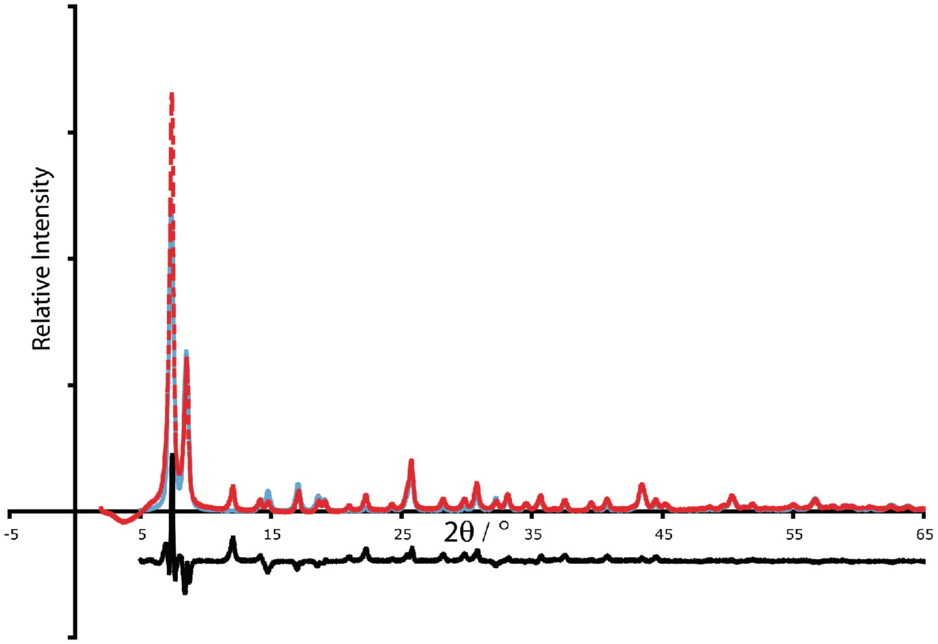

Figure 2) Rietveld analysis of UiO-66-A. Red dashed, experimental pattern; blue, calculated pattern; black, difference pattern (exp-calc).

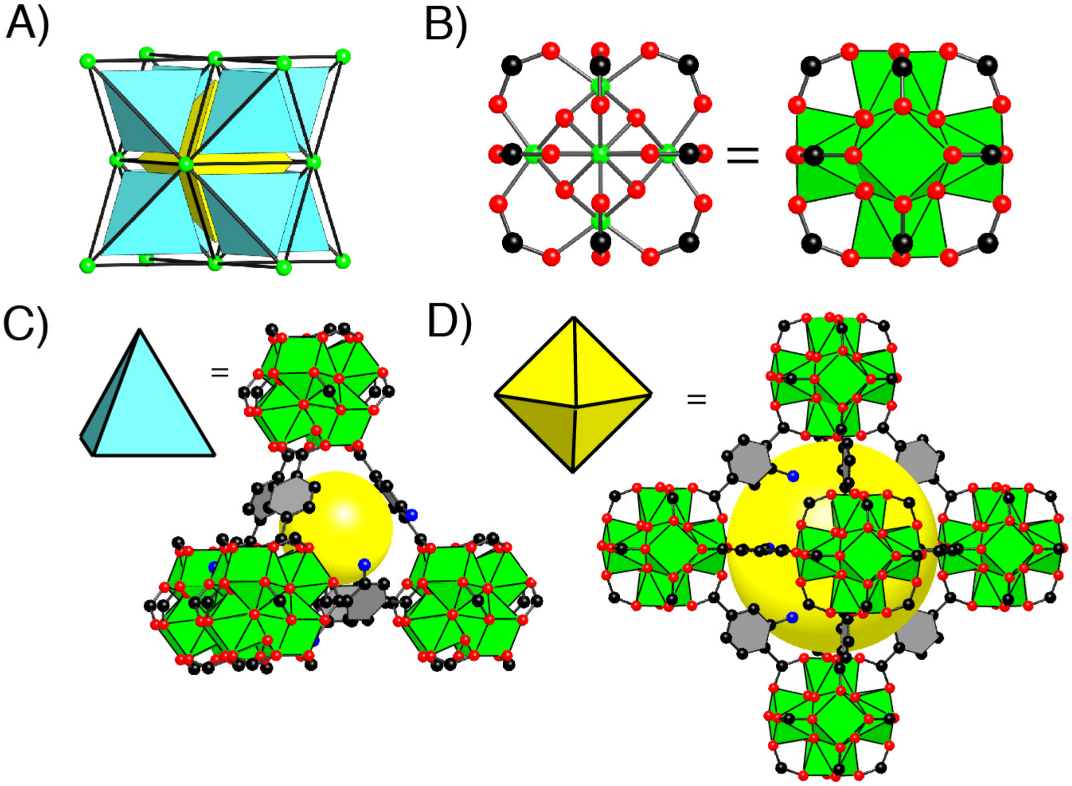

Figure 3) The crystal structure of UiO-66-A. (A) The tiling of the fcu unit showing the division of space into tetrahedra (green) and octahedra (yellow). Each yellow sphere and line represent the zirconium oxide unit and the organic linker, respectively. (B) A cube octahedral unit $Zr_6(OH)_4O_4(\text{-}CO_2)_{12}$ units of UiO-66-A. (C) A tetrahedral unit from the fcu net. (D) A octahedron unit from the fcu net. Pores in the evacuated crystalline frameworks are illustrated by yellow spheres that contact the van der Waals radii of the framework atoms.

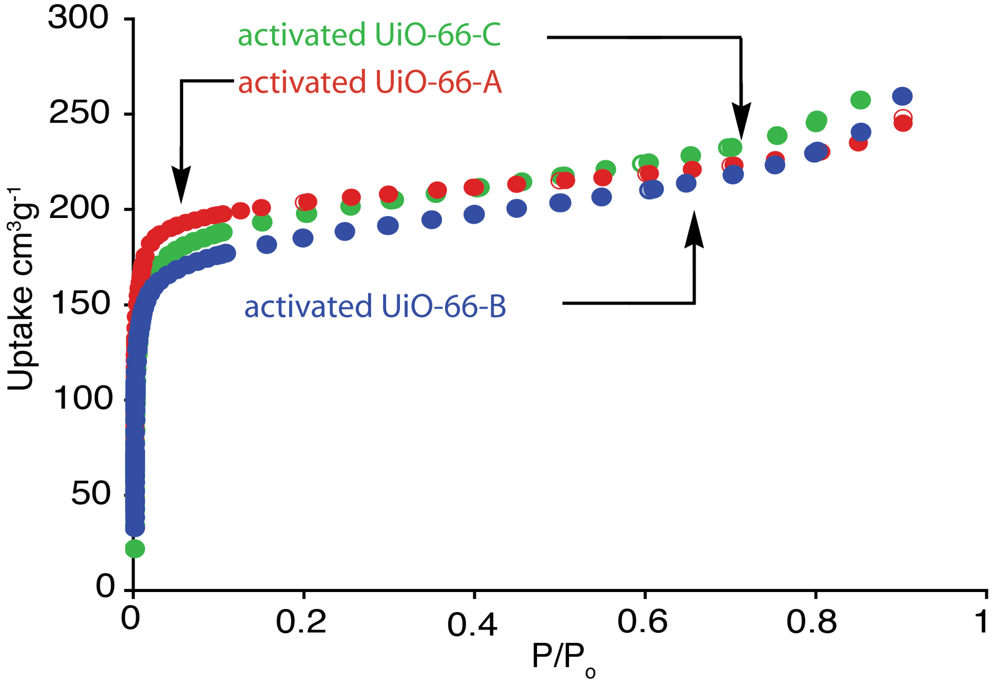

Figure 4) N_2 isotherm at 77 K of UiO-66-A and postmodified compounds. UiO-66-A (red), UiO-66-B (blue), and UiO-66-C (green).

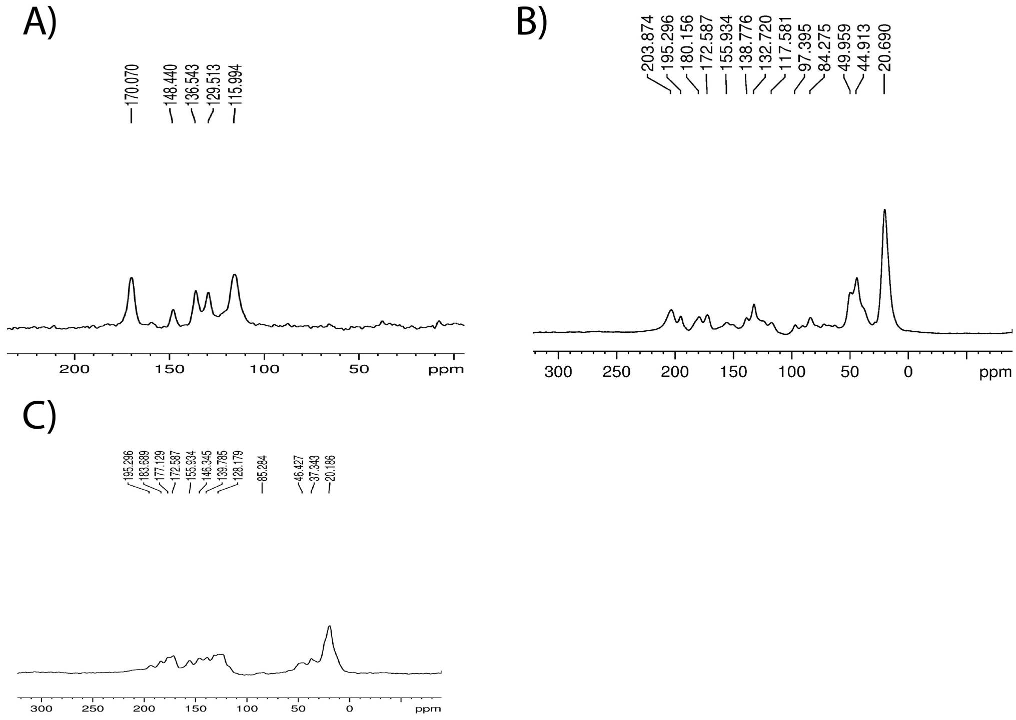

Figure 5) ^{13}C CP/MAS NMR of A) UiO-66-A, B) UiO-66-B, C) UiO-66-C.

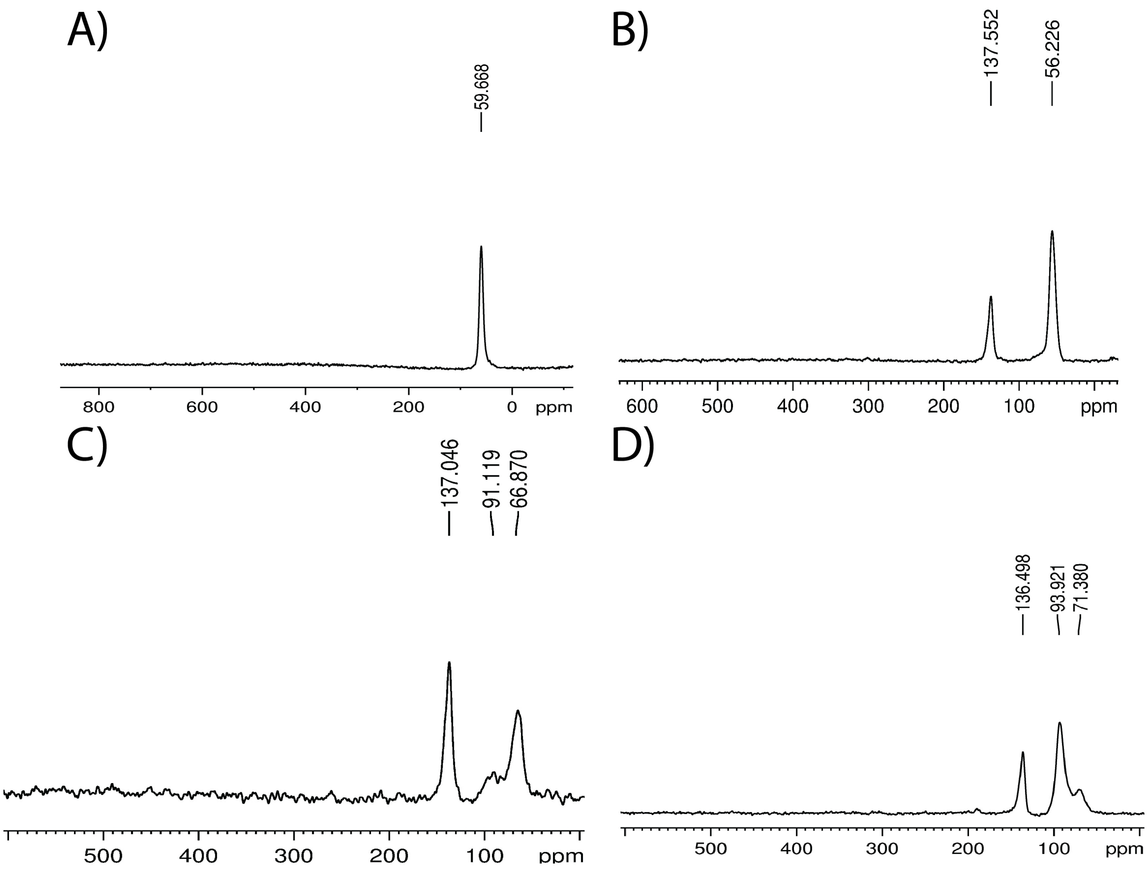

Figure 6) ^{15}N CP/MAS NMR of A) 2-aminoterephthalic acid, B) UiO-66-A, C) UiO-66-B, and D) UiO-66-C.

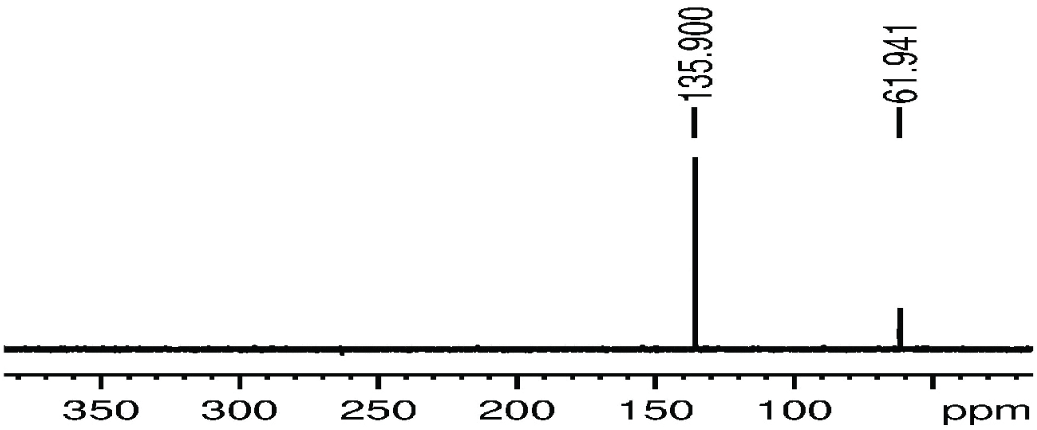

Figure 7) NMR spectra of 2-aminoterephalic acid in d6-acetone/DCl

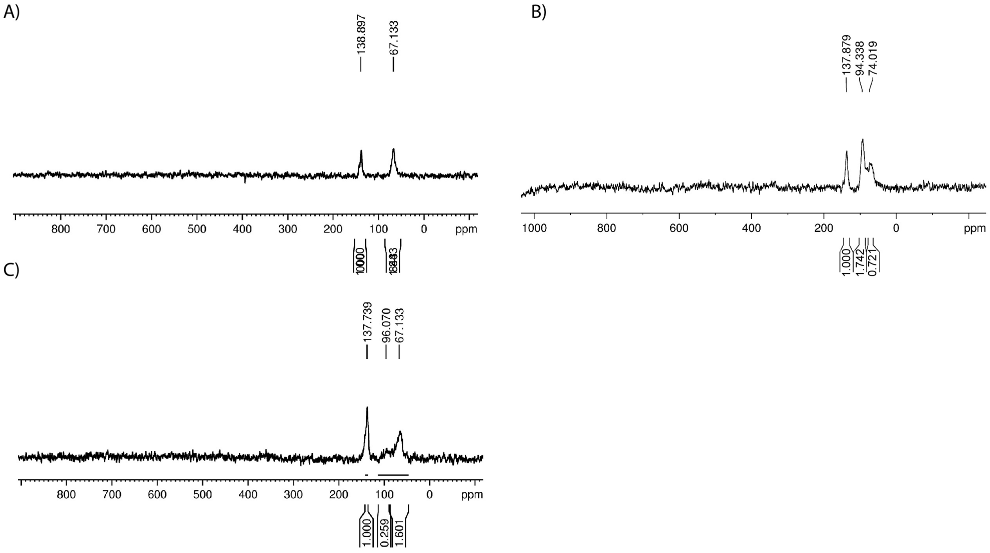

Figure 8) ^{15}N direct excitation NMR of A) UiO-66-A, B) UiO-66-B, C) UiO-66-C.

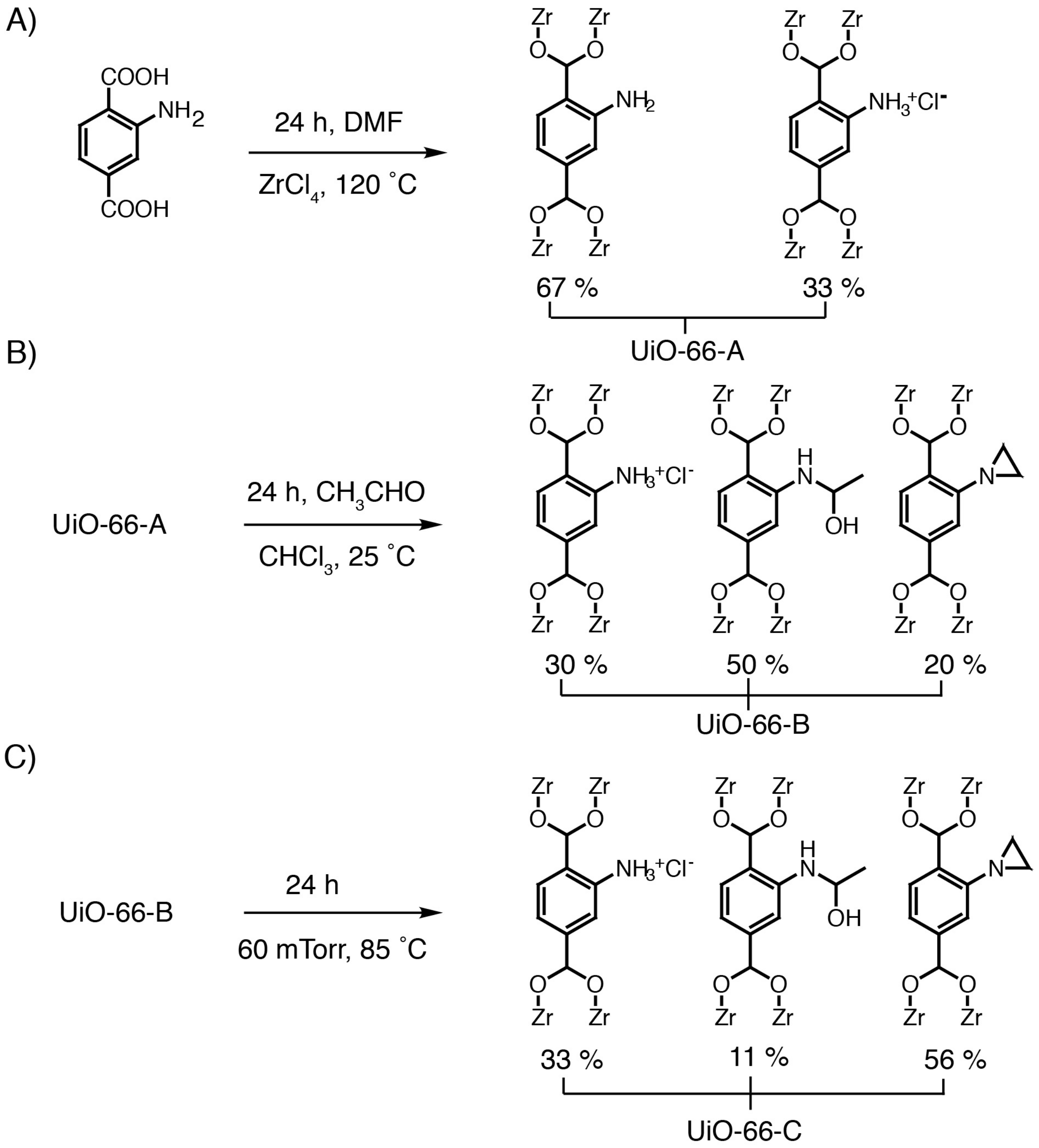

Figure 9) Synthesis and post modification of UiO-66-A.

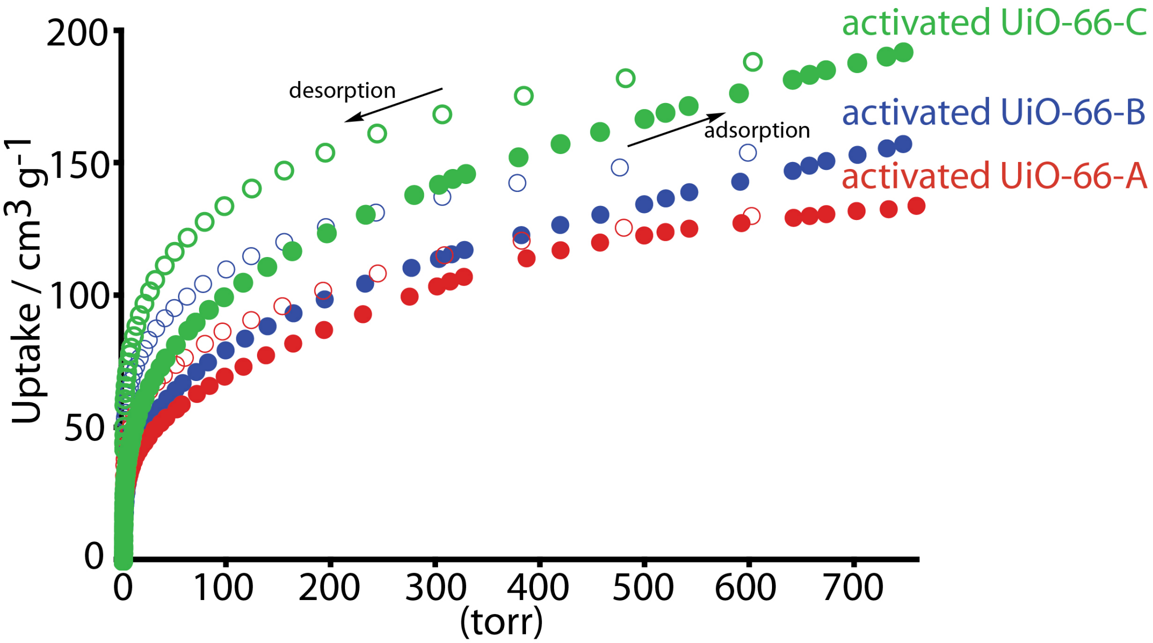

Figure 10) NH_3 isotherm at 298 K of UiO-66-A and postmodified compounds. UiO-66-A (red), UiO-66-B (blue), and UiO-66-C (green).

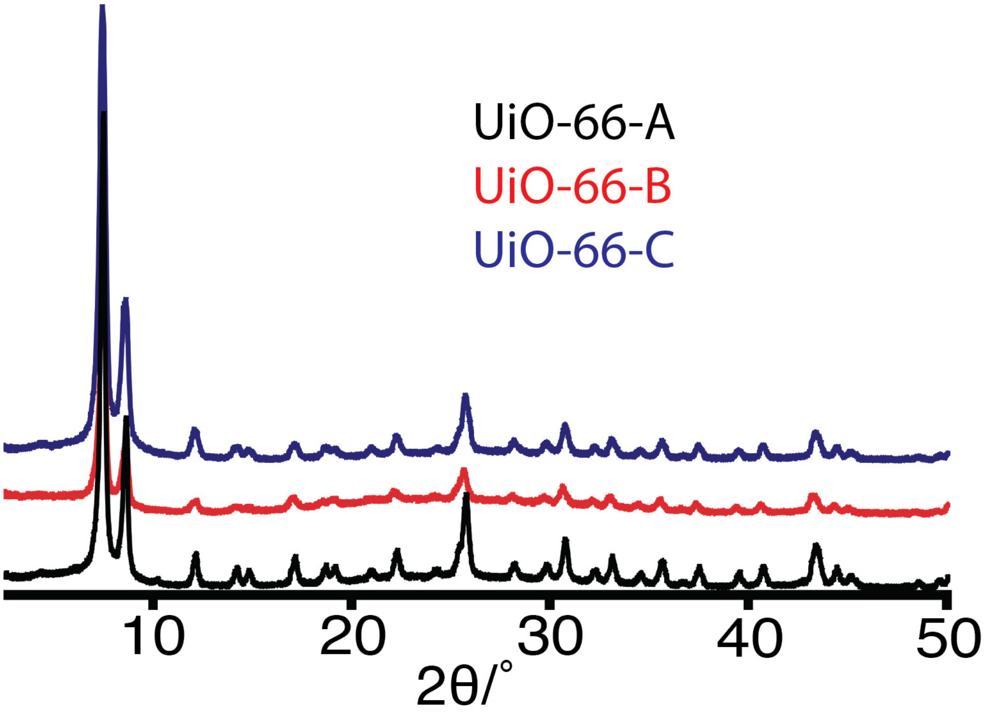

Figure 11) PXRD of UiO-66-A and postmodified compounds following ammonia adsorption. UiO-66-A (red), UiO-66-B (blue), and UiO-66-C (green).

Tables

<table>
<tr><td colspan="5">**UiO-66-A**</td></tr>
<tr><td colspan="2">Space Group
Fm-3*m* (Origin choice 1)
a = *b* = *c* = 20.781(3) Å
a = b = g = 90˚</td><td colspan="3">Volume
8974 $Å^3$</td></tr>
<tr><td>Atom</td><td>Occupancy</td><td>*X*</td><td>*Y*</td><td>*Z*</td></tr>
<tr><td>Zr1</td><td>1</td><td>0.11357</td><td>1.0000</td><td>0.00000</td></tr>
<tr><td>O2</td><td>1</td><td>0.16632</td><td>1.0000</td><td>0.08800</td></tr>
<tr><td>C3</td><td>1</td><td>0.26720</td><td>1.0000</td><td>0.18450</td></tr>
<tr><td>O4</td><td>1</td><td>0.05892</td><td>0.94108</td><td>-0.05892</td></tr>
<tr><td>C5</td><td>1</td><td>0.14820</td><td>1.0000</td><td>-0.14820</td></tr>
<tr><td>C6</td><td>1</td><td>0.20042</td><td>1.0000</td><td>0.20042</td></tr>
<tr><td>N7</td><td>0.25</td><td>0.28758</td><td>1.38141</td><td>0.50000</td></tr>
</table>

Table 1) Atom positions in UiO-66-A

Name	**UiO-66-A**
Composition	$Zr_{24}O_{32}N_{24}C_{192}H_{120}$
Mass Formula (g mol^{-1})	5469
Crystal system	Cubic
Space Group	*Fm*-3*m* (No. 225)
a (Å)	20.781(3)
V (Å^3)	8974
Crystal density (g cm^{-3})	1.27301(49)
Number of reflections	232
Number of independent atoms	7
R_p (%)	14.54
R_{wp} (%)	19.71
GOF (c^2)	11.92

Table 2) Refinement parameters from Rietveld refinement.

References

1. Cavka, J. H.; Jakobsen, S.; Olsbye, U.; Guillou, N.; Lamberti, C.; Bordiga, S.; Lillerud, K. P. *J. Am. Chem. Soc.* **2008**, *130*, 13850.
2. a) Rowsell, J. L. C.; Yaghi, O. M. *Microporous Mesoporous Mater.* **2004**, *73*, 3-14 b) Eddaoudi, M.; Kim, J.; Rosi, N. L.; Vodak, D. T.; Wachter, J. O'Keeffe, M.; Yaghi, O. M. *Science*. **2002**, *295*, 469-472

3. a) Wang, Z.; Cohen, S. M. *J. Am. Chem. Soc.* **2007**, *129*, 12368. (b) Wang, Z.; Cohen, S. M. *Chem. Soc. Rev.* **2009**, *38*, 72 (c) Doonan, C. J.; Morris, W.; Furukawa, H.; Yaghi, O. M. *J. Am. Chem. Soc.* **2009**, *131*, 9492.
4. Kawamichi, T.; Haneda, T.; Kawano, M.; Fujita, M. *Nature*. **2009**, *461*, 633.
5. Phan, A.; Doonan, C.; Uribe-Romo, F. J.; Knobler, C. B.; O'Keeffe, M.; Yaghi, O. M. *Acc. Chem. Res*. **2009**, 43, 58-67
6. Saha, D.; Deng, S. *J. Colloid Interface Sci.* **2010**, *348*, 615.
7. Materials studio version 5.0, 2009, Accelrys Software Inc.
8. A. K. Rappe, C. J. Casewit, K. S. Colwell, W. A. Goddard-III, W. M. Skiff. *J. Am. Chem. Soc*. **1992,** *114,* 10024-10035.
9. Morris, W.; Doonan, C.; Furukawa, H.; Banerjee, R.; Yaghi, O. M. *J. Am. Chem. Soc.* **2008**, *130*, 12626-12627

Chapter 5

Synthesis of Porphyrin Based Zirconium Metal-Organic Frameworks and their Metalation.

Introduction

Recently, a zirconium-based metal-organic framework was reported; UiO-66 ($Zr_6O_4(OH)_4(BDC)_6$), this framework has an **fcu** topology.[1] This MOF has high chemical stability due to the high connectivity and the oxophilic nature of the zirconium metal oxide unit, leading to stability in aqueous solvents and under acidic conditions. Studies of the expansion of the **fcu** topology by increasing the length of the organic link have been carried out, replacing H_2-BDC with H_2-BPDC and H_2-TPDC to form UiO-67 ($Zr_6O_4(OH)_4(BPDC)_6$) and UiO-68 ($Zr_6O_4(OH)_4(TPDC)_6$), respectively.[1] The expansion and structural analogs of these MOFs have been extensively studied because, of their high chemical stability. They maybe suitable for various applications including postmodification, gas storage, and catalysis.[2] However, limitations arise on expanding the link, in that framework interpenetration is observed. Interpenetration occurs when one framework grows within another; it was first observed in the MOF-5 topology; **pcu** (**Scheme 1A**).[3] UiO-66 has a topology that can interpenetrate, **fcu**; this limits the pore sizes, surface area, and applications of UiO-66 and its structural analogs.[4] Others have shown that interpenetration can be avoided by employing organic units with multiple points of extension, allowing to the crystallization in net topologies that do not interpenetrate.[5] For example, the use of the tritopic link H_3-BTB and the Zn_4O cluster leads to the synthesis of a different topology, the **qom** topology; this topology does not interpenetrate.[5] Because this topology does not interpenetrate, the expansion of the link within this topology leads to the formation of MOF-180 and MOF-200, which have record-breaking surface area.[5] In this chapter, highly stable zirconium metal oxide units were combined with links of multiple points of expansion, namely tetracarboxyporphyrin (H_4-TCPP). This combination permits the synthesis of new topologies which have high chemical stability, high surface area, and high porosity.

Scheme 1) Synthesis of two isoreticular series. A) The interpenetrating IRMOF series. B) The non-interpenetrating MOF-177 series.[3,5]

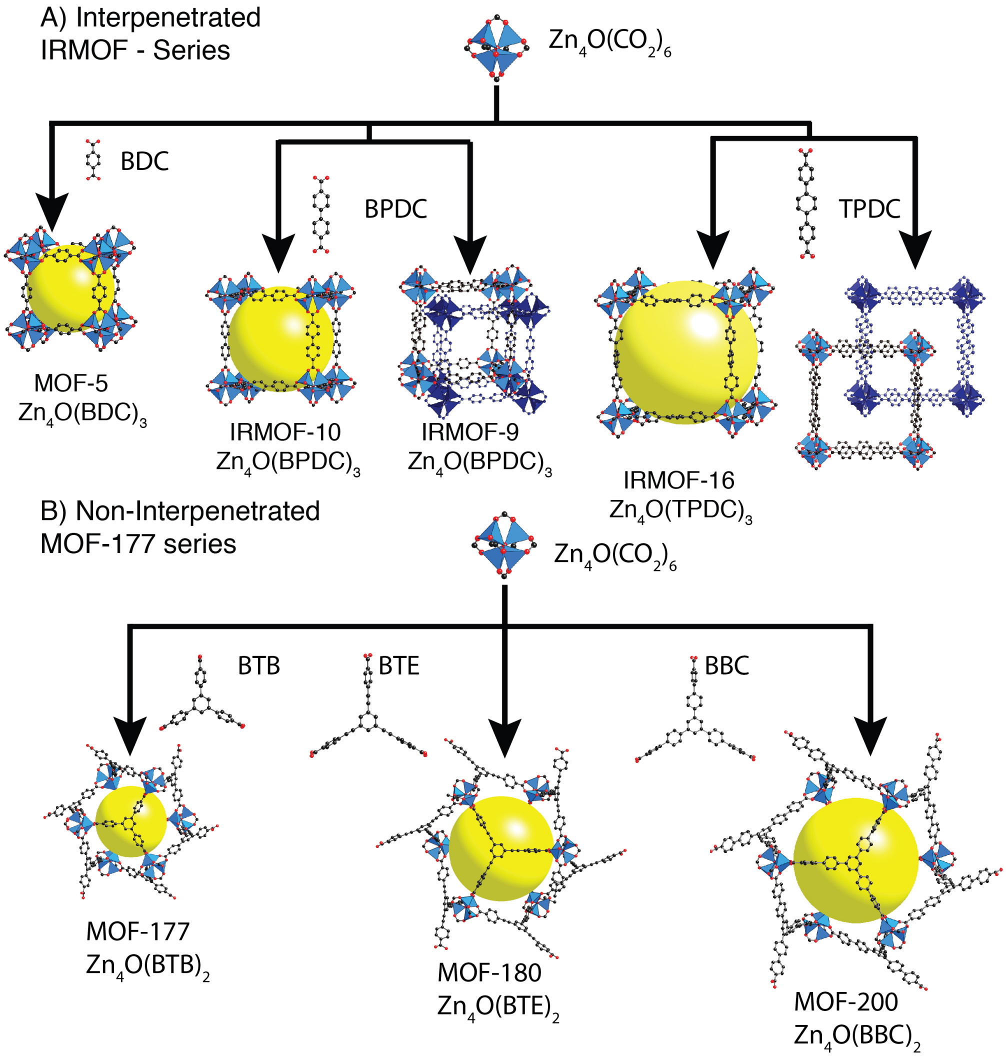

In addition to having four points of expansion, H_4-TCPP was selected because it contains a porphyrin binding site which is extensively known for its ability to bind metal centers.[6] The incorporation of open metal sites not integral to the MOF structure has been shown to enhance their gas adsorption and catalytic properties.[7] Multiple approaches including postmodification, removal of solvent from a metal oxide unit, and synthesis of organic units that contain predefined metal binding sites have been used to incorporate active metal binding sites into MOFs.[8] H_4-TCPP-H_2 with four points of extension contains a predefined porphyrin metal binding site. Over 100 porphyrin MOFs have been synthesized that contain porphyrin links. Many porphyrin MOFs are formed from geometrical arrays that prefer the formation of 2-D layers, limiting the porosity and the application of these MOFs because the porphyrin site is inaccessible.[9] Only a few examples of 3-D porphyrin-containing MOFs are known, often formed by employing bipyridine pillaring agents (**Scheme 2**).[10] In the few examples where exposed metalated porphyrins have been incorporated into MOFs the frameworks are catalytically active and adsorb gases selectively when they are exposed in MOFs.[10,11] One main limitation of currently known porphyrin MOFs is their chemical stability; for applications in gas adsorption and catalysis to be fully realized a chemically stable porphyrin MOF must be synthesized. In this chapter by employing an oxyphilic zirconium oxide unit with many points of extension, the synthesis of highly stable 3-D porphyrin MOFs has been successful. Furthermore, we show that the zirconium MOFs we have formed do not incorporate zirconium in the porphyrin unit H_4-TCPP-H_2, making these MOFs suitable for metal binding by two routes, pre-metalation and post-metalation.

Scheme 2) Structure of RPM MOFs.[10]

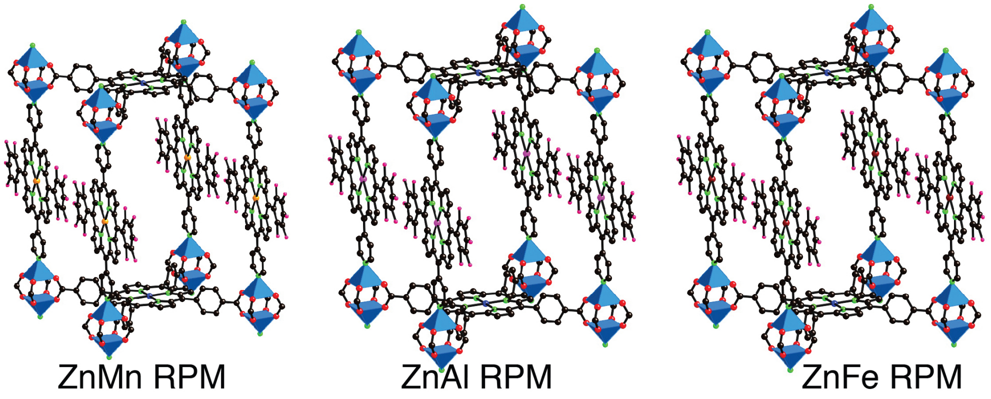
ZnMn RPM ZnAl RPM ZnFe RPM

In this chapter, the synthesis of three zirconium-based porphyrin MOFs are described, MOF-525, MOF-545, MOF-565 and one other extended Zr-MOF, MOF-535 (**Scheme 3**). The structures of MOF-535, MOF-545 and MOF-565 were resolved from single crystal diffraction data, resulting in the discovery of three new topologies **ftw**, **csq,** and **she**, respectively. MOF-525 was isolated as a microcrystalline powder, making it unsuitable for single crystal analysis. The structure was therefore resolved by using the reticular chemistry structural resource (RCSR) and analysis of its powder X-ray diffraction, which revealed an **ftw** topology.[12] The techniques used to resolve the structure of MOF-525 were adopted from covalent-organic frameworks, which crystallize as microcrystalline powders.[13] The structure of MOF-525, was analogous to that of MOF-535 which supported the structural assignment in the **ftw** topology. MOF-525 and MOF-545 were isolated as pure phases and metalated by two routes, pre-metalation and post metalation, to yield iron and copper MOFs, MOF-525-Cu, MOF-525-FeCl, MOF-545-Cu, and MOF-545-FeCl. The MOFs that contain porphyrins have exceptional surface area and chemical stability, making them ideal for applications in catalysis.

Scheme 3) Structures of MOF-525, MOF-535, MOF-545, and MOF-565.

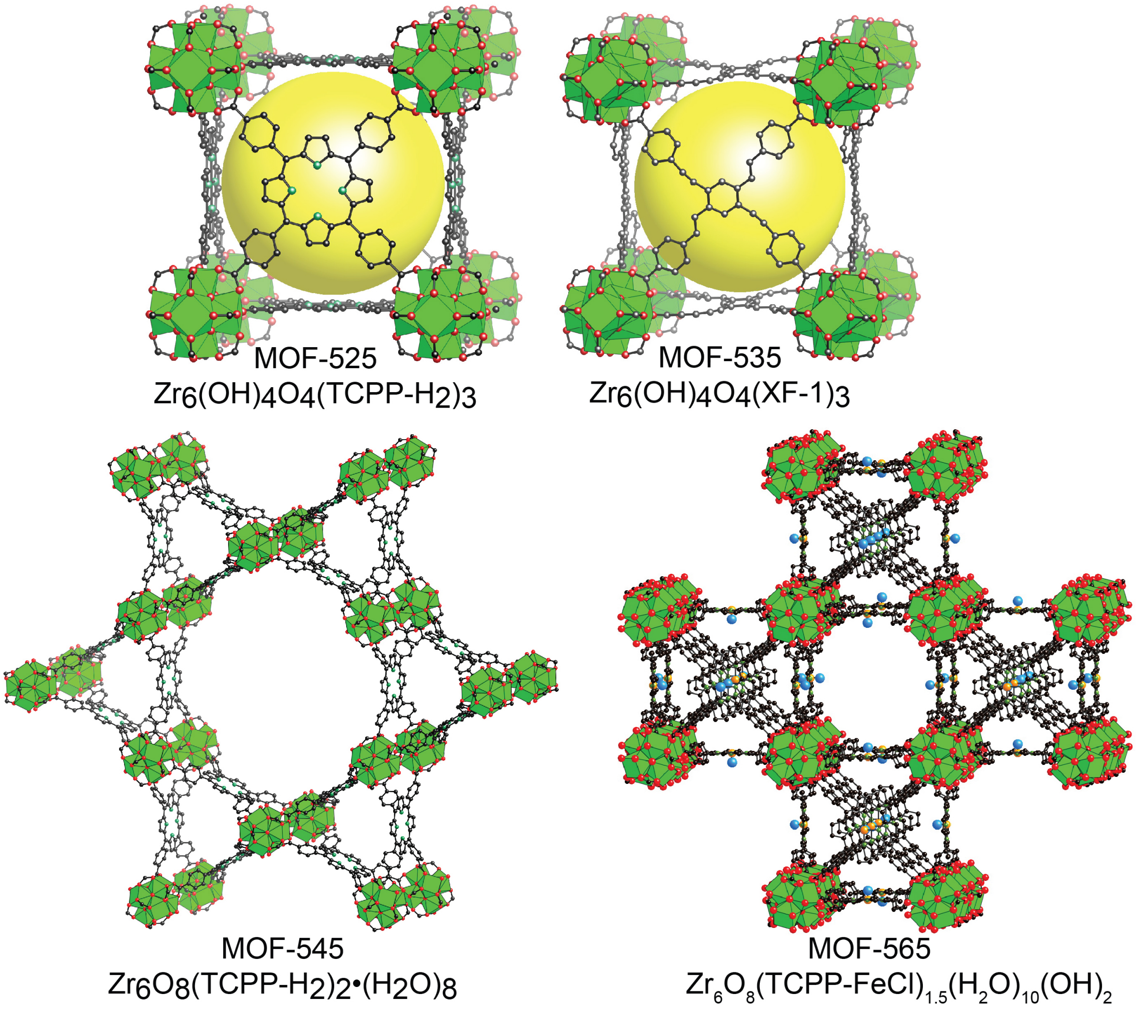

MOF-525
$Zr_6(OH)_4O_4(TCPP\text{-}H_2)_3$

MOF-535
$Zr_6(OH)_4O_4(XF\text{-}1)_3$

MOF-545
$Zr_6O_8(TCPP\text{-}H_2)_2\cdot(H_2O)_8$

MOF-565
$Zr_6O_8(TCPP\text{-}FeCl)_{1.5}(H_2O)_{10}(OH)_2$

Experimental

Materials and general procedures All reagents unless otherwise stated were obtained from commercial sources (Alfa Aesar, Cambridge Isotope Laboratories, Sigma Aldrich, TCI, and Frontier Scientific) and were used without further purification. The reported yields were unoptimized.

Synthesis of zirconium containing porphyrin MOFs and MOF-535

MOF-525 $Zr_6(OH)_4O_4(C_{48}N_4O_8H_{26})_3$ Zirconyl chloride octahydrate (12.5 mg, 0.037 mmol) was added to *N*,*N*-dimethylformamide (DMF, 10 mL) and sonicated for thirty minutes. Following sonication, tetrakis(4-carboxyphenyl)porphyrin (2.5 mg, 0.037 mmol) was added to the solution. After ten minutes further sonication, acetic acid (2.5 mL) was added to the solution. The solution was placed in a 20 mL scintillation vial and heated at 65 °C for three days. The microcrystalline powder was filtered and washed with DMF (5 × 10 mL) over a three-hour period. The DMF was then replaced with acetone (5 × 30 mL) over a five-day period. Finally, the volatile acetone was removed by heating at 120 °C under vacuum (30 mTorr) for 48 hrs.

MOF-525-Cu $Zr_6(OH)_4O_4(C_{48}N_4O_8H_{24}Cu)_3$ Zirconyl chloride octahydrate (12.5 mg, 0.037 mmol) was added to DMF (10 mL) and sonicated for thirty minutes. Following sonication, Cu(II) meso-tetra(4-carboxyphenyl)porphyrin (2.5 mg, 0.037 mmol) was added to the solution. After ten minutes further sonication, acetic acid (2.5 mL) was added to the solution. The solution was placed in a 20 mL scintillation vial and heated at 65 °C for three days. The microcrystalline powder was filtered and washed with DMF (5 × 10 mL) over a three-hour period. The DMF was then replaced with acetone (5 × 30 mL) over a five-day period. Finally, the volatile acetone was removed by heating at 120 °C under vacuum (30 mTorr) for 48 hrs.

MOF-535 $Zr_6O_4(OH)_4(C_{36}O_8H_{20})_3$ Zirconium tetrachloride (5.6 mg, 0.024 mmol) and acetic acid (2 mL) were added to DMF (10 mL) and sonicated for thirty minutes in a 20 mL scintillation vial. 4,4′-((1*E*,1′*E*)-(2,5-bis((4-carboxyphenyl)ethynyl)-1,4-phenylene)bis(ethene-2,1-diyl))dibenzoic acid) (H_4-XF, 16 mg, 0.024 mmol) added to the solution and dissolved by sonication. The reaction was heated at 60 °C for 4 hrs, followed by heating at 120 °C for two days. The single crystals were collected by filtration, and washed with DMF (5 × 10 mL) over a three-hour period. The DMF was then replaced with acetone (5 × 30 mL) over a five-day period. Finally, the volatile acetone was removed by heating at 100 °C under vacuum (30 mTorr) for 20 hrs.

MOF-545 $Zr_6(H_2O)_8O_4(C_{48}N_4O_8H_{26})_2$ Zirconyl chloride octahydrate (37.5 mg, 0.111 mmol) was added to DMF (10 mL) and sonicated for thirty minutes. Following sonication, tetrakis(4-carboxyphenyl)porphyrin (6.5 mg, 0.037 mmol) was added to the solution. After a further ten minutes of sonication, formic acid (7 mL) was added to the solution. The solution was placed in two 20 mL scintillation vials and heated at 130 °C for three days. The single crystals were collected by filtration and washed with DMF (5 × 10 mL) over a three-hour period. The DMF was then replaced with acetone (5 × 30 mL) over a five-day period. Finally, the volatile acetone was removed by heating at 120 °C under vacuum (30 mTorr) for 48 hrs.

MOF-545-Fe $Zr_6(H_2O)_8O_4(C_{48}N_4O_8H_{24}FeCl)_2$ Zirconyl chloride octahydrate (37.5 mg, 0.111 mmol) was added to DMF (10 mL) and sonicated for thirty minutes. Following sonication, Fe(III) meso-tetra(4-carboxyphenyl)porphyrin chloride (6.5 mg, 0.037 mmol) was added to the solution. After a further ten minutes of sonication, formic acid (5 mL) was added to the solution. The solution was placed in two 20 mL scintillation vials and heated at 130 °C for three days. The single crystals were collected by filtration and washed with DMF (5 × 10 mL) over a three-hour period. The DMF was then replaced with acetone (5 × 30 mL) over a five-day period. Finally, the volatile acetone was removed by heating at 120 °C under vacuum (30 mTorr) for 48 hrs.

MOF-545 $Zr_6(H_2O)_8O_4(C_{48}N_4O_8H_{24}Cu)_2$ Zirconyl chloride octahydrate (37.5 mg, 0.111 mmol) was added to DMF (10 mL) and sonicated for thirty minutes. Following sonication, Cu(II) meso-tetra(4-carboxyphenyl)porphyrin (6.5 mg, 0.037 mmol) was added to the solution. After a further ten minutes of sonication, formic acid (6 mL) was added to the solution. The solution was placed in two 20 mL scintillation vials and heated at 130 °C for three days. The single crystals were collected by filtration and washed with DMF (5 × 10 mL) over a three-hour period. The DMF was then replaced with acetone (5 × 30 mL) over a five-day period. Finally, the volatile acetone was removed by heating at 120 °C under vacuum (30 mTorr) for 48 hrs.

Postmetalation of MOF-525 to form MOF-525-Fe

MOF-525-Fe $Zr_6(OH)_4O_4(C_{48}N_4O_8H_{24}Fe)_3$ Iron chloride $FeCl_3$ (100 mg, 0.62 mmol) was dissolved in to DMF (10 mL). To the solution was added MOF-525 $Zr_6(OH)_4O_4(C_{48}N_4O_8H_{26})_3$ 50 mg, the solution was heated at 100 °C for 18 hrs. The microcrystalline powder was collected by filtration and washed with DMF (5 × 10 mL) over a three-hour period. The DMF was then replaced with acetone (5 × 30 mL) over a five-day period. Finally, the volatile acetone was removed by heating at 120 °C under vacuum (30 mTorr) for 48 hrs.

Single crystal analysis of MOF-535, MOF-545-Fe, MOF-565 Single crystals of MOF-535 and MOF-545-Fe were analyzed using synchrotron X-ray diffraction, revealing a primitive cubic unit cell of 19.41 Å and a primitive hexagonal unit cell $a = 42.68$ Å and $c = 16.66$ Å, respectively. Data for MOF-565 was collected on a Bruker Apex two diffractometer; MOF-565 crystallizes in the space group Im-3m with a unit cell size of 38.4 Å. Each of the MOF structures was resolved using direct methods as implemented in Shelxs-97.[14]

Structure resolution of MOF-525 from powder X-ray diffraction (PXRD). Powder X-ray data were collected using a Bruker D8-Discover θ-θ diffractometer in reflectance Bragg-Brentano geometry employing Ni filtered Cu Kα line focused radiation at 1600 W (40 kV, 40 mA) power and equipped with a Vantec Line detector. Radiation was focused using parallel focusing Gobel mirrors. The system was also outfitted with an anti-scattering shield that prevents incident diffuse radiation from hitting the detector, preventing the normally large background at $2\theta < 3$. Samples were mounted on zero background sample holders by dropping powders from a wide-blade spatula and then leveling the sample with a razor blade. To determine the structure of MOF-525, crystal structure modeling was carried out, followed by Rietveld refinement.

Scanning electron microscopy and optical microscopy of MOF-525, MOF-535, and MOF-545 Samples were analyzed using a JOEL JSM-6700 Scanning Electron Microscope using the SEI detector with accelerating voltage of 5 kV. First, samples of synthesized MOF-525 were measured by dispersing the material onto a sticky carbon surface attached to a flat aluminum sample holder. The samples were then gold coated using a Hummer 6.2 Sputter at ambient temperature and a pressure of 70 mTorr in an argon atmosphere for 30 s while maintaining a current of 15 mA. The crystals of MOF-525 were shown to be cubic in morphology with sizes from 0.5-1.0 μm

Optical microscopy of MOF-535 and MOF-545 was carried out using a Leica optical microscope. As synthesized samples of MOF-535 and MOF-545 were dispersed onto a glass plate for imaging. MOF-535 crystals were shown to be cubic in shape with dimensions 0.1 × 0.1 × 0.1 mm. MOF-545 crystal were shown to have a needle morphology with dimensions 0.5 × 0.025 × 0.025 mm.

Transmission electron microscopy (TEM)

A JEM-2010F field emission TEM equipped with a CEOS post-specimen spherical aberration corrector (C_s corrector) was operated at 120 kV for high-resolution transmission electron microscopy (HRTEM) imaging.

Argon and nitrogen isotherms of MOF-525, MOF-525-Fe, MOF-525-Cu, MOF-545, MOF-545-Fe, and MOF-545-Cu.

Low-pressure gas adsorption isotherms were measured volumetrically. Ar isotherms of MOF-525, MOF-535, and MOF-545 were measured using an Autosorb-1 analyzer (Quantachrome Instruments). N_2 isotherms of MOF-525-Cu, MOF-525-Fe, MOF-545-Cu, and MOF-545-Fe were measured using a NOVA surface area analyzer (Quantachrome Instruments). A liquid nitrogen sample bath (77 K) was used for N_2 measurements and an Argon sample bath (87 K) was used for Ar isotherms. The N_2 and Ar gas used was UHP grade. For measurement of the surface areas, the BET method was applied using the adsorption branches of the N_2 (Ar) isotherms assuming an N_2 (Ar) cross-sectional area of 16.2 (14.2) $Å^2$/molecule.

UV-Vis spectroscopy of digested MOF-525, MOF-525-Fe, MOF-525-Cu, MOF-545, MOF-545-Fe, and MOF-545-Cu.

Ultraviolet-visible (UV-Vis) spectrophotometry measurements were performed on a Shimadzu UV1800 using 1 cm Hellma quartz optical cells.

Results and discussion.

Synthesis and structure of MOF-525, MOF-535, MOF-545, and MOF-565. Initial reactions between H_4-TCPP and $ZrCl_4$ yielded a multiphase microcrystalline powder (**Figure 1A**). The powder pattern from the microcrystalline powder had multiple peaks in the low angle range, indicative of a large unit cell, a common feature of MOFs (**Figure**

2). Therefore extensive efforts were dedicated to the synthesis of a pure phase of MOF from H_4-TCPP and a zirconium source. MOF-525 was formed by the reaction of zirconyl chloride octahydrate (12.5 mg, 0.037 mmol) and tetrakis(4-carboxyphenyl)porphyrin (2.5 mg, 0.037 mmol) in a solution of N,N,dimethylformamide (10 mL) and acetic acid (2.5 mL). After sonication this solution was placed in a 20 mL scintillation vial and heated at 65 °C for three days to yield a microcrystalline powder of MOF-525. The microcrystalline powder was activated by washing with DMF and acetone, followed by evacuation at 120 °C for 48 hrs, to yield MOF-525 ($Zr_6(OH)_4O_4$(TCPP-H_2)). SEM was used to confirmed the formation of a homogenous phase, which showed that a single phase had now been isolated from the initial mixture observed to have cubeoctahedron morphology (**Figure 1B**).

The microcrystalline size of MOF-525 meant it was not suitable for single crystal analysis. Therefore powder diffraction and the RCSR were used to resolve the structure of MOF-525. Initial structural matches were considered with 12,4- connected components from the RCSR, based on the connectivity of the metal oxide unit and the organic link. In the RCSR database, only three topologies combine 12,4-connected components **ith**, **shp**, and **ftw** (**Figure 3**). The **ith** and **shp** topology were excluded based on the geometry of the topological components. The **ith** topologies incorporates tetrahedral units that cannot be accessed by the porphyrin unit (**Figure 3A**). The **shp** topology was excluded because the geometry of the twelve coordinate unit is not a cuboctahedron, the cluster shape that is predominant in other zirconium based MOFs (**Figure 3B**).[1] Therefore, a structure with the **ftw** topology was generated, replacing the square units with TCPP-H_2 and cuboctahedron units with the zirconium metal oxide units,

$Zr_6O_4(OH)_4$, (**Figure 4**). The structure was constructed in the space group *Pm* $\bar{3}$ *m* (No. 221) with an optimized unit cell parameter of 19.39 Å (**Figure 4D**). The calculated PXRD pattern from the calculated structure was shown to be coincident with the experimental PXRD pattern for MOF-525 (**Figure 5A**). To confirm the calculated structure, a Pawley refinement was first carried out; this agreed with the calculated unit cell (R_{wp} = 8.34) (**Figure 6**). Secondly, a Rietveld refinement was performed on the activated sample to confirm the structure and the atom positions within the MOF-525 structure (**Figure 7**). The final refined unit cell parameters for MOF-525 are a = 19.393(3) Å, R_p = 8.98 wR_p = 12.28 (**Table 1-2**). The Pawley and Rietveld refinements support the structural assignment of MOF-525 in the **ftw** topology. MOF-525 has a pore diameter of 19 Å. Each unit cell is constructed from eight corner sharing $Zr_6O_4(OH)_4$ units and six face sharing porphyrin units, and each porphyrin is bridging four $Zr_6O_4(OH)_4$ units.

The structure of MOF-525 was further confirmed by the synthesis of MOF-535, which also possesses the **ftw** topology. MOF-535 was synthesized by reaction of zirconium tetrachloride (5.6 mg, 0.024 mmol) and 4,4′-((1*E*,1′*E*)-(2,5-bis((4-carboxyphenyl)ethynyl)-1,4-phenylene)bis(ethene-2,1-diyl))dibenzoic acid) (H_4-XF, 16 mg, 0.024 mmol) in DMF (10 mL) and acetic acid (2 mL). The reaction was initially heated at 60 °C for 4 hrs to dissolve residual components, followed by heating at 120 °C for two days. Activation was achieved in an analogous manner to that for MOF-525.

Single crystals of the as-synthesized MOF-535 were analyzed by synchrotron X-ray diffraction. MOF-535 has a primitive cubic unit cell where a = 19.41 Å, which is analogous to that of MOF-525. In MOF-535 the zirconium and oxygen atoms corresponding to the secondary-building units (SBUs) were located in the space group $Pm\bar{3}m$, the space group of the **ftw** topology (**Figure 9**) (**Table 3-4**). The SBUs are located at the vertices of the unit cell. Subsequent least-squares refinements were performed and the obtained difference Fourier maps showed areas of high electron density in the center and in the faces of the cell, attributed to solvent molecules and to the atoms of the ligand, respectively. However the exact positions of the atoms of the cruciform ligand could not be precisely located from this map. It should be noted that the point symmetry of the cruciform ligand is incompatible with its location in the faces of a cell in the $Pm\bar{3}m$ space group. Therefore, we performed refinements using a lower symmetry space group with the hope of locating the atoms of the linker in a compatible space group. These attempts were unsuccessful and resulted in residual values resembling those found for the higher symmetry space group. Therefore we believe that the relative orientation of the ligand with respect to the SBUs is randomly distributed along the crystal (nonperiodic) while the overall connectivity of the network is maintained (as proved by the unequivocal position of the $Zr_6O_4(OH)_4$ and the twelve carboxylic groups). Because a disorder model could not be described, we assigned the peaks with higher density in those areas to C atoms (**Figure 9**). The final refinements were performed after performing the squeeze[15] routine to eliminate the disordered solvent molecules found in the cavities. Modelling was used to generate a structural representation of MOF-535, with cubeoctahedron clusters and XF links (**Figure 10**). The structure of MOF-535 was shown to be analogous to that of MOF-525 by comparison of the PXRD with the same space group and nearly identical unit cell sizes (**Figure 5**).

Initial SEM of reactions between H_4-TCPP-H_2 revealed a multi-phase product of reaction; the final product isolated was MOF-525. Secondly, another MOF, MOF-545 was isolated as single crystals. (**Figure 1C**). MOF-545 was synthesized by reaction of zirconyl chloride octahydrate (37.5 mg, 0.111 mmol) and tetrakis(4-carboxyphenyl)porphyrin (6.5 mg, 0.037 mmol) (6.5 mg, 0.037 mmol) in DMF (10 mL) and formic acid (7 mL). The solution was placed in two 20 mL scintillation vials and heated at 130 °C for three days. To activate the crystalline framework the crystals were collected by vacuum filtration and washed with DMF (5 × 10 mL) and acetone (5 × 30 mL). The acetone was removed by heating at 120 °C under vacuum (30 mTorr) for 48 hrs.

The initial X-ray diffraction study, carried out using synchrotron radiation, revealed a hexagonal unit cell with cell parameters a = 80.84 Å and c = 17.04 Å. Further resolution of the data with these unit cell parameters was not possible from single crystal diffraction, due to twinning of the crystal. Many attempts were made to grow crystals that did not have this twinning, this was achieved by replacing H_4-TCPP-H_2 with H_4-TCPP-FeCl (**Figure 1D**). No twinning was observed with the MOF-545-FeCl crystals and the structure could be solved from single crystal diffraction data. MOF-545-Fe crystallizes in the hexagonal space group *P*6/*mmm* (No. 191) with unit cell parameters *a* = 42.545 Å and *c* = 16.96 Å (**Table 5-6**). The link position within the unit cell was fully elucidated using a least squares refinement (**Figure 10**). The final refinements were performed after the squeeze[14] routine was used to eliminate the disordered solvent molecules found in the cavities. The SBU of MOF-545 contains eight terminating water ligands, which have replaced four of the twelve carboxylate groups found in the SBU of MOF-525 (**Figure**

10). To maintain the charge balance of the metal cluster, eight μ_3-oxo atoms complete the SBU with the formula $Zr_6O_8(-CO_2)_8(H_2O)_8$. The geometry of the simplified SBU is now a cube, which combines with the square tetratopic link to give the **csq** topology of MOF-545. The structure of MOF-545-Fe contains hexagonal and triangular 1-D channels that have a diameter of 36 Å and 8 Å, respectively. To confirm that the twinned structure of MOF-545 was analogous to that of MOF-545-Fe, PXRD was carried out (**Figure 2B**).

A third phase, MOF-565, was crystallized in the presence of MOF-545 when reactions were carried out at a lower concentration of reagents (**Figure 1E**). MOF-565 was synthesized by reaction of Zirconyl chloride octahydrate (18.75 mg, 0.055 mmol) and tetrakis(4-carboxyphenyl)porphyrin (3.25 mg, 0.0185 mmol) (6.5 mg, 0.037 mmol) in DMF (10 mL) and formic acid (7 mL).

Although MOF-565 was not isolated as a pure phase it was possible to isolate one single crystal for X-ray diffraction studies. Single crystal studies revealed a third porphyrin containing topology, **she**, which incorporates a hexagonal metal oxide unit and tetracoordinate porphyrin units (**Figure 11**). MOF-565 crystallized in the cubic space group Im-3m (229) with a unit cell parameter a =38.4 Å.

The porosity of each guest free pure phase was measured by argon adsorption isotherms at 87 K (**Figure 12**) The argon isotherms for MOF-525, MOF-535, and MOF-545 clearly showed a reversible argon adsorption indicative of permanent porosity (**Figure 12**). Surface area analysis of the isotherms of MOF-525, 535, and 545 by the BET method gave surface areas of 2620, 1120, and 2260 m^2/g, respectively. MOF-525 has the highest surface area reported for a zirconium based MOF. The step position observed in the argon isotherm of MOF-545 supports the mesoporous size (36 Å) of the large hexagonal pore (**Figure 12**).

The structure of MOF-525 and MOF-545 was further revealed by transmission electron microscopy (TEM), which provided direct insight into the pore diameters of MOF-525 and MOF-545 (**Figure 13**). Because of the crystal size of MOF-545 the single crystals of MOF-545 were first crushed. TEM of MOF-525 revealed the pores of MOF-525 visible as lighter areas in the TEM image, which confirms the 2 nm pore size. TEM of MOF-545 revealed two pores, one small and one large, 8 Å and 36 Å, respectively.

The chemical stability of the porphyrin containing MOFs, MOF-525 and 545, was evaluated by exposing the activated structures to methanol, water, and acidic conditions [water:acetic acid = 50:50 (v/v)] for 12 h (**Figure 13-16**). Each stability test was carried out under analogous conditions, 100 mg of MOF was suspended in 10 mL of the appropriate solvent and allowed to stand at room temperature for 24 hrs. No leaching of porphyrin into solution was seen, indicative that the MOF was not being digested. After each test the sample was filtered and activated by solvent exchange under identical conditions reported for the activation of the parent MOF. Following activation of these MOFs, crystallinity (**Figure 15-16**) and porosity (**Figure 17-18**) of the MOFs was maintained. In the presence of water:acetic acid = 50:50 (v/v), the color MOF-525 and 545 turned green in solution as a result of ground-state protonation of the porphyrins.[16] This protonation of the porphyrin clearly shows that the porphyrin sites are accessible.

The **csq** and **ftw** topologies both contain porphyrin units, and have high porosity, chemical stability, large pores, and accessible porphyrin sites; therefore, they are potentially suitable for catalysis and gas adsorption applications, however, before these applications can be assessed the porphyrin must be metalated. Two methods were used to metalate the porphyrin in MOF-525 and MOF-545, pre- and post-metalation. Primarily, pre-metalation has been achieved using H_4-TCPP-Cu and H_4-TCPP-FeCl under nearly identical conditions to those of metalation of MOF-525 and MOF-545 to form MOF-525-Cu [$Zr_6O_4(OH)_4$(TCPP-Cu)$_3$], MOF-545-Fe [Zr_6O_8(TCPP-FeCl)$_2$(H_2O)$_8$], and MOF-545-Cu [Zr_6O_8(TCPP-Cu)$_2$(H_2O)$_8$].

Attempts to pre-metalate MOF-525 with iron were unsuccessful; a pure phase was not isolated Therefore, post-metalation of the open porphyrin sites of activated MOF-525 was favored in post-metalation methodology, which was successful in quantitatively introducing iron into the porphyrin of MOF-525. MOF-525 metalation was achieved by dissolving iron chloride (200 mg, 1.6 mmol) in DMF (40 mL) to which MOF-525 (100 mg) was added. The reaction was heated to 100 °C for 12 h. Following reaction, the excess metal salts were removed by washing with DMF under activation conditions analogous to those of MOF-525 yielding a solvent free framework.

Analysis of the PXRD patterns showed that the metalated analogs of MOF-525 and 545 have the same structure as their non-metalated analogs (**Figure 5**). Analysis of the nitrogen isotherms of each MOF revealed BET surface areas comparable to the non-metalated analogs (**Figure 19**). To confirm that each MOF was quantitatively metalated, the samples were digested in 2 M NaOH, and a UV-vis spectroscopy study was performed; in no case was unmetalated porphyrin observed in the digested material. Each MOF was shown to contain only one porphyrin species, confirming the samples were quantitatively metalated (**Figure 20-22**).

Conclusions

In conclusion, after extensive synthetic efforts four new MOFs have been synthesized, exhibiting three new zirconium topologies, **ftw** (MOF-525 and MOF-535), **csq** MOF-545, and **she** (MOF-565) based on tetratopic organic units and highly stable zirconium oxide units. The structures of MOF-525, -535, and MOF-565 were resolved from single crystal analysis. MOF-525 was isolated as a microcrystalline powder, which made it unsuitable for single crystal analysis. However, the structure of MOF-525 was resolved by first applying the RCSR in generating potential structure matches. These structural models provided calculated PXRD data which, were compared with the experimental structures PXRD data, confirming an **ftw**. Three metal oxide shapes are reported, cubeoctahedron, cubes, and hexagons in the metal oxide units of MOF-525, MOF-545, and MOF-565, respectively. The cubic and hexagonal metal oxide units reported are novel in zirconium MOF chemistry, and are a result of capping of points of extension in the cubeoctahedron by water molecules.

Porphyrin units are incorporated into each of the three topologies, making them suitable for metalation. Two routes were used to metalate phase pure MOF-525 and MOF-545, pre- and post-metalation, with metalation by both routes resulting in quantitative metalation. The high chemical stabilities and surface areas of these metalated porphyrin MOFs expand the scope of chemistry of not just zirconium MOFs, but porphyrin based MOFs with potential applications in catalysis still to be investigated.

Figures

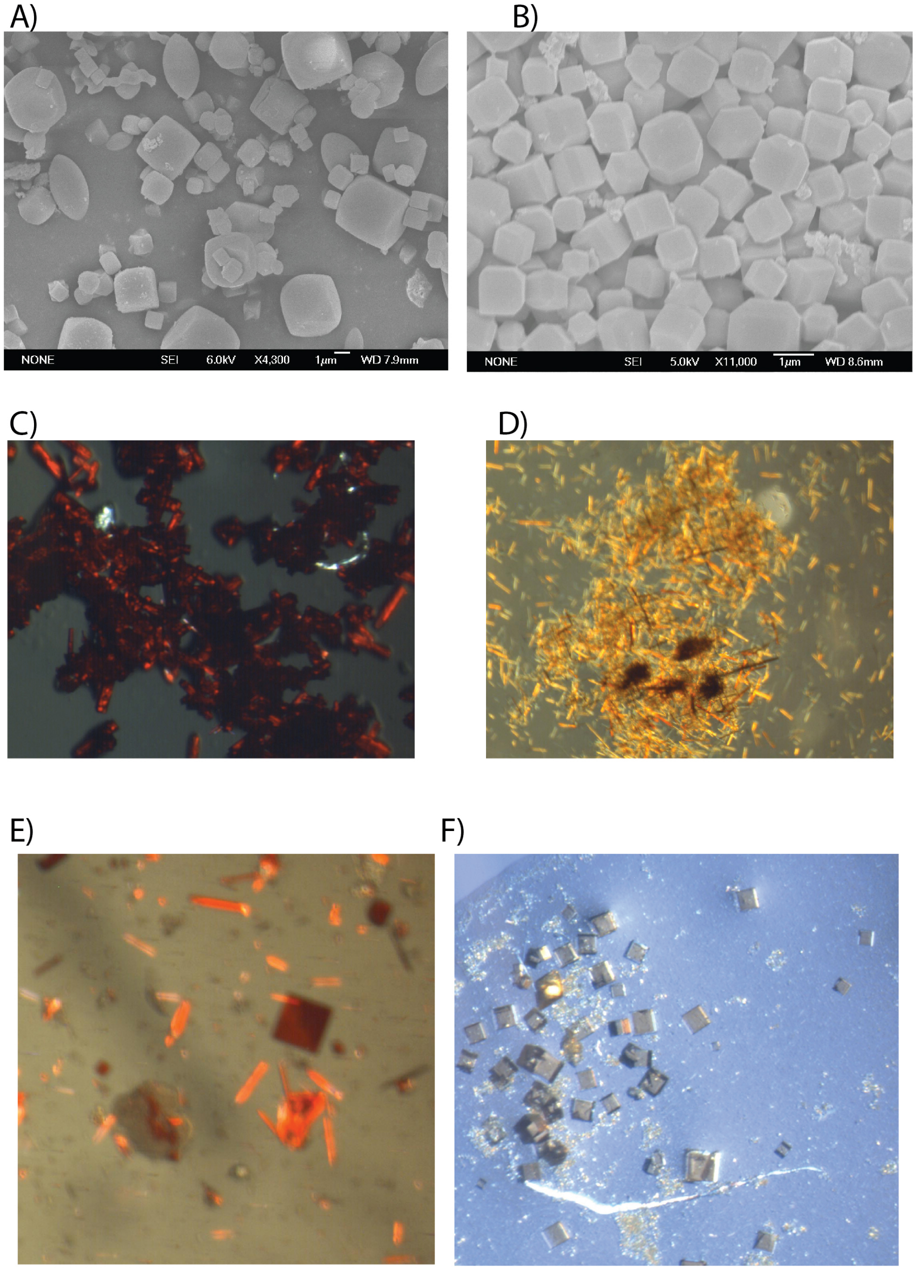

Figure 1) A-F) Optical microscopy and scanning electron microscopy of MOF-525, MOF-545, MOF-535, MOF-545-FeCl, and MOF-565 A) Mixture of MOF-525 and MOF-545. B) MOF-525. C) MOF-545 D) MOF-545-FeCl E) MOF-565. F) MOF-535

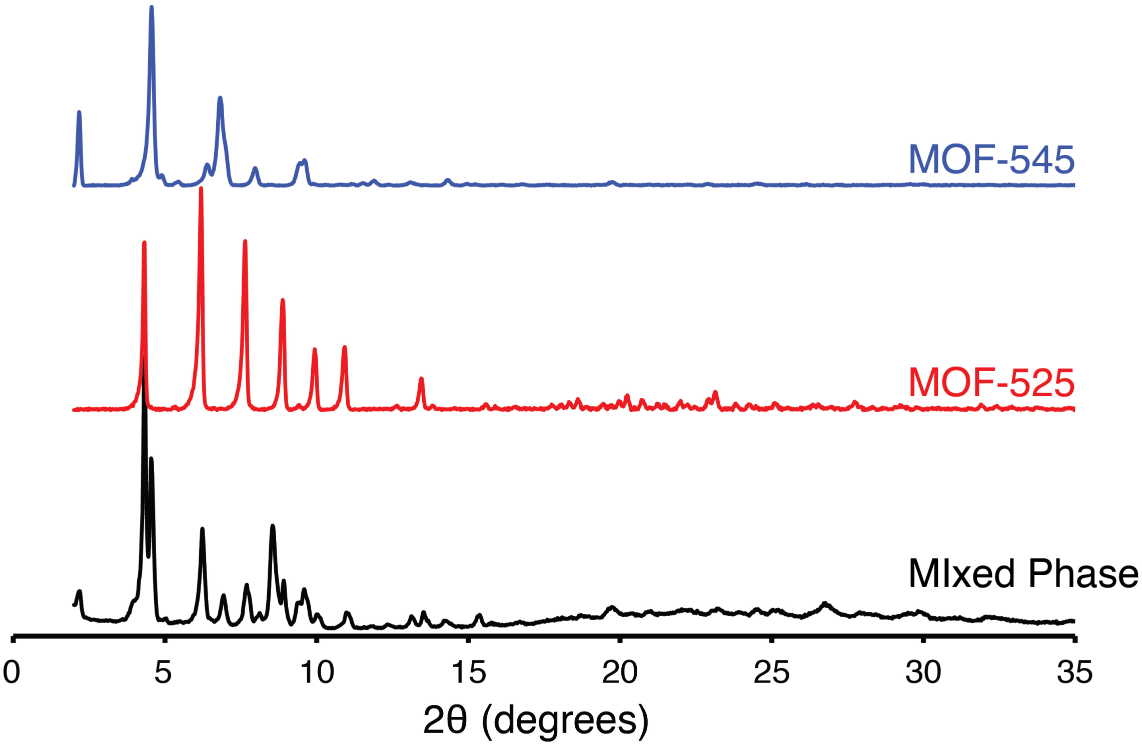

Figure 2) Powder X-Ray diffraction of MOF-525 and MOF-545. Mixture of MOF-545 and MOF-525 (black), MOF-525 (red), and MOF-545 (blue).

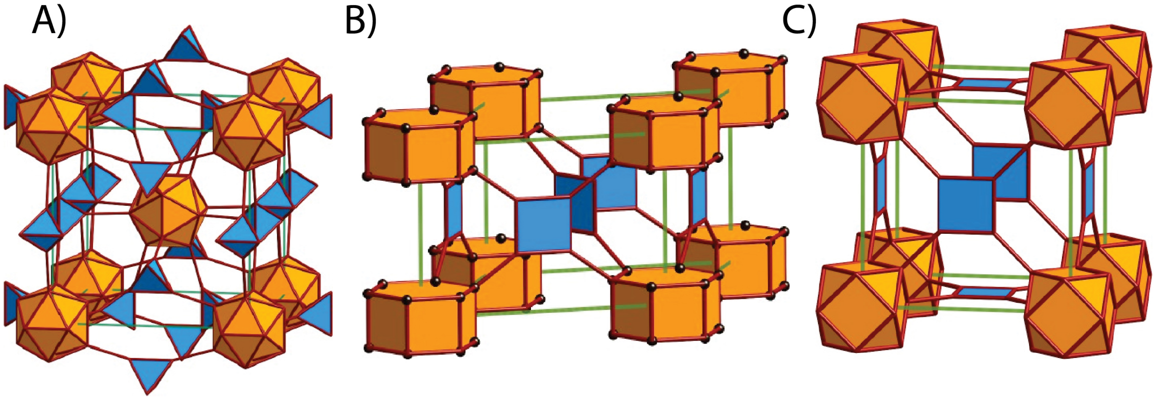

Figure 3) A-C) 12-4-connected nets from the reticular chemistry structural resource (RCSR) A) **ith** topology B) **shp** topology C) **ftw** topology.

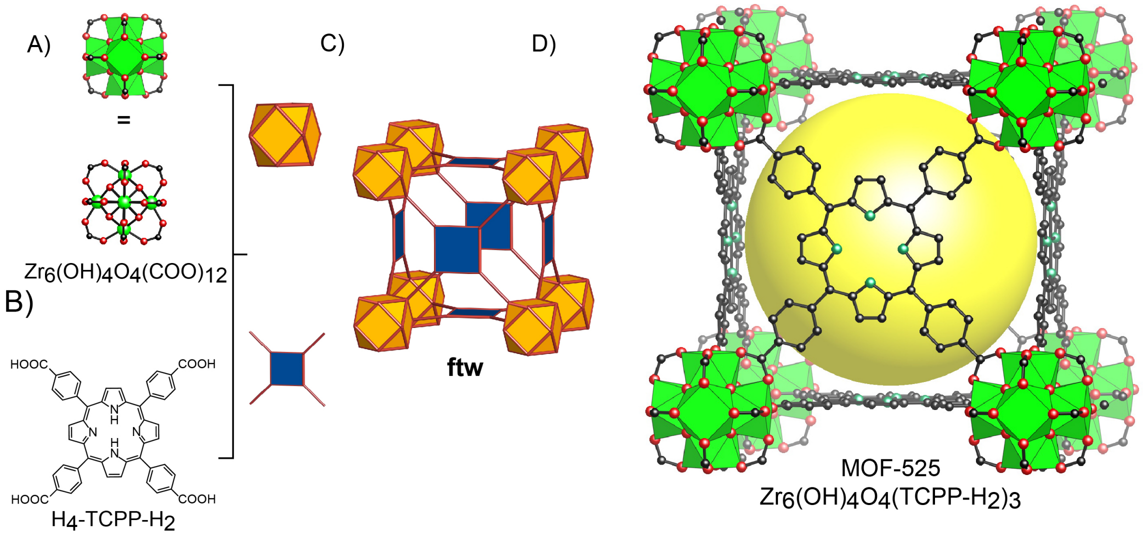

Figure 4) A-D) Structure and topology of MOF-525. A) A cube octahedral unit, $Zr_6(OH)_4O_4(-CO_2)_{12}$. (B) The organic links used in MOF-525 [H_4-TCPP-H_2 = tetracarboxyphenylporphyrin (C) The **ftw** topology. (D) Structure of MOF-525 Pores in the frameworks are illustrated by yellow spheres that contact the van der Waals radii of the atoms. Atom colors: zirconium, green polyhedra; carbon, black; nitrogen, dark green; oxygen, red. Hydrogen atoms are omitted for clarity.

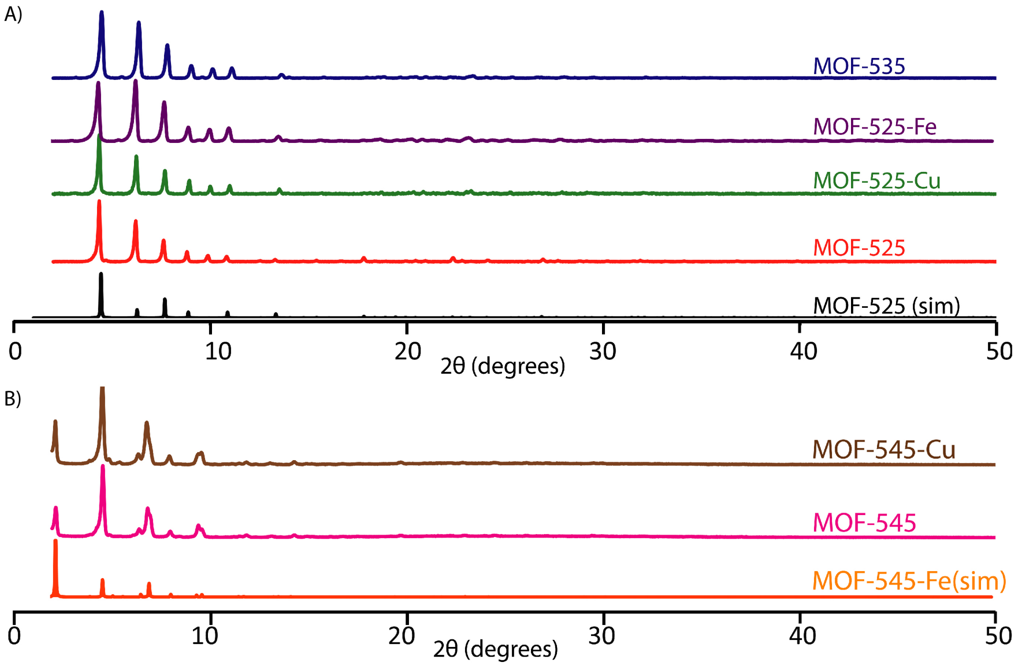

Figure 5) Powder X-ray Diffraction data for MOF-525, 535, and 545. (A) PXRD patterns of calculated **ftw** structure of MOF-525 (black), MOF-525 (red), MOF-525-Cu (green), MOF-525-Fe (purple), MOF-535 (blue). (B) PXRD of calculated **csq** structure of MOF-545-Fe, MOF-545 (pink), and MOF-545-Cu (brown).

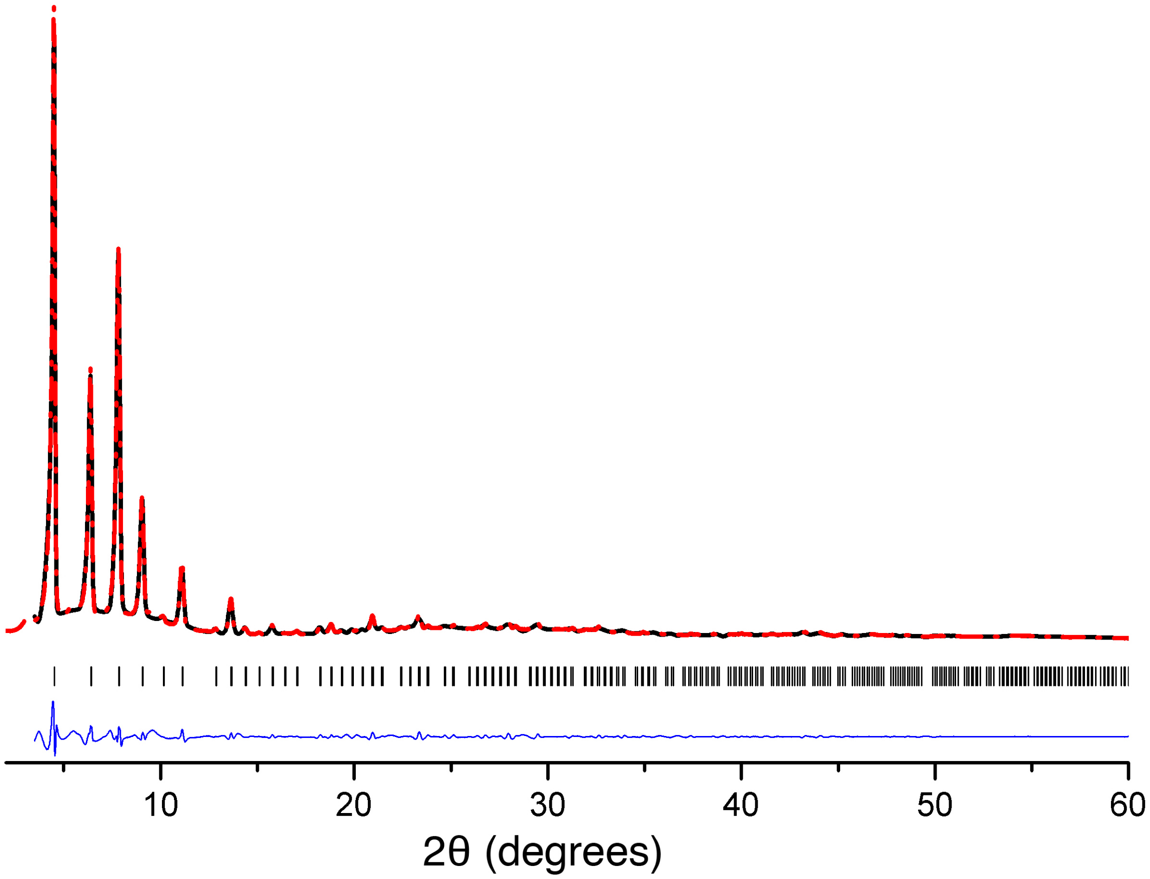

Figure 6) Pawley analysis of MOF-525. Red dashed, experimental pattern; black, calculated pattern; blue, difference pattern (exp-calc).

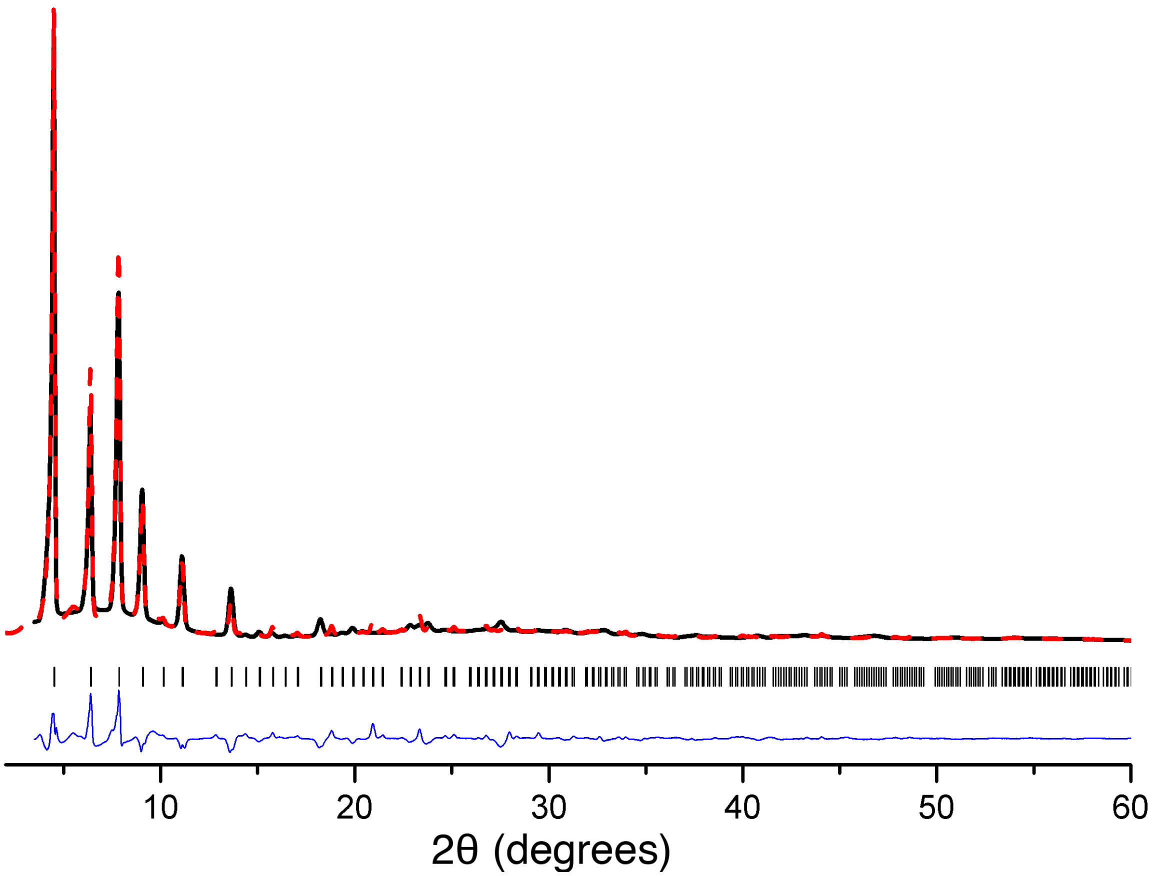

Figure 7) Rietveld analysis of MOF-525. Red dashed, experimental pattern; black, calculated pattern; blue, difference pattern (exp-calc).

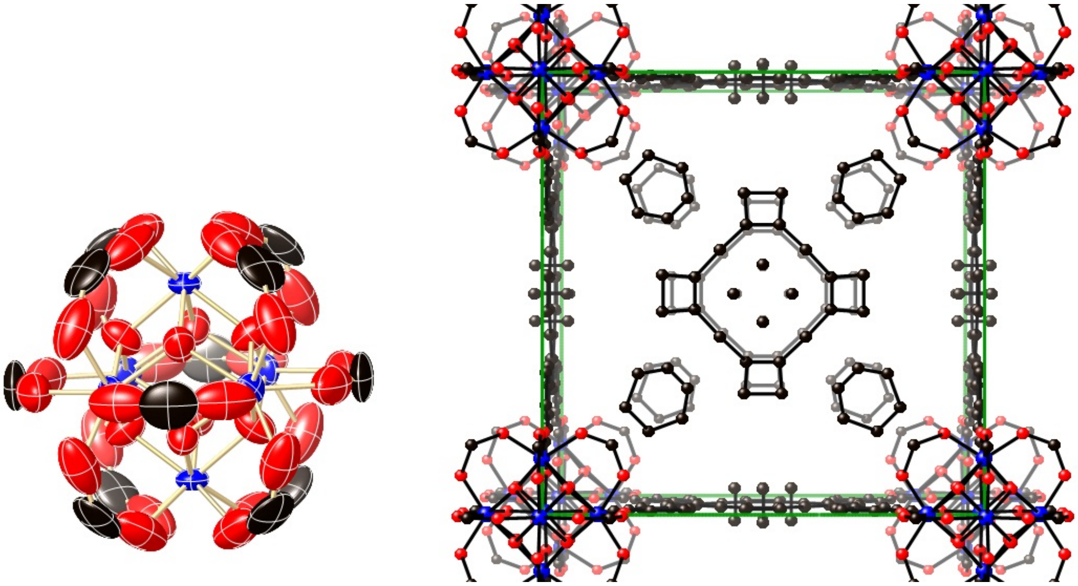

Figure 8) Left: ORTEP representation (30% probability) of the $Zr_6O_4(OH)_4(COO)_{12}$ cluster. Right: Ball and stick drawing of one unit cell. The SBUs are located at the corners of the cell. The disordered cruciform ligands connect the SBUs in the faces of the cell. Zirconium is blue, oxygen is red, and carbon is black.

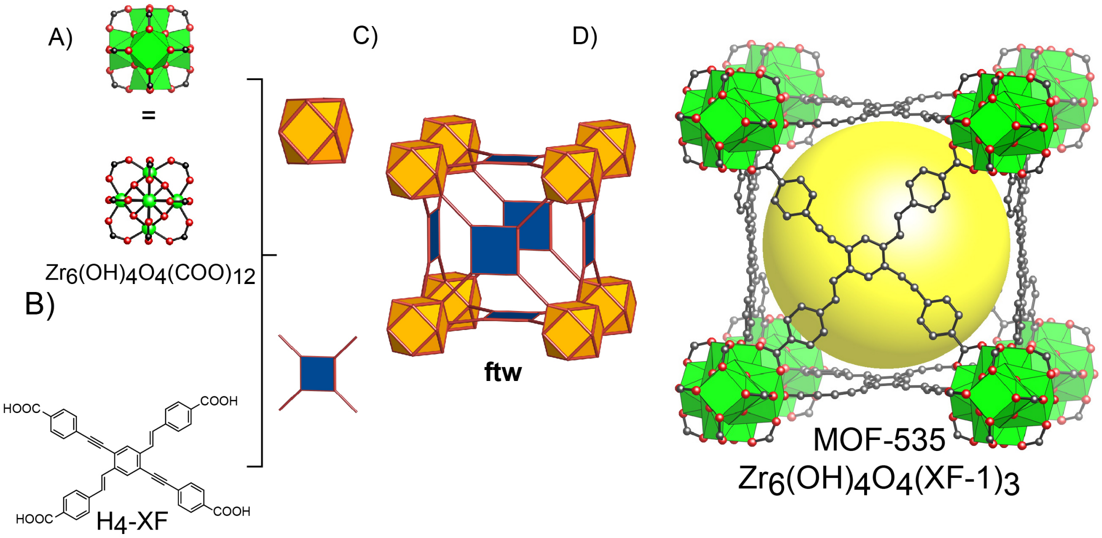

Figure 9) A-D) Structure and topology of MOF-535. A) A cube octahedral unit, $Zr_6(OH)_4O_4(-CO_2)_{12}$. (B) The organic links used in MOF-535 [H_4-XF = 4,4'-((1*E*,1'*E*)-(2,5-bis((4-carboxyphenyl)ethynyl)-1,4-phenylene)bis(ethene-2,1-diyl))dibenzoic acid)] (C) The **ftw** topology. (D) Structure of MOF-535 Pores in the frameworks are illustrated by yellow spheres that contact the van der Waals radii of the atoms. Atom colors: zirconium, green polyhedra; carbon, black; nitrogen, dark green; oxygen, red. Hydrogen atoms are omitted for clarity.

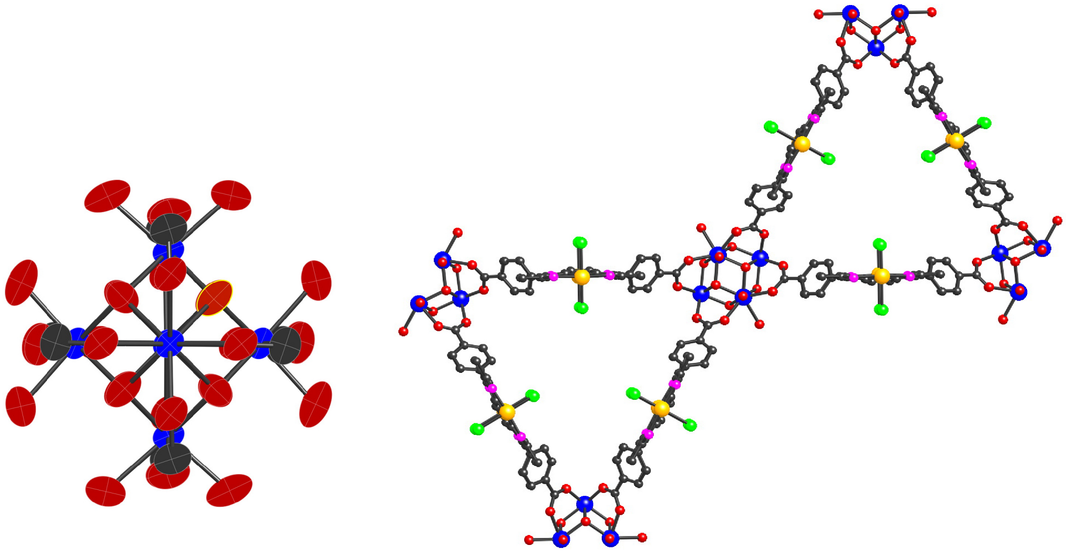

Figure 10) Left: ORTEP representation (50% probability) of the $Zr_6O_8(COO)_8(H_2O)_8$ cluster. Right: Ball and stick drawing of one unit cell. Zirconium is blue, oxygen is red, iron is yellow, nitrogen is pink, chlorine is green and carbon is black.

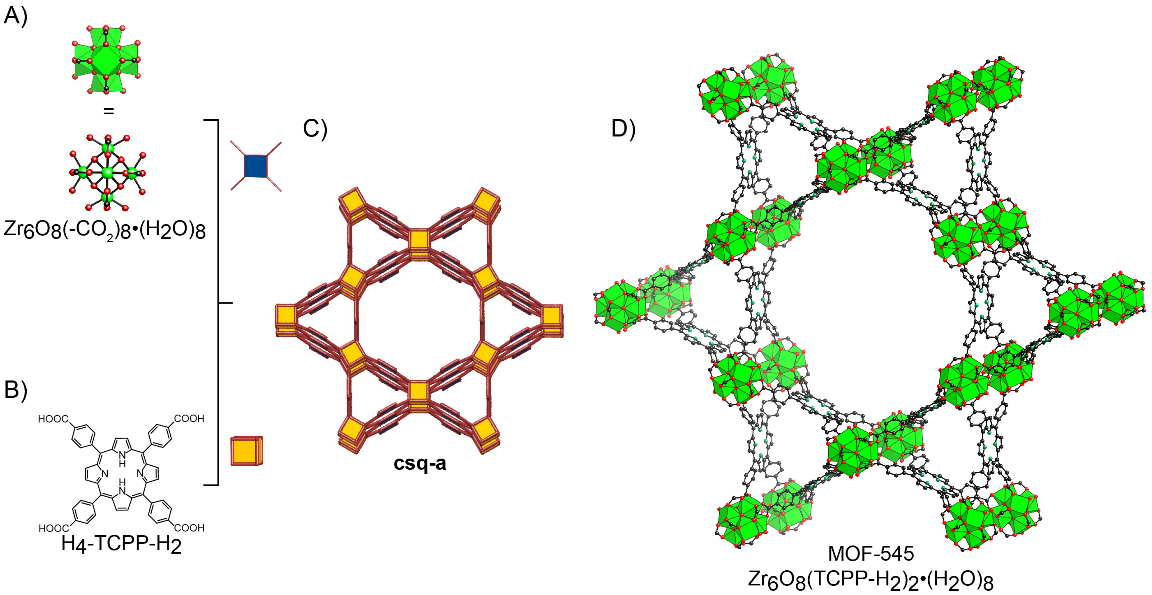

Figure 11) The topology and crystal structure of MOF 545. (A) A cube unit, $Zr_6O_8(-CO_2)_8(H_2O)_8$. (B) The organic links used in MOF-545 [H_4-TCPP-H_2 = tetracarboxyphenylporphyrin], (C) The **csq** topology. (D) Structure of MOF-545. Pores in the frameworks are illustrated by yellow spheres that contact the van der Waals radii of the atoms. Atom colors: zirconium, green polyhedra; carbon, black; nitrogen, dark green; oxygen, red. Hydrogen atoms are omitted for clarity.

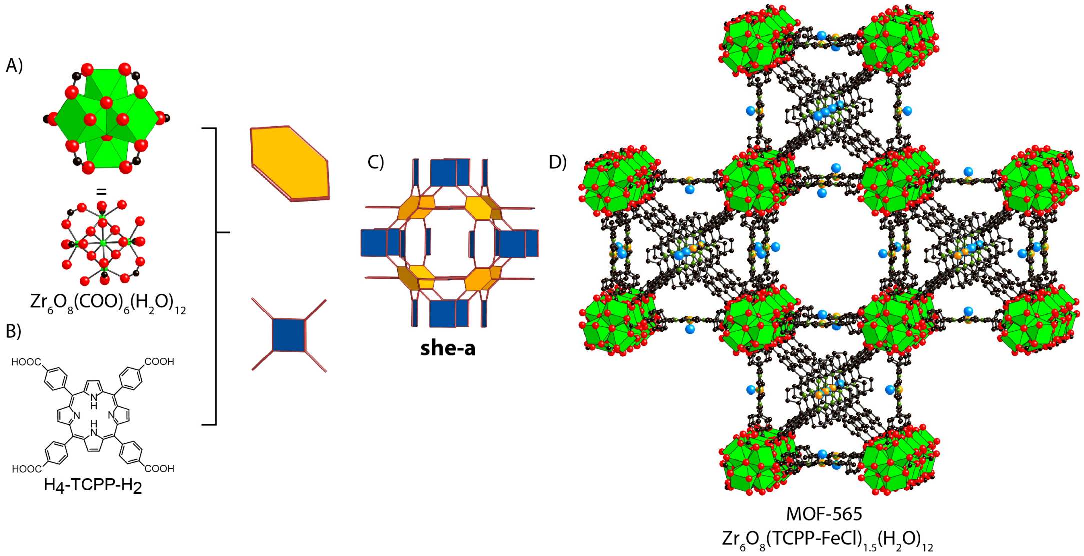

Figure 12) The topology and crystal structure of MOF-565. (A) A hexagonal unit, $Zr_6(O_8(\text{-}CO_2)_6(H_2O)_8(OH)_2$. (B) The organic links used in MOF-565 [H_4-TCPP-H_2 = tetracarboxyphenylporphyrin], (C) The **she** topology. (D) Structure of MOF- Pores in the frameworks are illustrated by yellow spheres that contact the van der Waals radii of the atoms. Atom colors: zirconium, green polyhedra; carbon, black; nitrogen, dark green; oxygen, red. Hydrogen atoms are omitted for clarity.

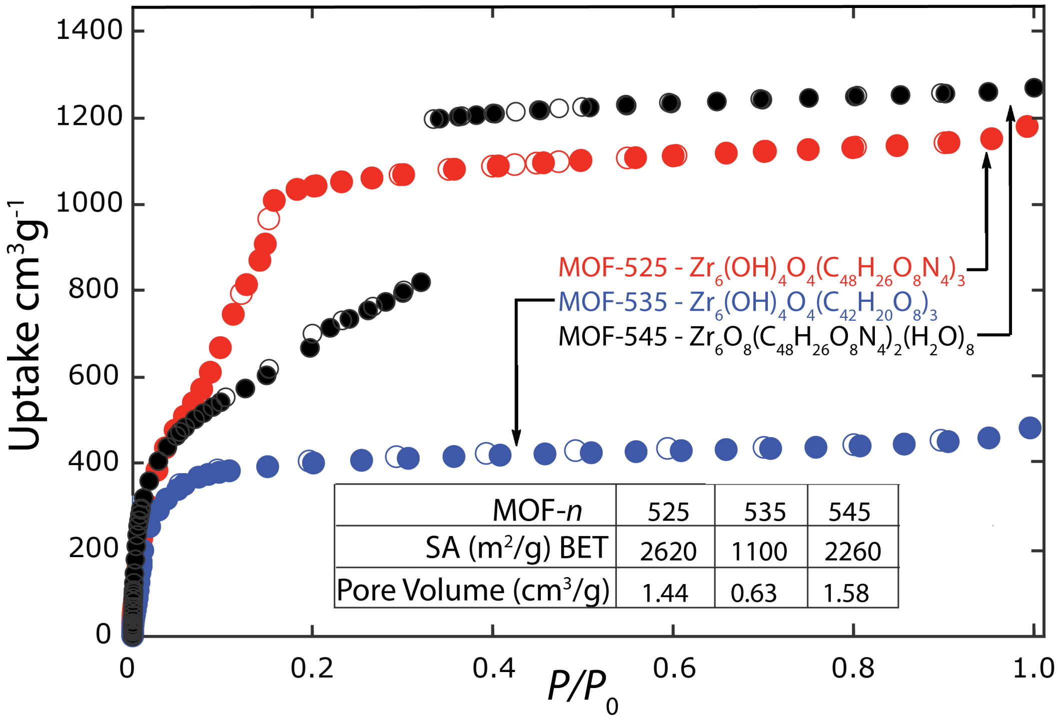

MOF-*n*	525	535	545
SA (m^2/g) BET	2620	1100	2260
Pore Volume (cm^3/g)	1.44	0.63	1.58

Figure 13) Argon gas adsorption isotherms for MOF-525 (red), MOF-535 (blue), and MOF-545 (black) at 87 K, with adsorption and desorption points represented by solid and open circles, respectively.

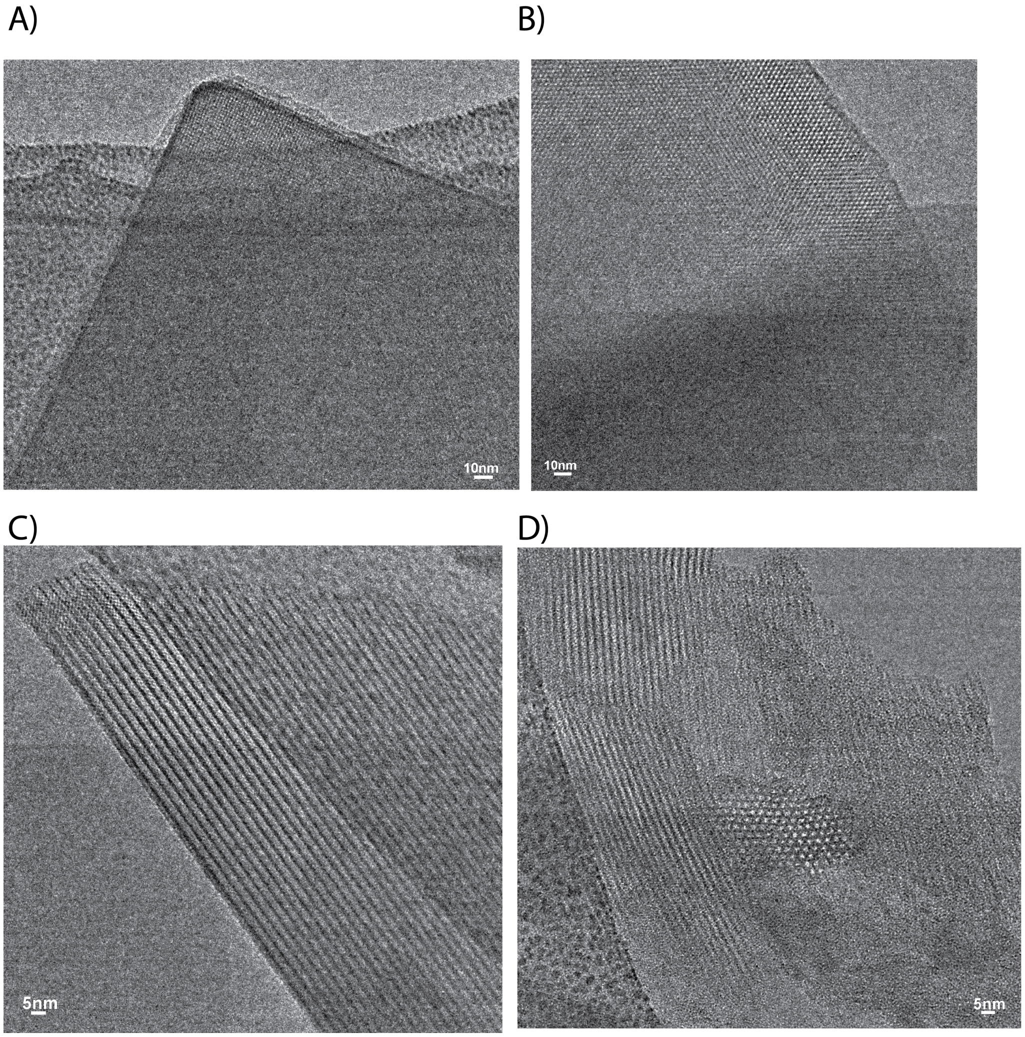

Figure 14) A-D) Transmission electron microcopy of MOF-525 and MOF-545. A-B) MOF-525, C-D) MOF-545.

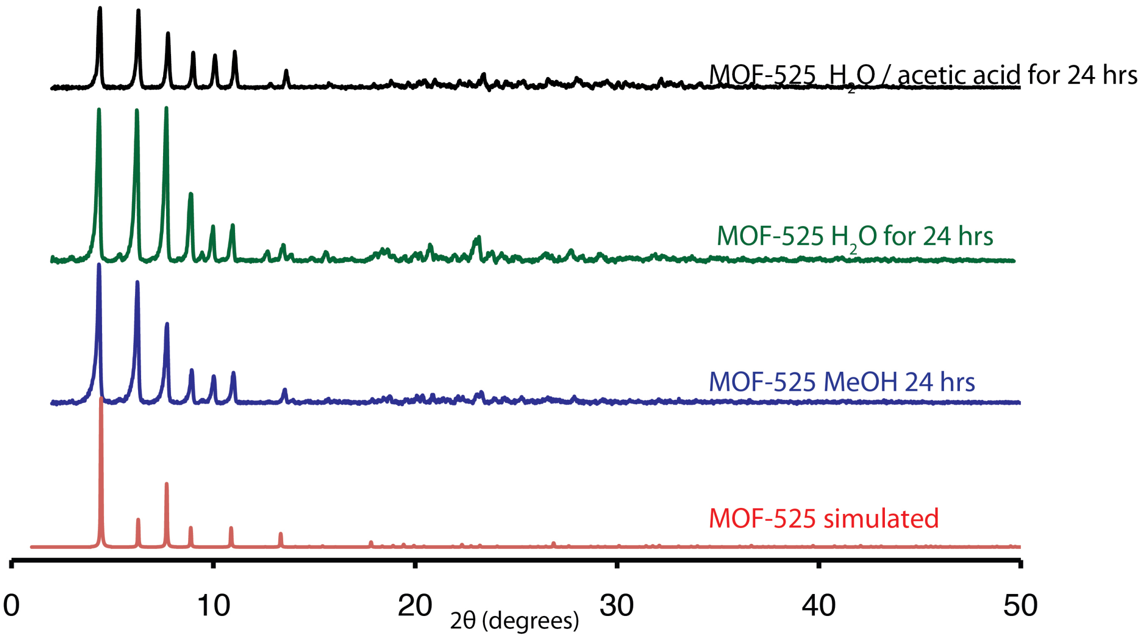

Figure 15) PXRD of samples of MOF-525 after suspension in organic and aqueous solvents. MOF-525 simulated (red), MOF-525 after suspension in to MeOH (blue), MOF-525 after exposure to H_2O, and MOF-525 after suspension in H_2O acetic acid (50/50, vol) (black).

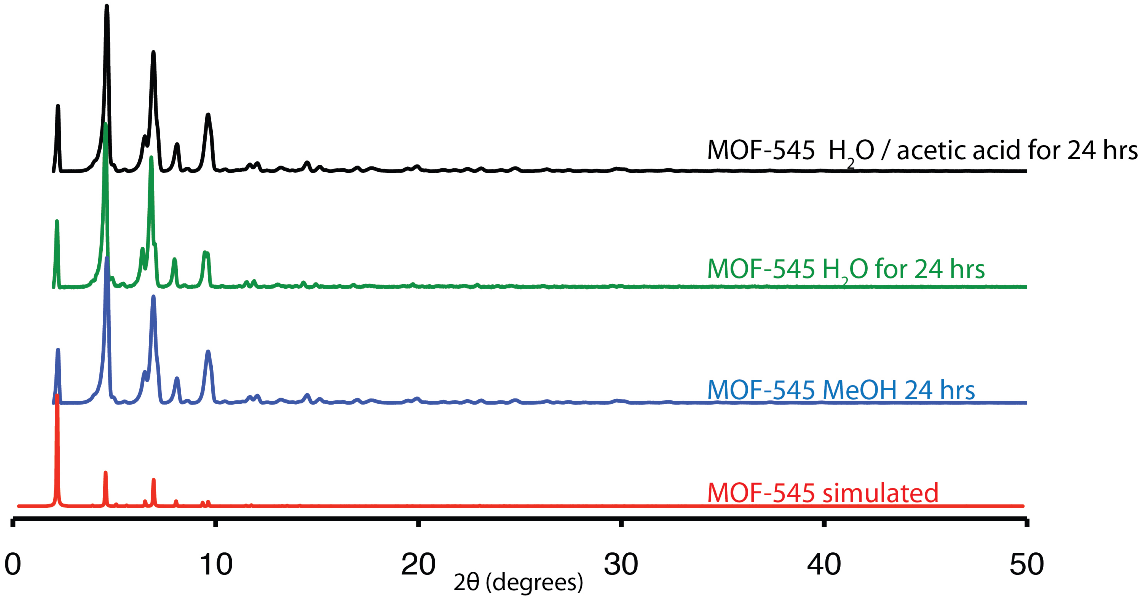

Figure 16) Powder X-ray diffraction of samples of MOF-545 after suspension in organic and aqueous solvents. MOF-545 simulated (red), MOF-545 after suspension in MeOH (blue), MOF-545 after suspension in H_2O, and MOF-545 after suspension in to H_2O acetic acid (50/50, vol) (black).

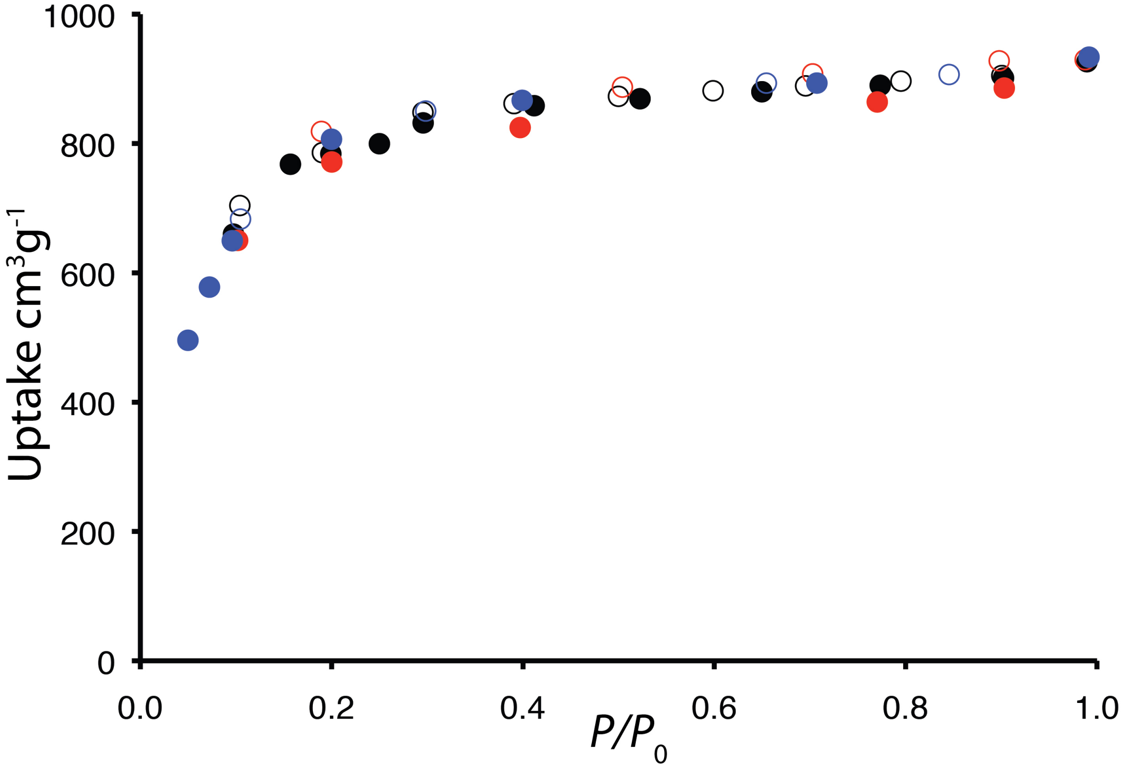

Figure 17) N_2 isotherms at 77 K of samples of MOF-525 after suspension in organic and aqueous solvents. MOF-525 simulated (red), MOF-525 after suspension in MeOH (blue), MOF-525 after exposure to H_2O, and MOF-525 after suspension in H_2O acetic acid (50/50, vol) (black).

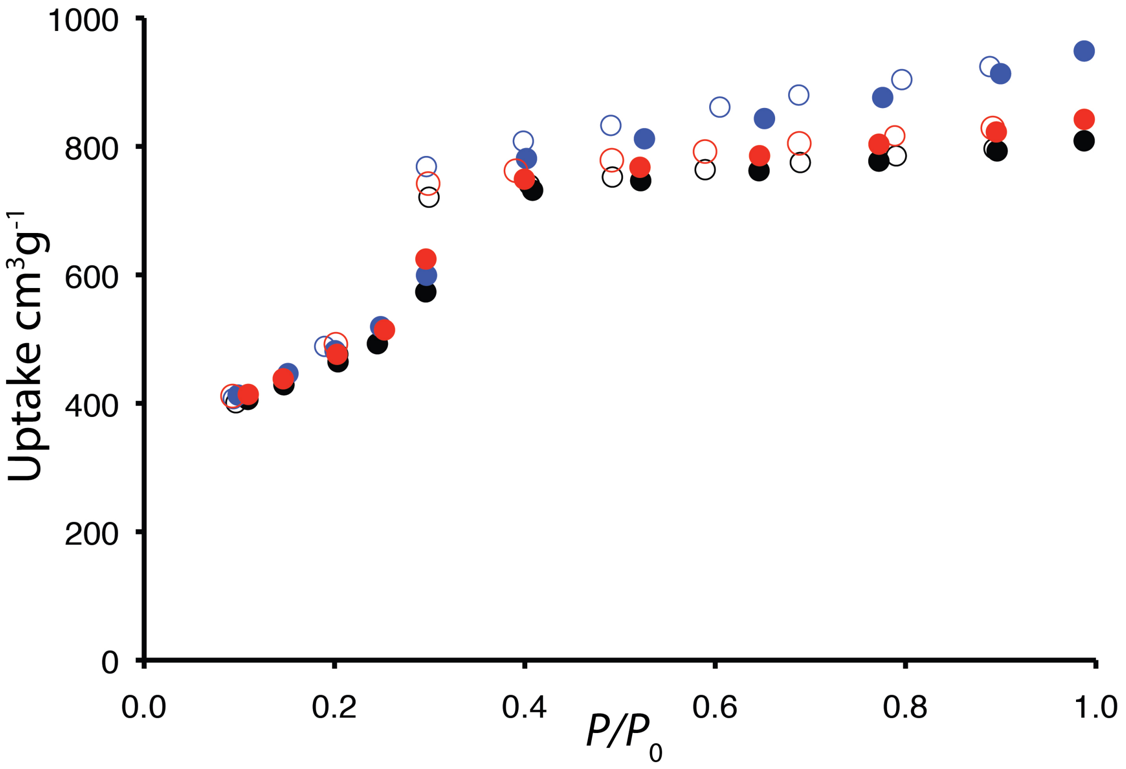

Figure 18) N_2 isotherms at 77 K of samples of MOF-545 after suspension in organic and aqueous solvents. MOF-545 simulated (red), MOF-545 after suspension in MeOH (blue), MOF-545 after exposure to H_2O, and MOF-545 after exposure to H_2O acetic acid (50/50, vol) (black).

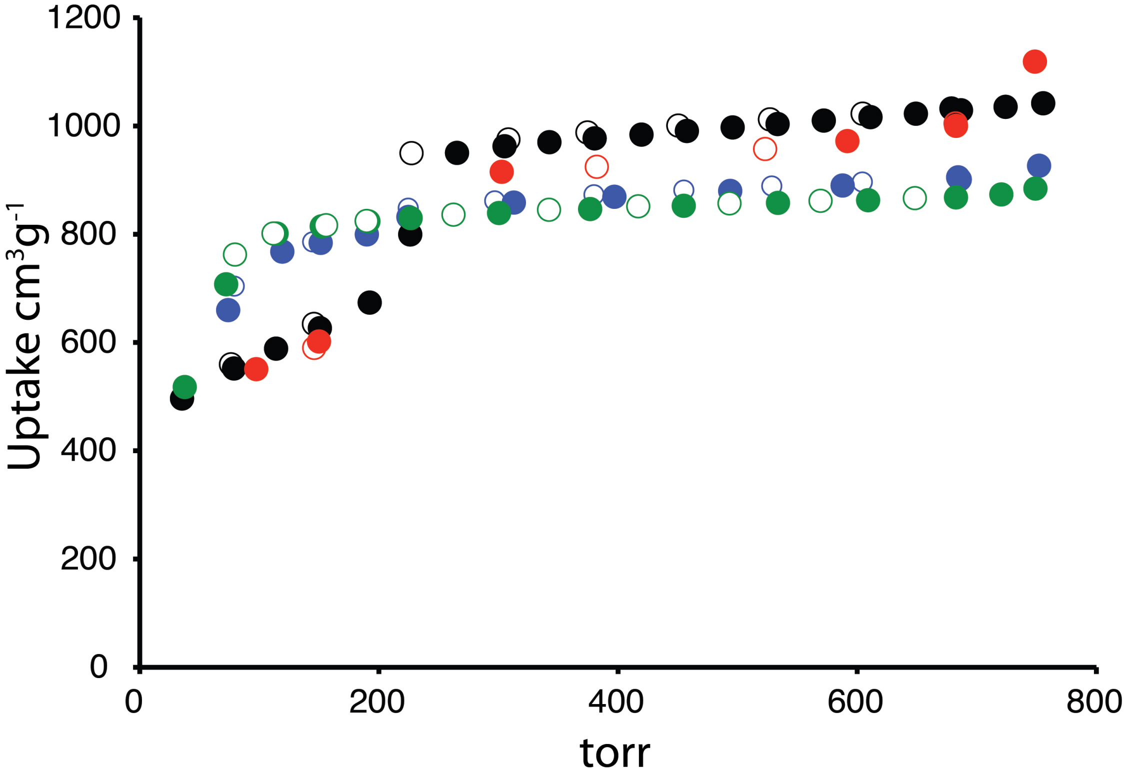

Figure 19) N_2 isotherms of MOF-525-Fe (green), MOF-525-Cu (blue), MOF-545-Fe (red), and MOF-545-Cu (black).

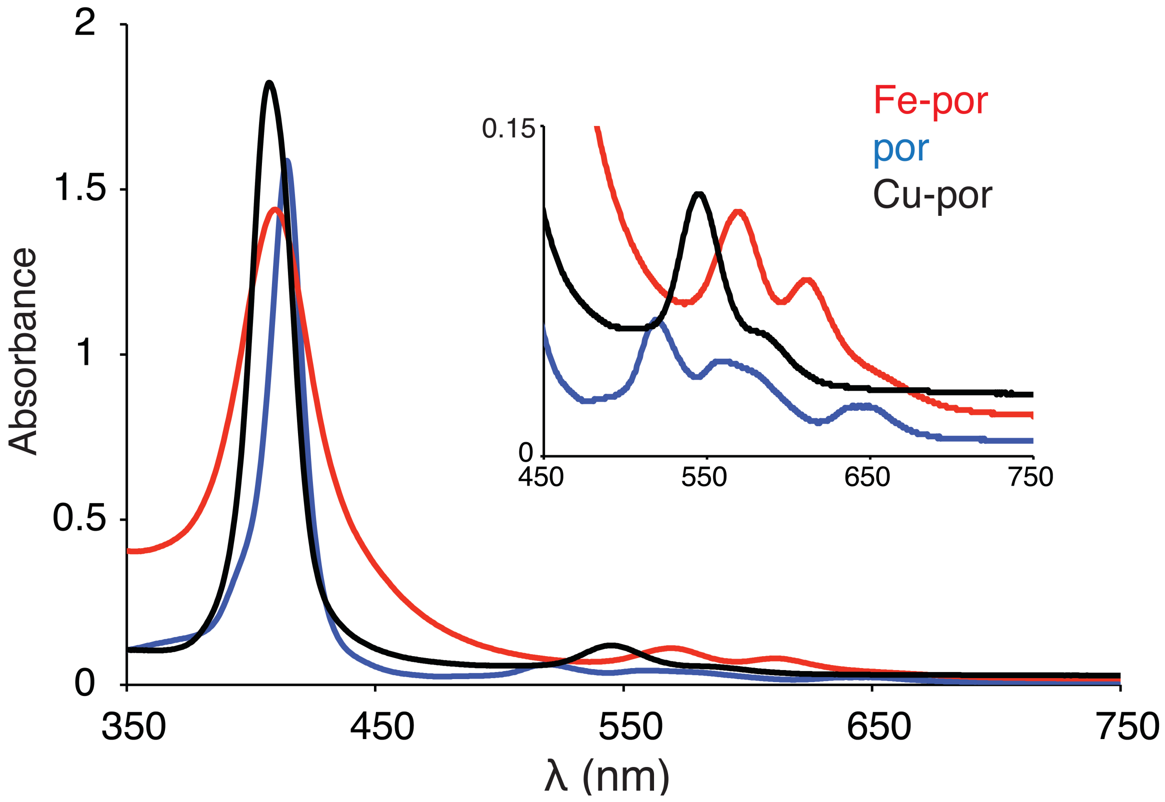

Figure 20) UV-Visible spectra of Fe-porphyrin (red), porphyrin (blue), and Cu-porphyrin (black).

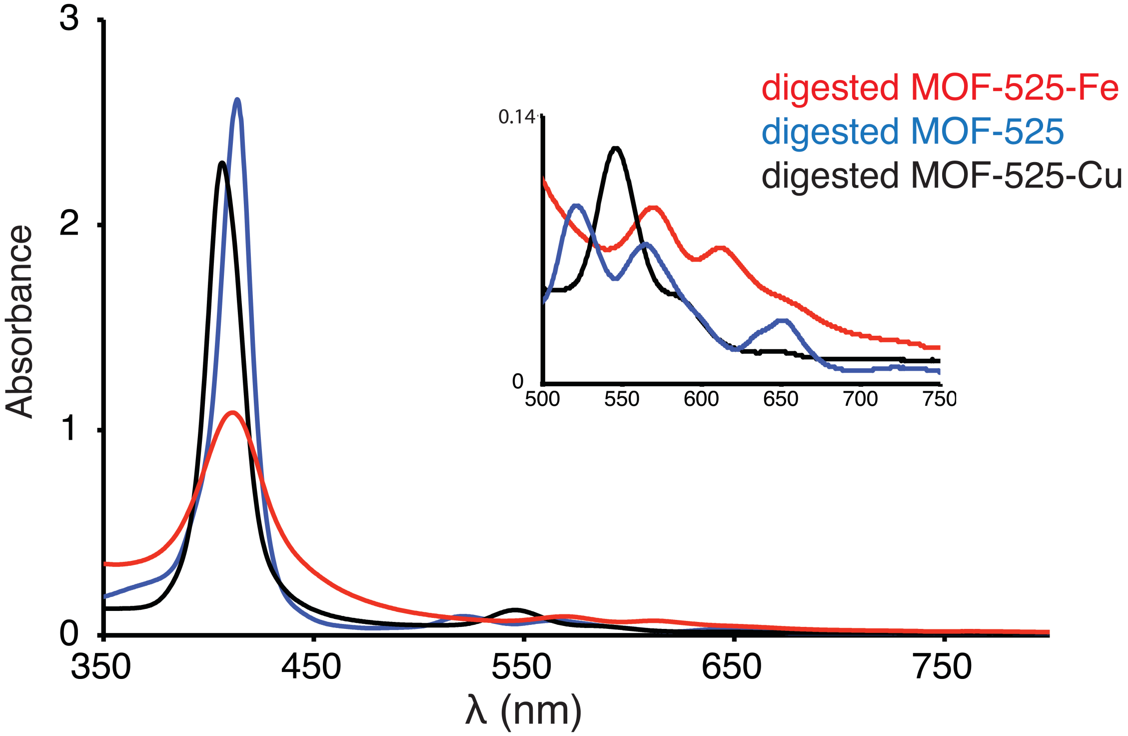

Figure 21) UV-Visible spectra of digested, MOF-525-Fe (red), MOF-525 (blue), and MOF-525-Cu (black).

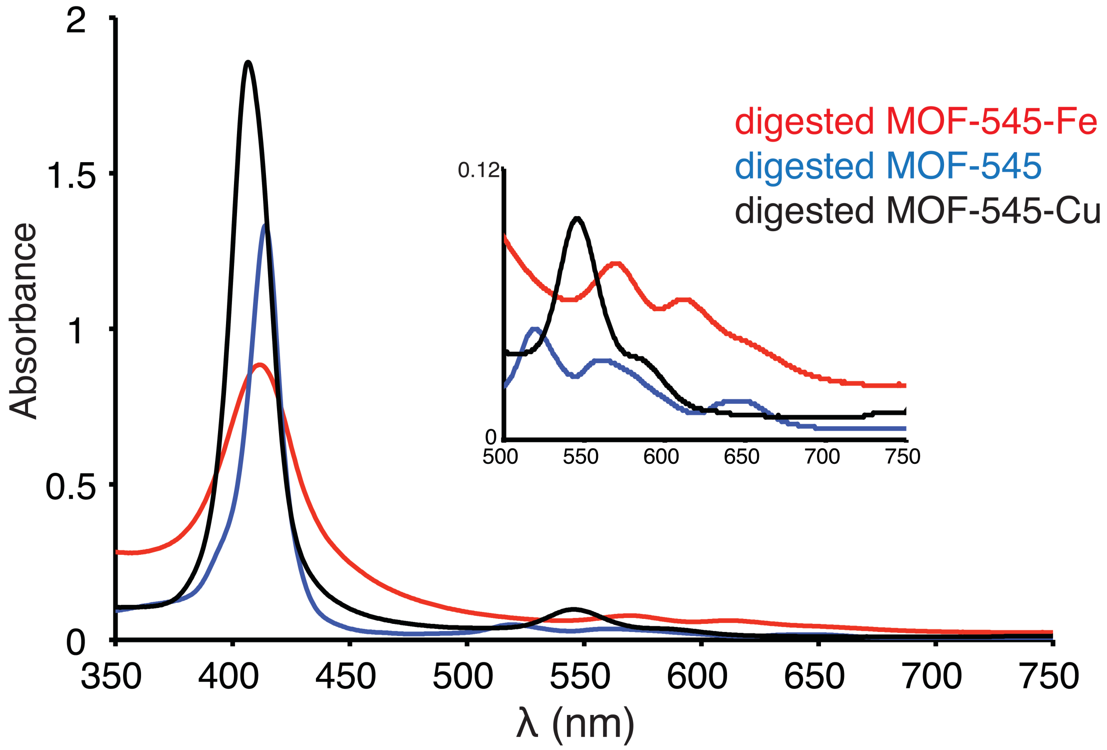

Figure 22) UV-Visible spectra of digested, MOF-545-Fe (red), MOF-545 (blue), and MOF-545-Cu (black).

Tables

Table 1) Fractional atomic coordinates for MOF-525 calculated from the *Materials Studio software.*

MOF-525

Space Group	Volume
$Pm\bar{3}m$ (Origin choice 1)	7293.5 Å^3

$a = b = c$ = 19.393(3) Å

a = b = g = 90°

Atom	Occupancy	*X*	*Y*	*Z*
Zr1	1	0.12089	0.0000	0.00000
O2	1	0.06310	0.06310	0.06310
O3	1	1.00000	0.17742	0.09315
N4	1	1.0000	0.39584	0.50000
C5	1	1.0000	0.19315	0.28106
C6	1	1.0000	0.24461	0.33179
C7	1	1.00000	0.35301	0.55606
C8	1	1.37263	0.00000	0.37263
C9	1	1.00000	0.31586	0.31586
C10	1	1.00000	0.15710	0.15710
C11	1	1.00000	0.21106	0.21106
C12	1	0.53491	0.00000	0.28507

Table 2) Final statistics from MOF-525.

Name	**MOF-525**
Composition	$Zr_6O_{28}N_{12}C_{144}$
Mass formula (g mol^{-1})	2609.69
Crystal system	Cubic
Space group	$Pm\bar{3}m$ (No. 221)
a (Å)	19.393 (3)
V (Å^3)	7293.48
Crystal density (g cm^{-3})	0.676 (3)
Number of reflections	256
Number of independent atoms	12
R_p (%)	8.98
R_{wp} (%)	12.28

Table 3) Crystal data and structure refinement for MOF-535 before squeeze.

Identification code	MOF-535	
Empirical formula	C152 O162 Zr6	
Formula weight	4964.84	
Temperature	100 K	
Wavelength	0.9201 Å	
Crystal system	Cubic	
Space group	$Pm\bar{3}m$	
Unit cell dimensions	a = 19.410(2) Å	a = 90°
	b = 19.410(2) Å	b = 90°
	c = 19.410(2) Å	g = 90°
Volume	7312.7(14) Å^3	
Z	1	

Density (calculated)	1.127 Mg/m^3	
Absorption coefficient	0.299 mm^{-1}	
F(000)	2448	
Crystal size	0.1 × 0.1 × 0.1 mm	
Theta range for data collection	3.15 to 19.76°	
Index ranges	-18<=h<=17, -17<=k<=18, -17<=l<=18	
Reflections collected	15466	
Independent reflections	712 [R(int) = 0.0251]	
Completeness to theta = 19.76°	97.8%	
Absorption correction	None	
Refinement method	Full-matrix least-squares on F^2	
Data / restraints / parameters	712 / 0 / 61	
Goodness-of-fit on F^2	4.760	
Final R indices [I>2sigma(I)]	R1 = 0.2874, wR2 = 0.6971	
R indices (all data)	R1 = 0.2874, wR2 = 0.6971	
Largest diff. peak and hole	1.249 and -1.541 e.Å^{-3}	

Table 4) Crystal data and structure refinement for MOF-535 after squeeze

Identification code	MOF-535	
Empirical formula	C136 O32 Zr6	
Formula weight	2692.68	
Temperature	100 K	
Wavelength	0.9201 Å	
Crystal system	Cubic	
Space group	$Pm\bar{3}m$	
Unit cell dimensions	*a* = 19.410(2) Å	a = 90°
	b = 19.410(2) Å	b = 90°
	c = 19.410(2) Å	g = 90°
Volume	7312.7(14) Å^3	
Z	1	
Density (calculated)	0.611 Mg/m^3	
Absorption coefficient	0.238 mm^{-1}	
F(000)	1312	
Crystal size	0.1 × 0.1 × 0.1 mm	
Theta range for data collection	3.15 to 19.76°	
Index ranges	-18<=h<=17, -17<=k<=18, -17<=l<=18	
Reflections collected	15466	

Independent reflections	712 [R(int) = 0.0257]
Completeness to theta = 19.76°	97.8%
Absorption correction	None
Refinement method	Full-matrix least-squares on F^2
Data / restraints / parameters	712 / 0 / 37
Goodness-of-fit on F^2	3.851
Final R indices [I>2sigma(I)]	R1 = 0.1860, wR2 = 0.6270
R indices (all data)	R1 = 0.1865, wR2 = 0.6287
Largest diff. peak and hole	0.583 and -1.250 e.Å^{-3}

Table 5) Crystal data and structure refinement for MOF-545-Fe before squeeze.

Identification code	MOF-545-Fe	
Empirical formula	C288 O150 Zr18 Fe6 N24 Cl6	
Formula weight	8554.22	
Temperature	100 K	
Wavelength	0.9201 Å	
Crystal system	Hexagonal	
Space group	*P*6/*mmm*	
Unit cell dimensions	a = 42.680(6) Å	a = 90°
	b = 42.680(6) Å	b = 90°
	c = 16.660(3) Å	g = 120°
Volume	26282(7) Å^3	
Z	1	
Density (calculated)	0.54 Mg/m^3	
Absorption coefficient	0.298 mm^{-1}	
F(000)	2448	
Crystal size	0.2 × 0.025 × 0.025 mm^3	
Theta range for data collection	1.34 to 20.78°	
Index ranges	-39<=h<=39, -40<=k<=39, -14<=l<=14	
Reflections collected	75203	
Independent reflections	4672 [R(int) = 0.0313]	
Completeness to theta = 20.78°	90.3%	
Absorption correction	None	
Refinement method	Full-matrix least-squares on F^2	
Data / restraints / parameters	4672 / 0 / 202	
Goodness-of-fit on F^2	2.329	
Final R indices [I>2sigma(I)]	R1 = 0.1575, wR2 = 0.4901	
R indices (all data)	R1 = 0.1689, wR2 = 0.4959	
Largest diff. peak and hole	0.991 and -1.651 e.Å^{-3}	

Table 6) Crystal data and structure refinement for MOF-545-Fe after squeeze.

Identification code	MOF-545-Fe
Empirical formula	C288 O150 Zr18 Fe6 N24 Cl6
Formula weight	8554.22

Temperature	100 K	
Wavelength	0.9201 Å	
Crystal system	Hexagonal	
Space group	*P*6/*mmm*	
Unit cell dimensions	*a* = 42.680(6) Å	a = 90°
	b = 42.680(6) Å	b = 90°
	c = 16.660(3) Å	g = 120°
Volume	26282(7) Å^3	
Z	1	
Density (calculated)	0.54 Mg/m^3	
Absorption coefficient	0.298 mm^{-1}	
F(000)	2448	
Crystal size	0.2 × 0.025 × 0.025 mm	
Theta range for data collection	1.34 to 20.78°	
Index ranges	-39<=h<=39, -40<=k<=39, -14<=l<=14	
Reflections collected	75203	
Independent reflections	4672 [R(int) = 0.0313]	
Completeness to theta = 20.78°	90.3%	
Absorption correction	None	
Refinement method	Full-matrix least-squares on F^2	
Data / restraints / parameters	4672 / 0 / 202	
Goodness-of-fit on F^2	1.042	
Final R indices [I>2sigma(I)]	R1 = 0.0779, wR2 = 0.2335	
R indices (all data)	R1 = 0.0930, wR2 = 0.2482	
Largest diff. peak and hole	0.751 and -1.543 e.Å^{-3}	

References

1) (a) Cavka, J. H.; Jakobsen, S.; Olsbye, U.; Guillou, N.; Lamberti, C.; Bordiga, S.; Lillerud, K. P. *J. Am. Chem. Soc.* **2008**, *130*, 13850.
2) Morris, W.; Doonan, C. J.; Yaghi, O. M. *Inorg. Chem*. **2011**, *50*, 6853. (b) Garibay, S. J.; Cohen, S. M. *Chem. Commun.* **2010**, *46*, 7700.
3) Li, H.; Eddaoudi, M.; O'Keeffe, M.; Yaghi, O. M.; *Nature*, **1999**, *402*, 276

4) Schaate, A.; Roy, P.; Preube, T.; Lohmeier, S. J.; Godt, A.; Behrens, P. Chem. Eur. J. 2011, 17, 9320. (b) Godt, A.; Lippke, J.; Waltz, F.; Wiebcke, M.; Behrens, P. Chem. Eur. J. 2011, 17, 6643.

5) Furukawa, H.; Ko, N.; Go, Y. B.; Aratani, N.; Choi, S. B.; Choi, E.; Yazaydin, A. O.; Snurr, R. Q.; O'Keeffe, M.; Kim, J.; Yaghi, O. M. *Science*, **2010**, *239,* 424

6) Stephenson, N. A.; Bell, A. T. J. Mol. Catal. A: Chem. 2007, 275, 54.

7) (a) Caskey, S. R.; Wong-Foy, A. G.; Matzger, A. J. *J. Am. Chem. Soc.* **2008**, *130*, 10870. (b) Britt, D.; Furukawa, H.; Wang, B.; Glover, T. G.; Yaghi, O. M. *Proc. Natl. Acad. Sci. U.S.A*. **2009**, *106*, 20637. (c) Phan, A.; Czaja, A. U.; Gándara, F.; Knobler, C. B.; Yaghi, O. M. *Inorg. Chem.* **2011**, *50*, 7388.

8) (a) Morris, W.; Doonan, C. J.; Furukawa, H.; Banerjee, R.; Yaghi, O. M. J. Am. Chem. Soc. 2008, 130, 12626. (b) Tanabe, K. K.; Cohen, S. M. Angew. Chem. Int. Ed. 2009, 48, 7424. (c) Chen, B.; Eddaoudi, M.; Reineke, T. M.; Kampf, J. W.; O'Keeffe, M.; Yaghi, O. M. J. Am. Chem. Soc. 2000, 122, 15599. (d) Rosi, N. L.; Kim, J.; Chen, B.; Eddaoudi, M.; O'Keeffe, M.; Yaghi, O. M. J. Am. Chem. Soc. 2005, 127, 1504.

9) (a) Abrahams, B. F.; Hoskins, B. F.; Michail, D. M.; Robson, R. *Nature.* **1994**, *369*, 727. (b) Suslick, K. S.; Bhyrappa, P.; Chou, J. H.; Kosal, M. E.; Nakagaki, S.; Smithenry, D. W.; Wilson, S. R. *Acc. Chem. Res.* **2005**, *38*, 283. (c) Barron, P. M.; Wray, C. A.; Hu, C.; Guo, Z.; Choe, W. *Inorg. Chem*, **2010**, *49*, 10217. (d) Wang, X.; Meng, L.; Cheng, Q.; Kim, C.; Wojtas, L.; Chrzanowski, M.; Chen, Y.; Zhang, P.; Ma, S. *J. Am. Chem. Soc.* **2011**, *133*, 16322.

10) Shultz, A. M.; Farha, O. K.; Hupp, J. T.; Nguyen, S. T. *J. Am. Chem. Soc.* **2009**, *131*, 4204.

11) (a) Farha, O. K.; Shultz, A. M.; Sarjeant, A. A.; Nguyen, S. T.; Hupp, J. T. *J. Am. Chem. Soc.* **2011**, *133*, 5652. Fateeva, A.; Devautour-Vinot, S.; Heymans, N.; Devic, T.; Grenèche, J. M.; Wuttke, S.; Miller, S.; Lago, A.; Serre, C.; Weireld, G. D.; Maurin, G.; Vimont, A.; Férey, G. *Chem. Mater.* **2011**, *23*, 4641.

12) Ockwig, N. W.; Delgado-Friedrichs, O.; O'Keeffe, M.; Yaghi, O. M. *Acc. Chem. Res.* **2005**, *38*, 176. (b) O'Keeffe, M.; Peskov, M. A.; Ramsden, S. J.; Yaghi, O. M. *Acc. Chem. Res.* **2008**, *41*, 1782. (c) RCSR can be accessed at http://rcsr.anu.edu.eu/

13) (a) Côté, A. P.; El-Kaderi, H. M.; Furukawa, H.; Hunt, J. R.; Yaghi, O. M. *J. Am. Chem. Soc.* **2007**, *129*, 12914. (b) Uribe-Romo, F. J.; Hunt, J. R.; Furukawa, H.; Klöck, C.; O'Keeffe, M.; Yaghi, O. M. *J. Am. Chem. Soc.* **2009**, *131*, 4570

14) Sheldrick, G. M. *Acta Crystallographica Section A.* **2008**, *64*, 112.

Fleischer, E. B. *Acc. Chem. Res,* 1970, 3, 105.

Chapter Six

Synthesis of New Zeolitic Imidazolate Frameworks (ZIFs) Incorporating Novel Functionalities and their Gas Adsorption.

Introduction

Gas adsorption, separation, and storage are of great importance in modern society for many purposes, including transport, purification, and the delay of global warming.[1] Current technologies and materials for these gas adsorption applications include amine scrubbing, zeolites, and activated carbons.[2] However, these technologies and materials have disadvantages; for example, a power plant employing amine-scrubbing technology to remove CO_2 would consume a third of the energy produced by that plant to remove CO_2.[3] Therefore to replace current technologies, new materials must have a high adsorption capacity, low regeneration costs, thermal, and chemical stability.

Zeolitic imidazolate frameworks (ZIFs) have high chemical stability and large surface areas, often exceeding 1000 m^2/g BET, making them potential replacements in gas adsorption applications.[4] For example, ZIF-8 ($Zn(C_4H_5N_2)_2$) retains its porosity and crystallinity after exposure to acidic and basic conditions.[5] These high surface area materials, which incorporate high chemical and thermal stability, have been studied for applications in gas adsorption, separation, and catalysis.[6] This high chemical stability combined with the high surface area, will allow ZIFs to be deployed in harsh environments, potentially replacing current technologies. There have been several studies of carbon capture in ZIFs; however, little is known about the factors that influence gas adsorption in these materials because several factors influence gas adsorption, including ZIF topology, functionalities on the imidazolate, and the metal ion. Therefore, studies of each of these variables independently are valuable in designing the best frameworks for gas adsorption.

A large group of ZIFs have been synthesized using high-throughput techniques and solvothermal methods; these materials encompass a diverse range of structures (**Scheme 1**).[7] This array of structures highlights the variation in these ZIFs, in that the imidazolate, metal ion, topology, pore size, and pore structure are all seen to vary (**Scheme 1**). In this chapter, we describe the synthesis of an isoreticular series of ZIFs; these ZIFs only vary in the functionalities that decorate the 4-5 position of the imidazolate, which points into the pore of the **rho** topology (**Scheme 2**). This allows for the study of gas adsorption as a factor of functionality, with detailed studies allowing a conclusion to be drawn on about functionality affects CH_4 and CO_2 adsorption.

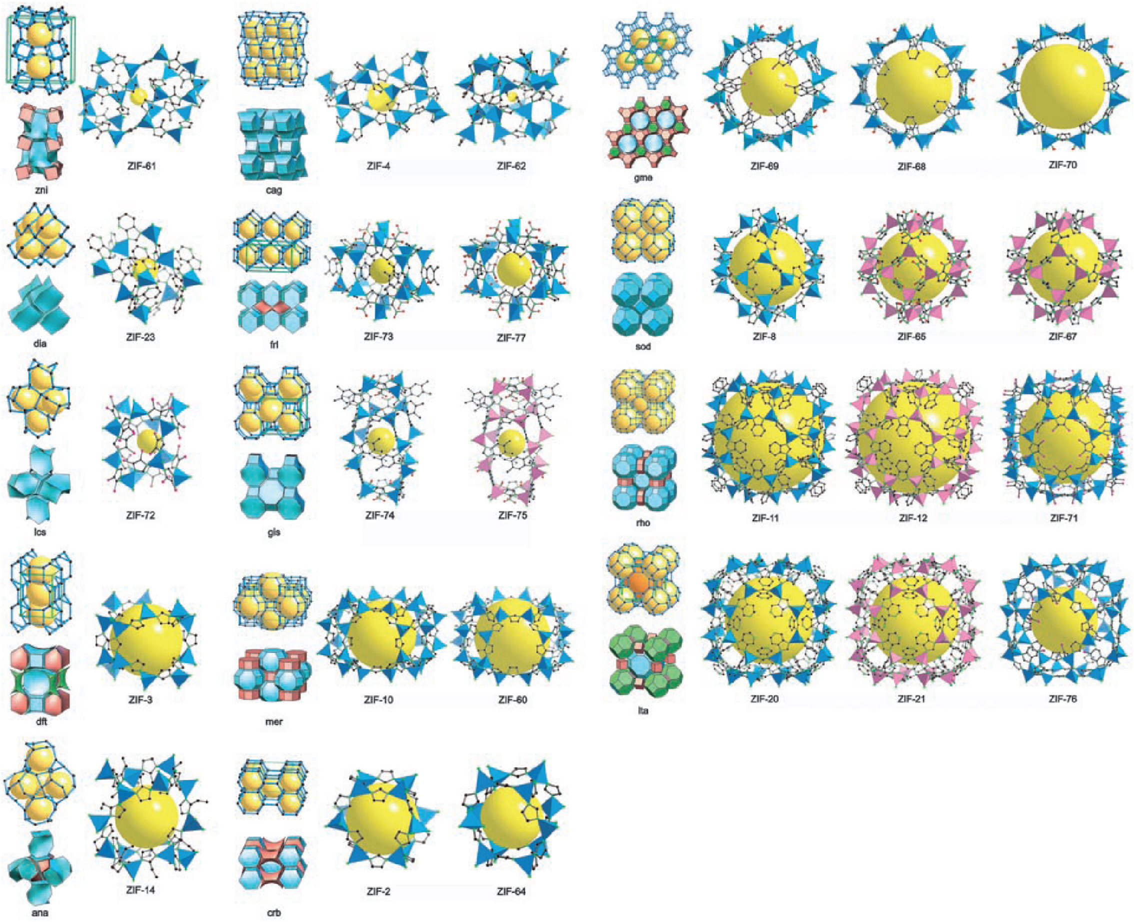

Scheme 1) A selection of ZIFs reported in the literature and their topologies.[7]

Five ZIFs were synthesized with the **rho** topology, namely, ZIF-25, 71, 93, 96 and 97; incorporating the functionalized imidazolates, $C_5H_8N_2$, $C_3H_2N_2Cl_2$, $C_5H_6N_2O$, $C_4H_4N_4$, and $C_5H_8N_2O$, respectively (**Scheme 2**). These ZIF materials were isolated as microcrystalline powders unsuitable for single crystal analyses. Their structures were confirmed by first modeling the respective **rho** topologies and then comparing the calculated PXRD patterns from the model to the experimental PXRD. A complete structural analysis was performed by a Rietveld study of the PXRD, a technique which has been used to solve the structure of many microcrystalline powders. To confirm the functionalization of the pores a CP/MAS ^{13}C NMR spectrum and an FT-IR spectrum were measured for each ZIF, confirming that the respective functionalities were incorporated into each of them.

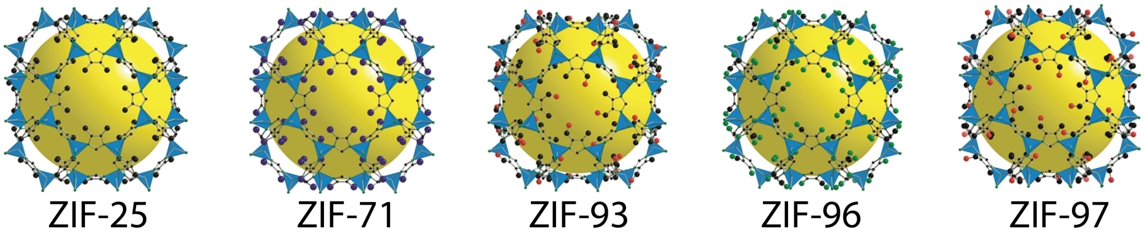
ZIF-25 ZIF-71 ZIF-93 ZIF-96 ZIF-97

Scheme 2) Structure of the isoreticular ZIF series.

The N_2 isotherms of the ZIFs were Type I in shape indicative of permanent microporosity. The surface areas of this series of ZIFs were shown to be directly proportional to their densities; the lowest density material, ZIF-25, has the highest BET surface area, 1100 m^2/g. Each ZIF in the isoreticular series has the same topology and metal ion, but has different functionalities at the 4,5 positions of the imidazolate. Therefore, due to the isoreticular nature of these ZIFs with permanent porosity, the study of gas adsorption as a factor of functionality was possible.

We chose to study the adsorption of CO_2 and CH_4 in these ZIFs using a combination of experiment and theory; these studies revealed relationships between surface area, functionalization, and total gas uptake. Experiments showed that CO_2 adsorption exhibited a strong dependence on functionality, with CH_4 adsorption directly proportional to surface area. Theory supported experiments highlighting the strong binding sites within each ZIF framework, which were enhanced by functionality in the case of CO_2 adsorption.

Experimental

Reagents and general procedures.

All reagents unless otherwise stated were obtained from commercial sources (Alfa Aesar, Cambridge isotope laboratories, Sigma Aldrich, TCI) and were used without further purification. Yields reported were unoptimized. Elemental microanalyses were performed at the University of California, Los Angeles, Department of Chemistry and Biochemistry.

Synthetic procedures for ZIF-25, -71,-93,-96, and -97

ZIF-25: $Zn(C_5H_7N_2)_2$ = Zn(dmIm)$_2$. A solution of zinc acetate $Zn(O_2CCH_3)_2$ (0.147 g, 0.8 mmol) in 8 mL N,N-dimethylformamide and a solution of 4,5-dimethylimidazole (0.233 g, 2.4 mmol) in 8 mL N,N-dimethylformamide was sealed in a 20 mL vial, and heated in an oven at 125 °C, and allowed to react solvothermally for 12 h. The mother liquor was decanted and the crystalline powder was washed with chloroform (3 × 5 mL). The product was activated with chloroform (3 × 10 mL) over three days before drying under vacuum (0.01 Torr) for 24 h at 80 ˚C. Yield: 0.0269 g, 76% based on 4,5-dimethylimidazole. $C_{10}H_{14}N_4Zn = Zn(C_5H_7N_2)_2$, calcd: C, 46.98%; H, 5.52%; N, 21.92%. Found: C, 46.45%; H, 5.60%; N, 21.74%.

ZIF-71: $Zn(C_3HCl_2N_2)_2$ = Zn(dcIm)$_2$. A solution of zinc acetate $Zn(O_2CCH_3)_2$ (0.147 g, 0.8 mmol) in 8 mL *N*,*N*-dimethylformamide and a solution of 4,5-dichloroimidazole

(0.329 g, 2.4 mmol) in 8 mL *N*,*N*-dimethylformamide was combined and sealed in a 20 mL vial, heated in an oven at 85 °C, and allowed to react solvothermally for 12 h. The mother liquor was decanted and the crystalline powder was washed with chloroform (3 × 5 mL). The product was activated with chloroform (3 × 10 mL) over three days before drying under vacuum (0.01 Torr) for 24 h at 80 ˚C. Yield: 0.0183 g, 68% based on 4,5-dichloroimidazole. $C_6H_2N_4Cl_4Zn$ = $Zn(C_3H_1N_2Cl_2)_2$, calcd: C, 21.3%; H, 0.60%; N, 16.61%. Found: C, 21.20%; H, 0.84 %; N, 16.31%.

ZIF-93: $Zn(C_5H_5N_2O)_2$ = Zn(4me5alIm)$_2$. A solution of zinc acetate ($Zn(O_2CCH_3)_2$) (0.147 g, 0.8 mmol) in 8 mL *N*,*N*-dimethylformamide and a solution of 4-methylimidazole-5-carbaldehyde (0.264 g, 2.4 mmol) in 8 mL *N*,*N*-dimethylformamide was combined and sealed in a 20 mL vial, heated in an oven at 85 °C, and allowed to react solvothermally for 12 h. The mother liquor was decanted and the crystalline powder was washed with chloroform (3 × 5 mL). The product was activated with chloroform (3 × 10 mL) over three days before drying under vacuum (0.01 Torr) for 24 h at 80 ˚C. Yield: 0.0191 g, 84% based on 4-methylimidazole-5-carbaldehyde. $C_{10}H_{10}N_4O_2Zn$ = $Zn(C_5H_5N_2O)_2$, calcd: C, 42.35%; H, 3.55%; N, 19.79%. Found C 42.01%, H 3.60%, N 19.64%.

ZIF-94

ZIF-96: $Zn(C_4H_3N_4)_2$ = Zn(4cy5amIm)$_2$. A solution of zinc acetate ($Zn(O_2CCH_3)_2$) (0.147 g, 0.8 mmol) in 8 mL of *N*,*N*-dimethylformamide and a solution of 4-aminoimidazole-5-carbonitrile (0.2592 g, 2.4 mmol) in 8 mL *N*,*N*-dimethylformamide were combined and sealed in a 20 mL vial, heated in an oven at 85 °C, and allowed to react solvothermally for 12 h. The mother liquor was decanted and the crystalline powder was washed with diethyl ether (3 × 5 mL). The product was activated with diethyl ether (3 × 10 mL) over three days before drying under vacuum (0.01 Torr) for 24 h at 80 ˚C. Yield: 0.0161 g, 72% based on 4-aminoimidazole-5-carbonitrile. $C_8H_6N_8Zn$ = $Zn(C_4H_3N_4)_2$, calcd: C, 34.37%; H, 2.16%; N, 40.08%. Found: C, 34.00%; H, 1.99%; N, 39.41%.

ZIF-97: $Zn(C_5H_7N_2O)_2$ = $Zn(4mehylIm)_2$. A solution of zinc acetate ($Zn(O_2CCH_3)_2$) (0.1519 g, 0.8 mmol) in 8 mL *N*,*N*-dimethylformamide and a solution of 4-hydroxymethyl-5-methylimidazole (0.269 g, 2.4 mmol) in 10 mL *N*,*N*-dimethylformamide were combined and sealed in a 20 mL vial, heated in an oven at 100 °C, and allowed to react solvothermally for 12 h. The mother liquor was decanted, and the crystalline powder was washed with diethyl ether (3 × 5 mL). The product was activated with diethyl ether (3 × 10 mL) over three days before drying under vacuum (0.01 Torr) for 24 h at 80 °C. Yield: 0.0145 g, 63 % based on 4-hydroxymethyl-5-methylimidazole. $C_{10}H_{16}N_4O_3Zn$ = $Zn(C_5H_7N_2O)_2 \cdot H_2O$, calcd: C, 39.29%; H, 5.28%; N, 18.33%. Found: C, 40.01%; H, 5.11%; N, 18.68%.

Structure resolution from Powder X-Ray Diffractrometry (PXRD)

Powder X-ray data were collected using a Bruker D8-Discover θ-2θ diffractometer in reflectance Bragg-Brentano geometry employing Ni filtered Cu Kα line focused radiation at 1600 W (40 kV, 40 mA) power and equipped with a Vantec Line detector. Radiation was focused using parallel focusing Gobel mirrors. The system was also outfitted with an anti-scattering shield that prevents incident diffuse radiation from hitting the detector, preventing the normally large background at $2\theta < 3$. Samples were mounted on zero background sample holders by dropping powders from a wide-blade spatula and then leveling the sample with a razor blade.

Crystal structure modeling. The models for ZIF-25, -93, -96, and -97, including cell parameters and atomic positions, were generated using Material Studio chemical structure-modeling software employing the Crystal Building module.[8] The structure of each ZIF was generated using the relevant space group, the cell parameters were used as obtained, and atom positions were generated from single crystal data of ZIF-71. The constructed structure was minimized with the Forcite module using the Geometry Optimization routine with the Universal force field (UFF).[9] The obtained model was used as input for Rietveld refinement.

Rietveld refinement. The Rietveld refinement was performed using Topas from Bruker including data from $2\theta = 5 - 70^\circ$. Prior to the Rietveld refinement, a profile fitting was performed using the Pauley refinement method.[10] The profile obtained from Pawley fitting and the model generated, were used as a starting set. The profile used was a Thomson-Cox-Hasting Pseudo Voigt function with 6 terms (TCHZ peak type) with a 20th order Chebychev polynomial and Finger-Cox-Jephcoat peak asymmetry (2 parameters). Unit cell parameters, zero-shift correction, Lorentz polarization, linear absorption, scale, crystallite size, and strain were refined observing convergent refinements. Hydrogen atoms were not included in the refinements.

Solid state ^{13}C CP/MAS nuclear magnetic resonance spectroscopy

High Resolution solid-state nuclear magnetic resonance (NMR) spectra were recorded at ambient pressure on a Bruker DSX-300 spectrometer using a standard Bruker magic angle-spinning (MAS) probe with 4 mm (outside diameter) zirconia rotors. The magic angle was adjusted by maximizing the number and amplitudes of the signals of the rotational echoes observed in the ^{79}Br MAS FID signal from KBr. Cross-polarization with MAS (CP/MAS) was used to acquire ^{13}C data at 75.47 MHz. The ^{1}H and ^{13}C ninety-degree pulse widths were both 4 ms. The CP contact time varied from 1.5 to 5 ms. High power two-pulse phase modulation (TPPM) ^{1}H decoupling was applied during data acquisition. The decoupling frequency corresponded to 72 kHz. The MAS sample-spinning rate was 10 kHz. Recycle delays between scans varied between 3 and 10 s, depending upon the compound as determined by observing no apparent loss in the ^{13}C signal from one scan to the next. The ^{13}C chemical shifts are given relative to tetramethylsilane as zero ppm, calibrated using the methylene carbon signal of adamantane assigned to 37.77 ppm as the secondary reference.

Nitrogen gas adsorption measurements, and calculation of surface area by the BET method

Low-pressure gas adsorption isotherms were measured volumetrically on an Autosorb-1 analyzer (Quantachrome Instruments). A liquid nitrogen sample bath (77 K) was used for N_2 measurements. The N_2 gas used was UHP grade. For measurement of the apparent surface areas (S_{BET}), the BET method was applied using the adsorption branches of the N_2 isotherms assuming a N_2 cross-sectional area of 16.2 Å^2/molecule.

Fourier transform infrared spectroscopy

FT-IR spectra of the synthesized ZIFs were obtained as KBr pellets using a Nicolet 400 Impact spectrometer; signals are given in wavenumbers (cm^{-1}).

Experimental CO_2 and CH_4 isotherms.

Low-pressure gas adsorption isotherms were measured volumetrically on an Autosorb-1 analyzer (Quantachrome Instruments). A constant temperature water bath (at 298 K) was used for CO_2 measurements. The CO_2 gas used was UHP grade. Error of these measurements is +/- 2%.

Results and Discussion

Synthesis and structure of ZIF frameworks The synthesis of five ZIFs was achieved; ZIF-25, -71, -93, -96, and -97 (**Figure 1**) have the **rho** topology. For example, ZIF-25 was synthesized by first preparing two solutions, one of zinc acetate $Zn(O_2CCH_3)_2$ (0.147 g, 0.8 mmol) in 8 mL N,N-dimethylformamide and the other of 4,5-dimethylimidazole (0.233 g, 2.4 mmol) in 8 mL N,N-dimethylformamide. The two solutions were added to a 20 mL vial, and heated in an oven at 125 °C. The reaction was then allowed to react solvothermally for 12 h. The ZIFs synthesized varied only in the imidazolate that decorated the pores; each ZIF offers a different decoration of organic functionalities, **dmIm** (ZIF-25), **dcIm** (ZIF-71), **almeIm** (ZIF-93), **cyamIm** (ZIF-96), and **hymeIm** (ZIF-97) (**Figure 1**). Unlike other ZIF syntheses these reactions proceed in the presence of zinc acetate, the acetate rapidly depronating the imidazole, allowing for rapid formation of a homogeneous crystalline powder as evidenced by SEM (**Figure 2**). Other synthetic procedures including solvothermal reactions led to small yields or production of amorphous products.

Due to the microcrystalline nature of these ZIFs, the **rho** topology was initially confirmed by comparison of the PXRD data to that for the structure of ZIF-71, generated from single crystal data (**Figure 3**).[8] To further characterize the ZIFs, the activation of each structure was first optimized by trying a variety of activation conditions; these activation conditions involved altering exchange solvent (diethyl ether, acetone, MeOH, EtOH, etc), evacuation time, and evacuation temperature. To confirm that each structure was activated, the elemental microanalysis was shown to be consistent with the fully activated framework. The optimal activation solvent was found to be diethyl ether (ZIF-96, -97) or $CHCl_3$ (ZIF-25, -71, and -93) followed by evacuation at 100 ˚C. Following activation

Rietveld analysis of ZIF-25, ZIF-93, ZIF-96, and ZIF-97 confirmed the **rho** topology (**Figure 4**), by comparison of the experimental data with modeling data. Rietveld analysis of each ZIF showed good refinement parameters (**Table 1**). Rietveld analysis confirmed the position of all the atoms within each cubic unit cell; ZIFs with symmetrical functionalities in the 4,5-position on the imidazolate belonging to space group Im-3m and unsymmetrical functionalities in the 4,5 position imidazolate belonging to space group I432 (**Table 2-5**).

The **rho** topology is comprised of two cages, the **lta** cage and **d8r** cage (**Figure 5**). The large **lta** cage has 48 vertices and 26 faces comprised of 12 squares, 8 hexagons, and 6 octagons (**Figure 5**). The smaller **d8r** cage has 24 vertices and is comprised of eight squares and two octagons (**Figure 5**). These structures are decorated with different organic functionalities, which point into the **lta** and **d8r** pores of these frameworks.

To confirm the presence of the functional groups in the activated samples, FTIR and ^{13}C cross polarization magic angle spinning (CP/MAS) NMR were performed on activated samples of each ZIF (**Figure 6-7**). The FTIR showed characteristic stretches for -CN and –CHO, stretches present at 2176 and 1669 cm^{-1} for ZIF-93 and -96, respectively (**Figure 6**). The CP/MAS solid state NMR shows the presence of all the expected functionalities (Figure x). We observe the presence of the -CH_3 functionality of ZIF-25, -93, and -97 at 9, 11, and 11 ppm, respectively, the -CHO functionality at 180 ppm for ZIF-93; the -CN functionality at 80 ppm for ZIF-96; and the -CH_2OH functionality at 60 ppm for ZIF-97 (**Figure 7**). Furthermore, these techniques confirm the homogenous nature of the samples and no additional organic groups were observed in the ZIF samples.

Gas adsorption in isoreticular ZIF series. After activation, the N_2 isotherm at 77 K was measured for each ZIF; each isotherm was Type I in shape, indicative of the permanent microporosity of these frameworks (**Figure 8**). The surface area of the ZIFs was evaluated by BET fitting of the N_2 isotherms at 77 K. ZIF-25 has the highest surface area, 1110 m^2/g, with a surface area found to be directly proportional to the density in this series of ZIFs (**Table 6**). This series of frameworks exhibits high porosity making them ideal for studies of their gas adsorption. In addition, the only significant difference across these frameworks is the variation in functionality observed in the decoration of the pore; other properties including the metal ion, topology and pore size remaining consistent (**Table 6**).

The CH_4 and CO_2 adsorption of each ZIF was measured at 298 K (**Figure 9**). ZIF-25 had the highest uptake of CH_4 0.6 $mmol/g^{-1}$, and ZIF-96 had the highest uptake of CO_2, 2.11 $mmol/g^{-1}$. In both the CH_4 and the CO_2 adsorption measurements the framework with the highest density, ZIF-71, adsorbed the smallest amount of CO_2 and CH_4. CH_4 adsorption was proportional to the surface area throughout the frameworks (**Figure 9**). However, the CO_2 adsorption was found not to be directly proportional to the surface area, due to interactions between the functionalities within the pores and the CO_2. To further understand the role of functionality, the enthalpy of the CO_2 and the CH_4 adsorption was calculated as a factor of coverage for each ZIF (**Figure 9**). The initial enthalpies of adsorption were shown to vary by only 2 KJ/mol^{-1} for methane, again confirming that functionality does not play a large role in the adsorption of methane. The initial enthalpy of CO_2 adsorption was shown to vary by up to 50 %; this further confirms that functionality plays a role in CO_2 adsorption; functionality strongly contributes to the initial binding sites.

To understand these relationships further, simulations of CO_2 and CH_4 adsorption were carried out at 298 K. The simulation results for CH_4 were shown to be in excellent agreement with the experimental isotherms (**Figure 10**), confirming the dependence of CH_4 adsorption on the surface area. Simulated adsorption of CO_2 also is in excellent agreement with the experimental results, showing that CO_2 uptake was not directly proportional to the surface area; the highest performers again are ZIF-96 and ZIF-93 (**Figure 10**). To further understand the role of the binding sites, the initial enthalpies of adsorption were calculated from the simulation. CH_4 initial enthalpies of adsorption were shown to deviate by only 5 KJ/mol^{-1}; in contrast, CO_2 enthalpies were shown to vary by 15 KJ/mol^{-1}, with ZIF-93 showing the highest enthalpy of adsorption, 29 KJ/mol^{-1} (**Table 6**). These simulation results confirm the experimental observations showing that functionality clearly influences CO_2 adsorption.

To understand the respective CO_2 binding sites within the framework, equilibrium CO_2 density maps were calculated (**Figure 11**). These maps highlight primary adsorption of CO_2 at the hexagonal faces of the **lta** cavities and secondary adsorption sites in the smaller **d8r** cages. These adsorption sites are highly dependent on functionality; ZIF-93 and ZIF-96 showing the highest magnitude sites for CO_2 adsorption.

Conclusions

Five ZIF frameworks were synthesized as microcrystalline powder, by rapid deprotonation of a functionalized imidazole to form a homogenous microcrystalline powder. The structure of these ZIFs was resolved from the PXRD data; with each ZIF has the **rho** topology, which is comprised of two pores, the large **lta** cage and the smaller **d8r** cage. The cages are decorated with different ffuhctionalities, including –CH_3 (ZIF-25, -93, and -97), -Cl (ZIF-71), -CHO (ZIF-93), -CN (ZIF-96), -NH_2 (ZIF-96), and –OH (ZIF-97). The evacuation of each ZIF was optimized to obtain a solvent-free framework; different solvents were used to activate each framework. To confirm the incorporation of the functionalities, ^{13}C CP/MAS solid state NMR and FTIR were measured, showing the expected carbon resonances and stretches, respectively.

The isoreticular nature of these ZIFs makes them ideal for the study of gas adsorption, unlike other studies of gas adsorption; in ZIFs only one variable changes throughout these frameworks. Firstly, N_2 isotherms were used to determine the BET surface area of each framework; the surface area is shown to scale with density. Two gases were selected for adsorption measurements, CO_2 and CH_4, because of their importance in current adsorption applications. CH_4 adsorption was shown to be directly proportional to the surface area; the highest surface area material has the highest adsorption of CH_4. In addition, the initial enthalpy of adsorption was shown to vary by only 2 KJ/mol^{-1}, further demonstrating that functionalities do not significantly affect CH_4 adsorption. In contrast, CO_2 adsorption was not proportional to the surface area; functionalities including –NH_2 and –CHO enhance CO_2 adsorption, highlighted by higher adsorption and higher enthalpies of adsorption in ZIF-93 and ZIF-96. Simulations of isotherms and enthalpies of adsorption showed similar trends, supporting the experimental results. To further understand these results, CO_2 equilibrium maps were calculated, which pointed out the variation in CO_2 adsorption around the functionalities and the importance of the cage size with the small cages of these ZIFs, offering the strongest adsorption sites.

New synthetic methods allowed the synthesis of an isoreticular series of ZIFs suitable for the study of gas adsorption. The incorporation of functionality was shown to enhance CO_2 adsorption. The ability to add multiple functionalities to the organic link of ZIFs and MOFs must be investigated, as addition of multiple functionalities may have an additive effect on gas adsorption, leading to significant increases over the non-functionalized or mono-functionalized framework. Further studies of ZIFs must be carried out to investigate the role of topology and the metal ion on gas adsorption. The stability of the future materials in the adsorption process is key, as multiple cycling of materials for adsorption processes, often under harsh conditions will be required, making ZIFs an attractive option.

Figures

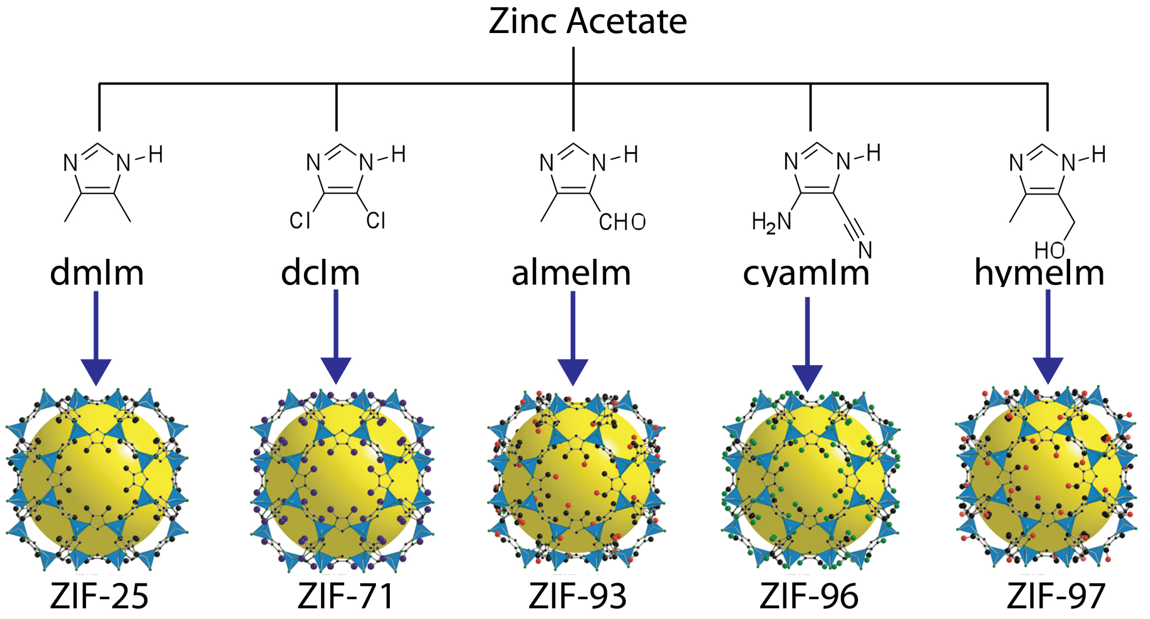

Figure 1) Synthesis of an isoreticular ZIF series. The series of links **dmeIm**, **dcIm**, **almeIm**, **cyamIm,** and **hymeIm** used for the isoreticular ZIFs. The structure of one cage that is linked together to make the structures of ZIF-25, 71, 93, 96, and 97. The yellow ball within the cage represents the free space. Atom colors: zinc, blue tetrahedra; carbon, black; chlorine, dark blue; oxygen, red; nitrogen, green. Hydrogen atoms are omitted for clarity. ZIF-25, 96, and 97 showed in ordered conformation.

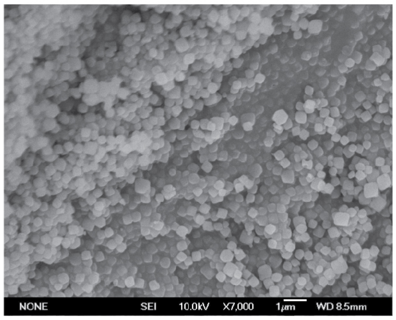

Figure 2) SEM of microcrystalline ZIF-97.

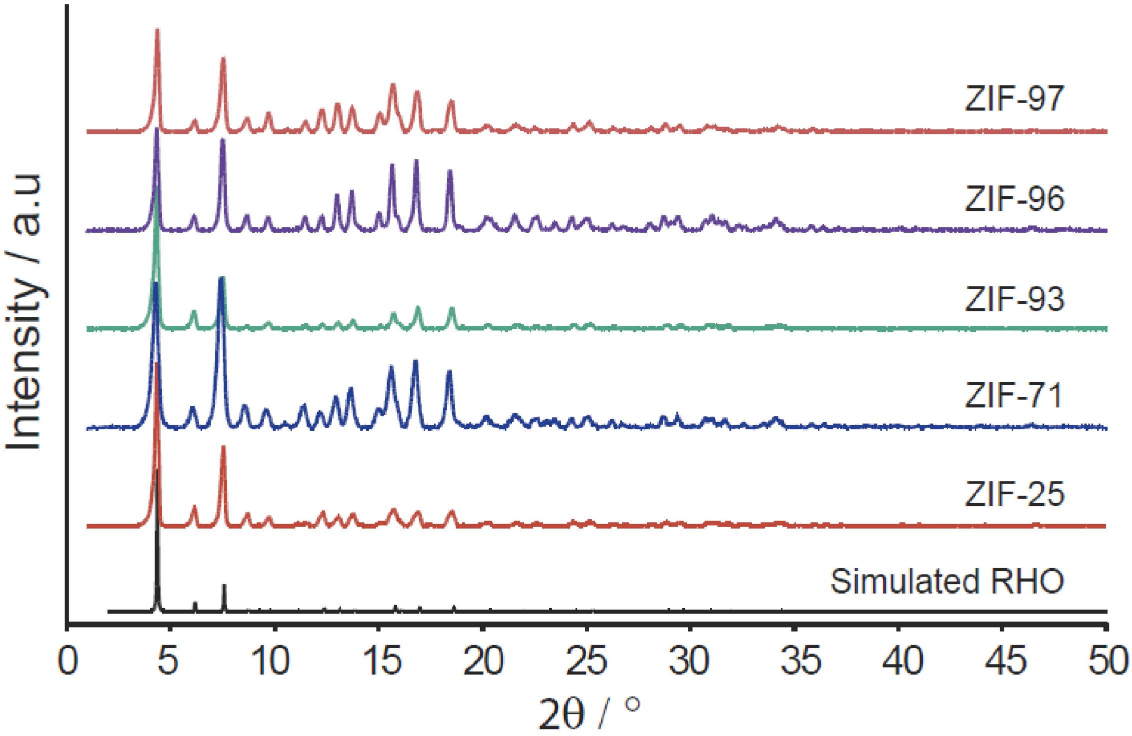

Figure 3) a) PXRD patterns of activated ZIF-25 (blue), 71 (black), 93 (red), 96 (green), and 97 (brown). A simulated RHO pattern from single crystal data (black).

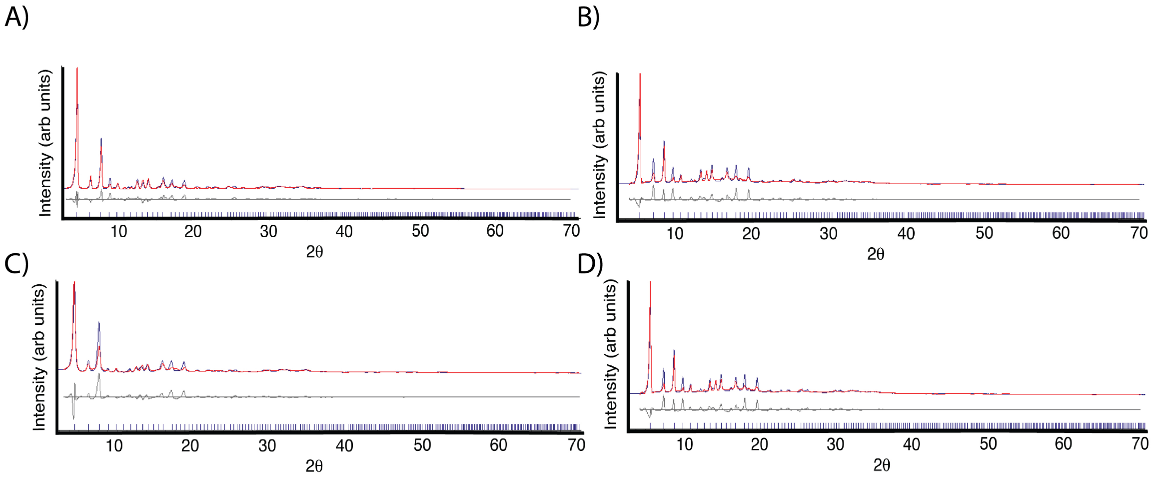

Figure 4) Rietveld refinements of ZIF-25 (A), ZIF-93 (B), ZIF-96 (C), and ZIF-97 (D). Red, experimental pattern; blue, calculated pattern; grey, difference pattern (exp-calc); Bragg peaks, blue.

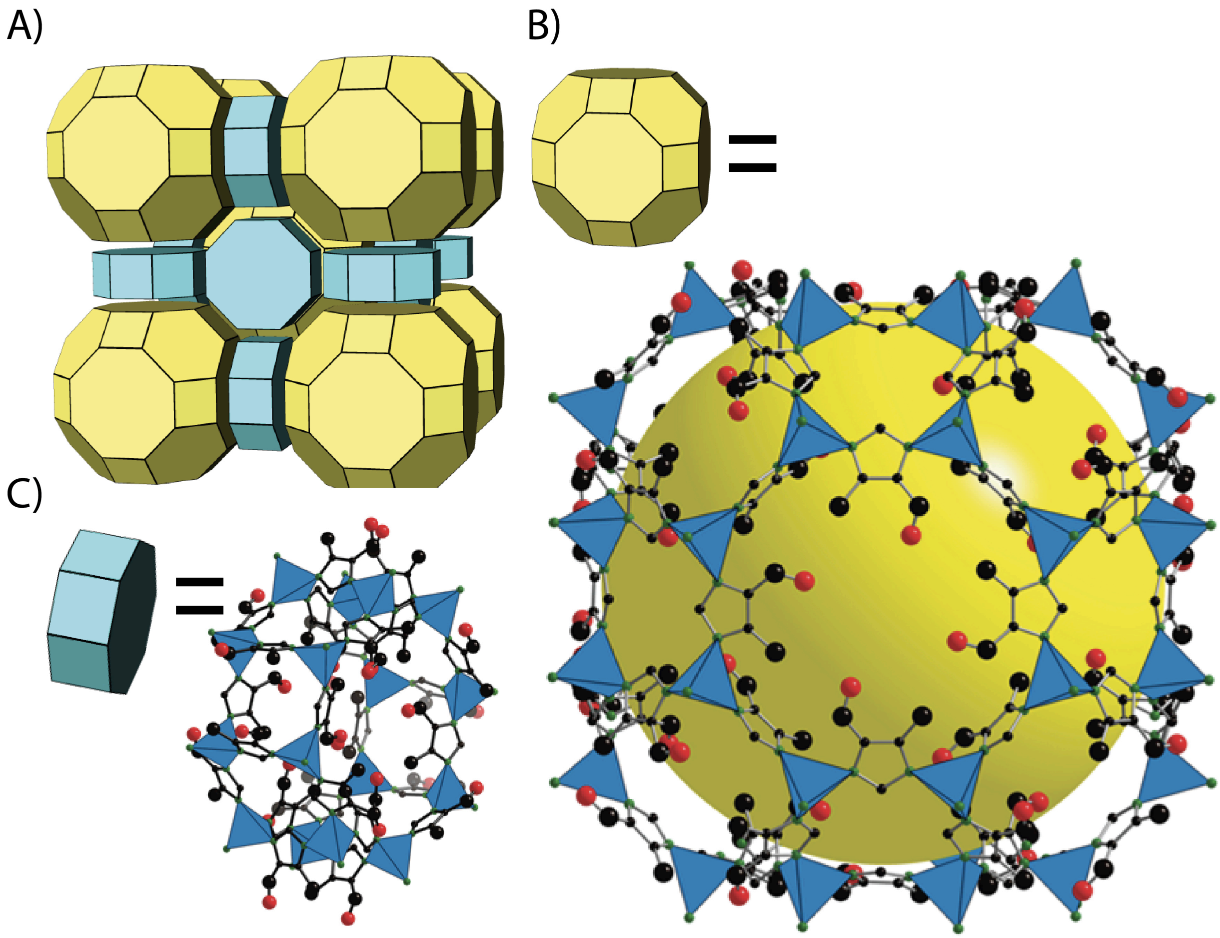

Figure 5) A) The tiling of the RHO structure representing the subdivisions of space (blue and red polyhedra). (B) The structure of one large **lta** cage that is linked together to make the structure of ZIF-93. (C) The **d8r** cage of the **rho** topology. The yellow ball within the cage represents the free space. Atom colors: zinc, blue tetrahedra; carbon, black; oxygen, red; nitrogen, green. Hydrogen atoms are omitted for clarity.

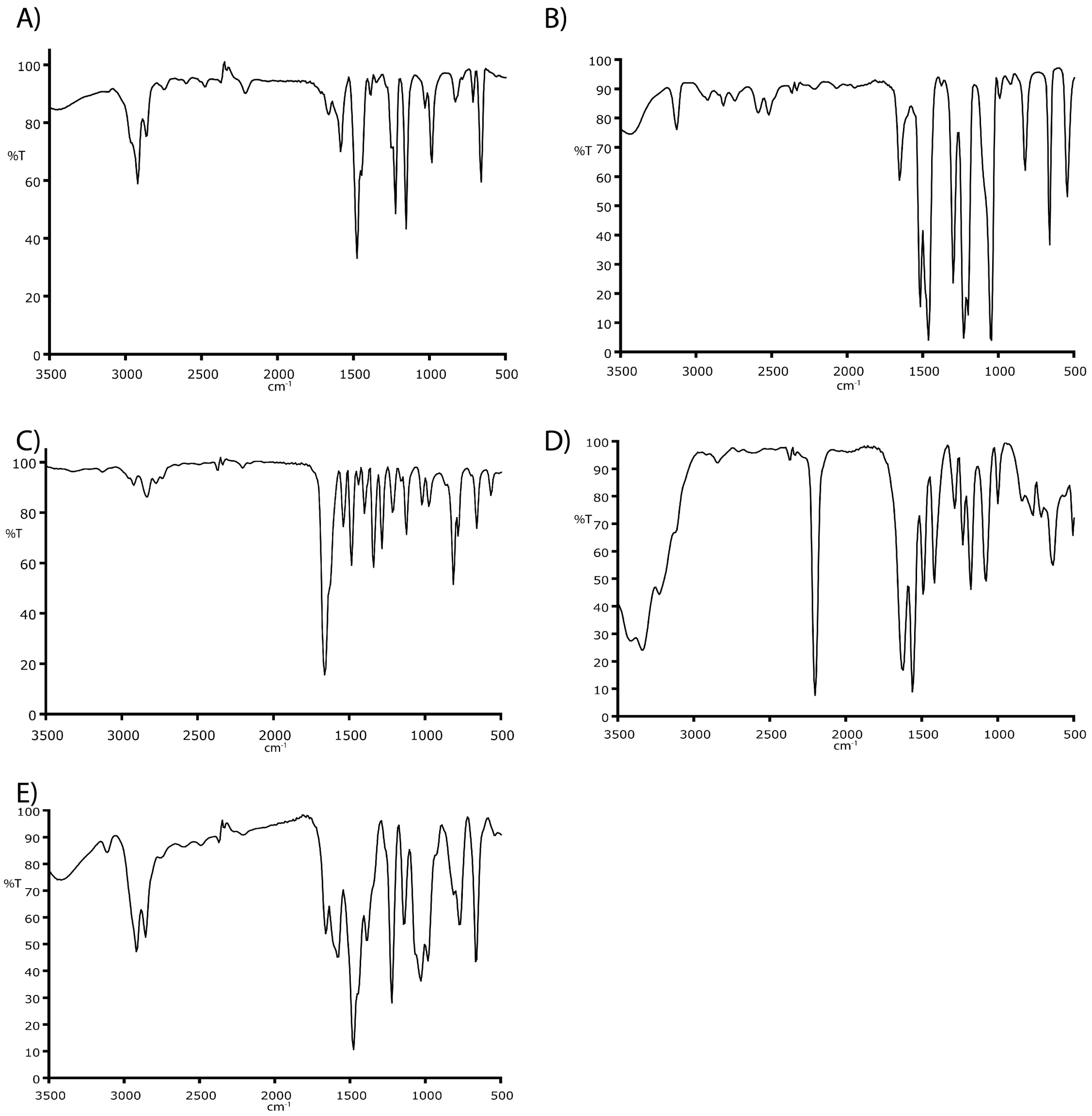

Figure 6) A-E) FT-IR of isoreticular ZIF series, A) ZIF-25, B) ZIF-71, C) ZIF-93, D) ZIF-96, and E) ZIF-97.

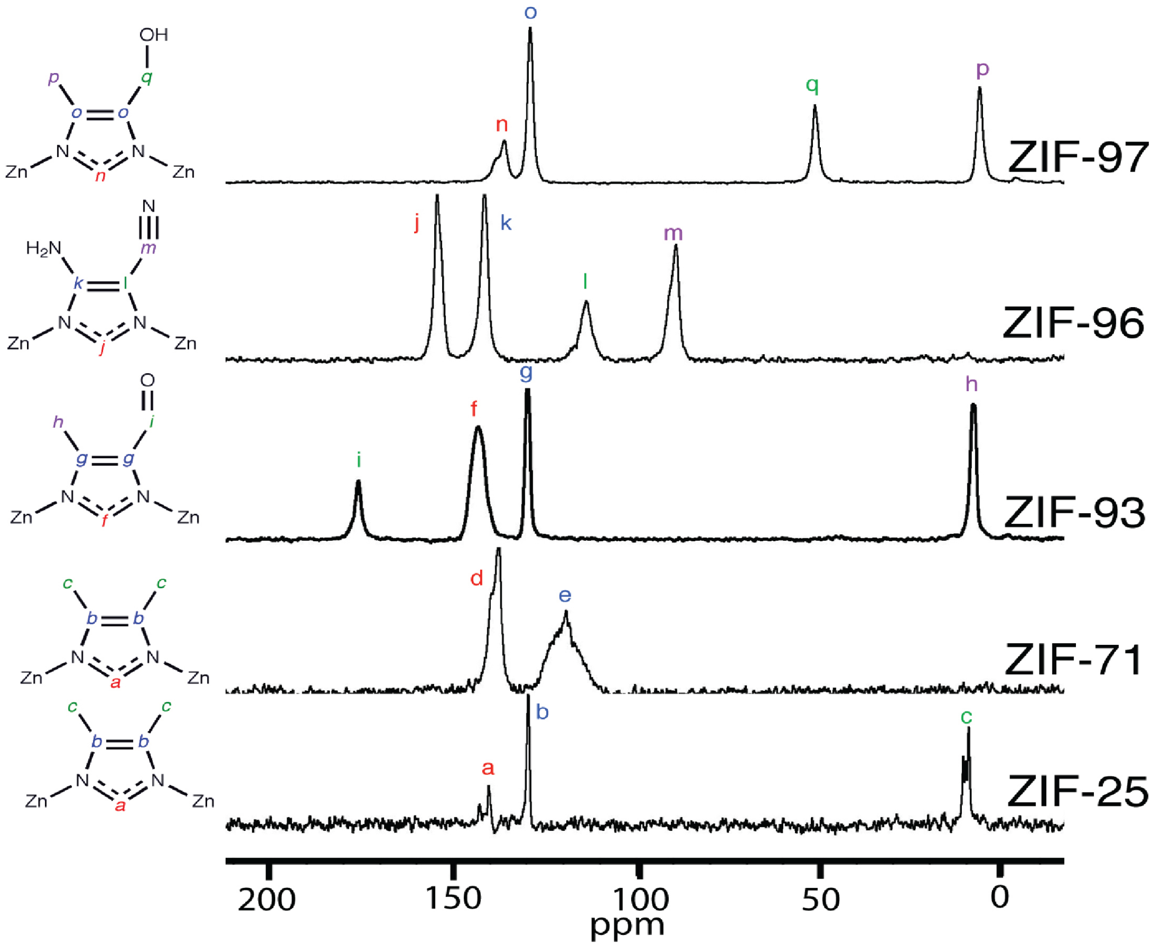

Figure 7) ^{13}C CP/MAS solid state NMR of isoreticular ZIF series.

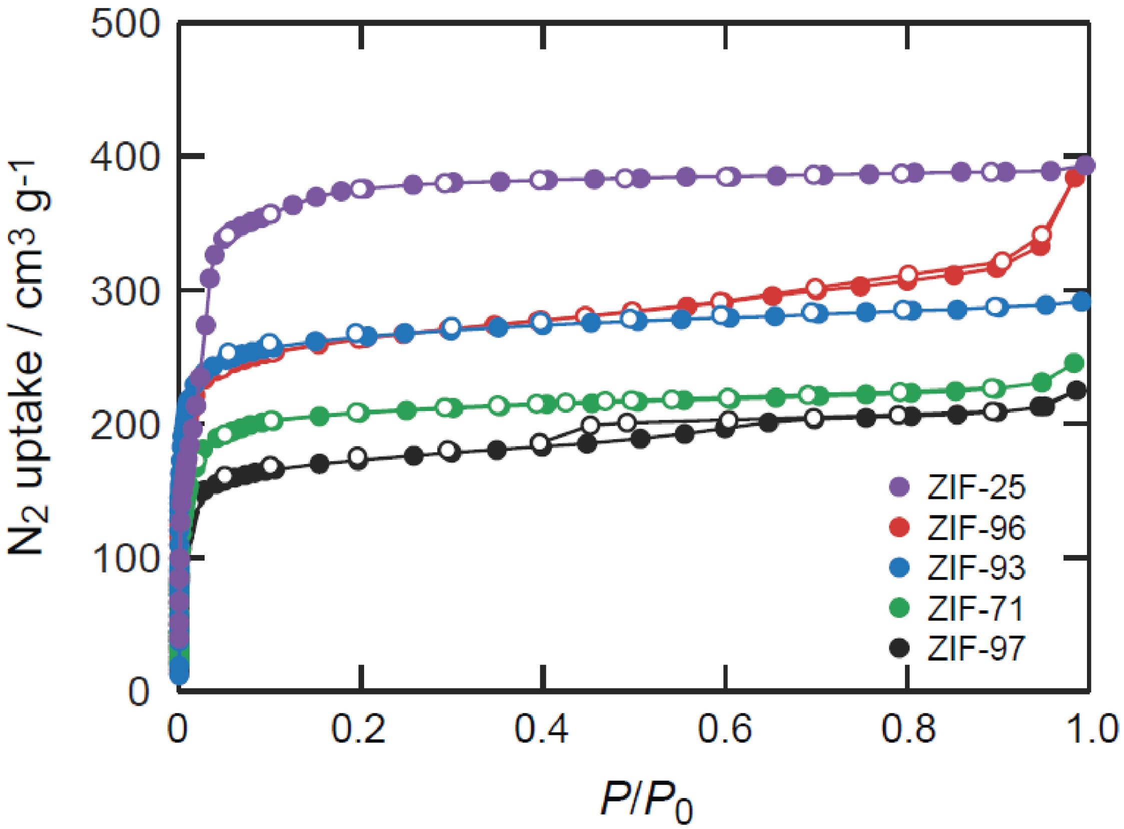

Figure 8) N_2 isotherms at 77 K of isoreticular ZIF series.

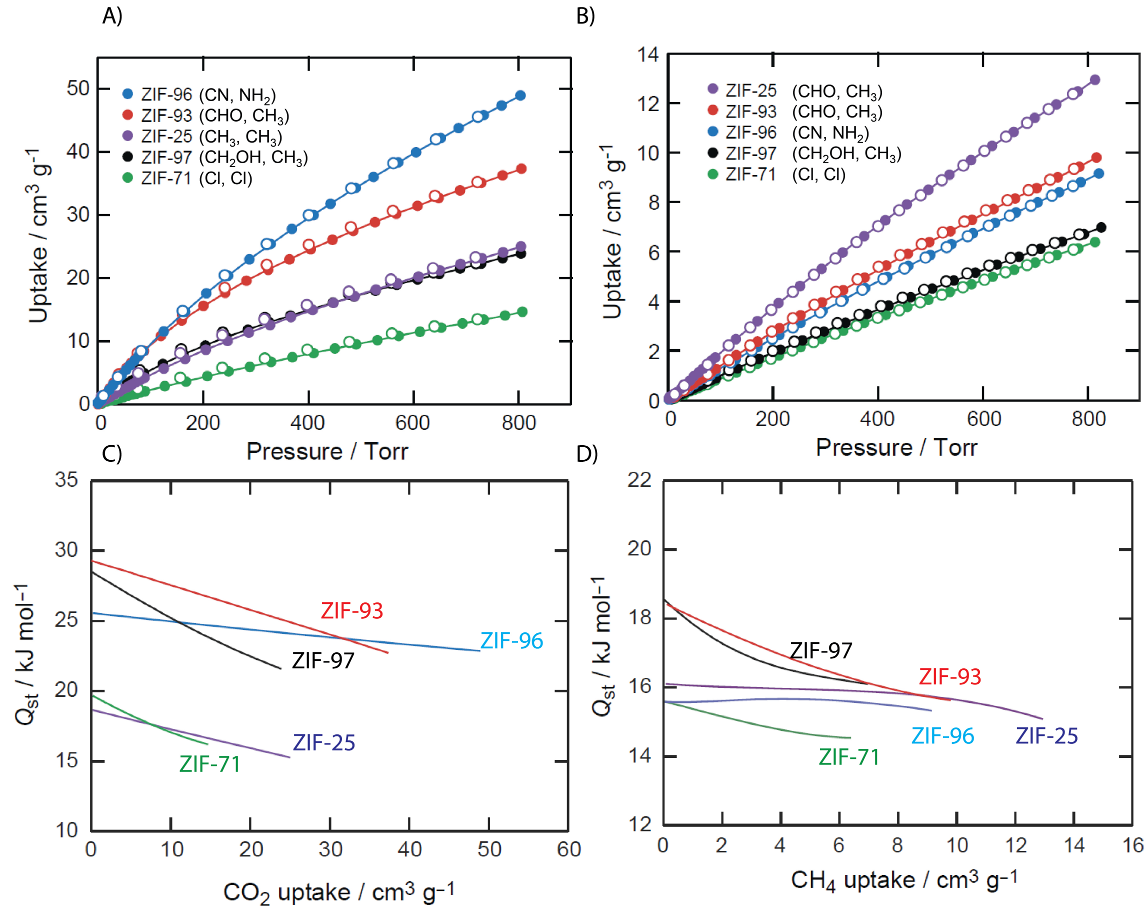

Figure 9) A) CO_2 adsorption at 298 K for isoreticular ZIF series. B) CH_4 adsorption at 298 K for isoreticular ZIF series. C) Calculations of enthalpy of CO_2 adsorption as a factor of loading for isoreticular ZIF series. D) Calculations of enthalpy of CH_4 adsorption as a factor of loading for isoreticular ZIF series.

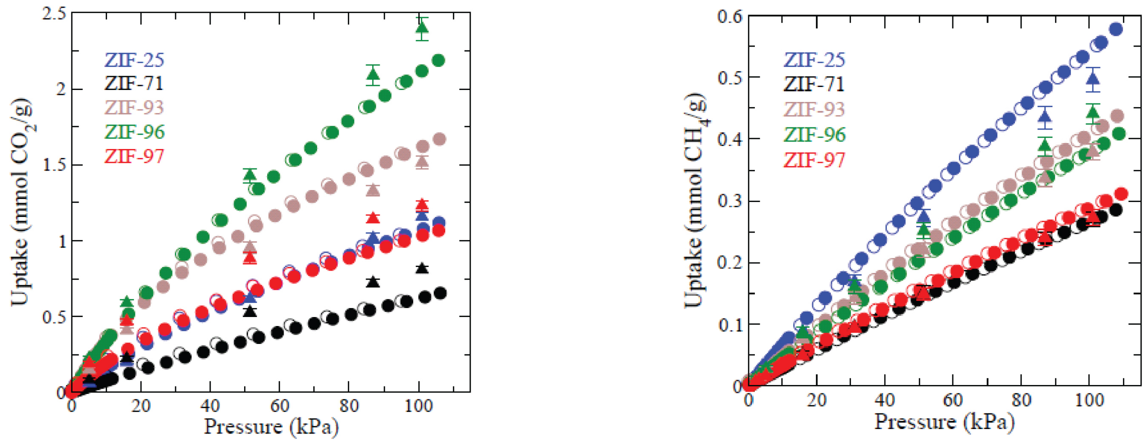

Figure 10) A) CO_2 adsorption at 298 K for isoreticular ZIF series. B) CH_4 adsorption at 298 K for isoreticular ZIF series. Triangles (Theory) circles (experiment)

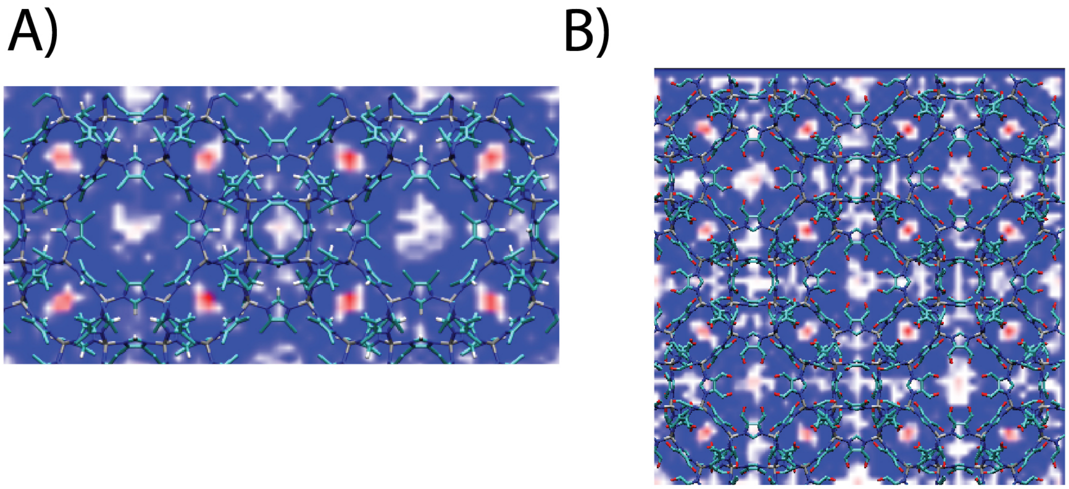

Figure 11) CO_2 charge density maps of CO_2 adsorption in ZIF-71(A) and ZIF-93(B).

Tables

Table 1) Full refinement values for Rietveld analysis of ZIF-25, -93, -96, and -97.

Name	**ZIF-25**	**ZIF-93**	**ZIF-96**	**ZIF-97**
Composition	$Zn_{24}C_{240}H_{336}N_9$	$Zn_{24}C_{240}H_{240}N_{96}O_{48}$	$Zn_{24}C_{192}N_{192}H_{144}$	$Zn_{24}C_{240}H_{288}N_{96}O_4$
Mass Formula (g mol^{-1})	6135	6806.2	6709.6	6903
Crystal system	Cubic	Cubic	Cubic	Cubic
Space Group	*Im*-3*m* (No. 227)	*I*432 (No. 211)	*I*432 (No. 211)	*I*432 (No. 211)
a (Å)	28.688(5)	28.599(10)	28.529(10)	28.601(12)
V (Å^3)	23610(130)	23392(26)	23220(50)	23396(30)
Crystal density (g cm^{-3})	0.856	0.991	0.979	0.999
Number of reflections	213	211	210	210
Number of independent atoms	9	18	18	18

R_p (%)	16.67	15.39	15.66	14.72
R_{wp} (%)	23.94	20.52	22.02	20.50
R_B (%)	11.56	12.09	10.01	13.35
GOF (c^2)	23.73	20.07	20.71	16.51

Table 2) Fractional atomic coordinates for ZIF-25 calculated from *Materials Studio.*

ZIF-25_rho_				
Space Group *Fd*-3*m* (Origin choice 1) $a = b = c = 28.7613(15)$ Å $\alpha = \beta = \gamma = 90^\circ$			Volume 23792 Å^3	
Atom		*X*	*y*	*Z*
Zn1		0.10230	0.39770	0.75000
C2		0.38540	0.0000	0.25240
C3		0.40240	0.02410	0.18600
C4		0.41600	0.05590	0.14710
C5		0.35290	0.15930	0.31910
C6		0.38310	0.19950	0.30580
C7		0.32250	0.32250	0.90830
N8		0.39130	0.03930	0.22890
N9		0.14450	0.20020	0.61680

Table 3) Fractional atomic coordinates for ZIF-93 calculated from *Materials Studio.*

ZIF-93_rho_				
Space Group *I*432(Origin choice 1) $a = b = c = 28.3565(15)$ Å $\alpha = \beta = \gamma = 90^\circ$			Volume 22801 Å^3	
Atom		*X*	*y*	*Z*
Zn1		0.25000	0.60140	0.89860
Zn2		0.25000	0.39590	0.89590
O3		0.39280	0.54230	0.92060
O4		0.08560	0.69990	0.78160
C5		0.24580	0.49900	0.88340
C6		0.31400	0.52290	0.90490
C7		0.35150	0.55370	0.92320
C8		0.31420	0.47420	0.90310
C9		0.35230	0.44190	0.92040
C10		0.17820	0.59350	0.82270
C11		0.18050	0.66070	0.85680
C12		0.19380	0.70010	0.88930
C13		0.14680	0.66210	0.82210
C14		0.11690	0.70290	0.81070
N15		0.27100	0.53840	0.89210
N16		0.27120	0.45920	0.88960
N17		0.14510	0.61970	0.80050
N18		0.20030	0.61760	0.85730

Table 4) Fractional atomic coordinates for ZIF-96 calculated from *Materials Studio.*

ZIF-96_rho_				
Space Group *I*432(Origin choice 1) $a = b = c$ = 28.3564(15) Å $\alpha = \beta = \gamma = 90^\circ$			Volume 22801 Å^3	
Atom		*X*	*Y*	*z*
Zn1		0.25000	0.60361	0.89639
Zn2		0.25000	0.39830	0.89830
C3		0.24644	0.50085	0.88055
C4		0.31189	0.52577	0.90821
C5		0.34463	0.55570	0.93261
C6		0.31167	0.47754	0.90946
C7		0.17847	0.59290	0.82085
C8		0.17688	0.65961	0.85537
C9		0.14235	0.65903	0.82156
C10		0.11051	0.69665	0.80968
N11		0.27085	0.54076	0.89002
N12		0.34456	0.44911	0.93471
N13		0.27083	0.46136	0.89168
N14		0.14306	0.61700	0.79982
N15		0.19967	0.61810	0.85537
N16		0.18803	0.69793	0.88605
N17		0.37101	0.57950	0.95259
N18		0.08485	0.72688	0.80003

Table 5) Fractional atomic coordinates for ZIF-97 calculated from *Materials Studio.*

<table>
<tr><td colspan="5">ZIF-97_rho_</td></tr>
<tr><td colspan="3">Space Group
<i>I</i>432(Origin choice 1)
<i>a</i> = <i>b</i> = <i>c</i> = 28.4319(15) Å
α = β = γ = 90˚</td><td colspan="2">Volume
22983 Å³</td></tr>
<tr><td>Atom</td><td></td><td><i>X</i></td><td><i>Y</i></td><td><i>z</i></td></tr>
<tr><td>Zn1</td><td></td><td>0.25000</td><td>0.60100</td><td>0.89900</td></tr>
<tr><td>Zn2</td><td></td><td>0.25000</td><td>0.39527</td><td>0.89527</td></tr>
<tr><td>O3</td><td></td><td>0.39089</td><td>0.54761</td><td>0.90925</td></tr>
<tr><td>O4</td><td></td><td>0.07187</td><td>0.69599</td><td>0.81578</td></tr>
<tr><td>C5</td><td></td><td>0.24663</td><td>0.49879</td><td>0.88114</td></tr>
<tr><td>C6</td><td></td><td>0.31216</td><td>0.52133</td><td>0.91001</td></tr>
<tr><td>C7</td><td></td><td>0.34868</td><td>0.55017</td><td>0.93453</td></tr>
<tr><td>C8</td><td></td><td>0.31215</td><td>0.47309</td><td>0.89292</td></tr>
<tr><td>C9</td><td></td><td>0.34970</td><td>0.44073</td><td>0.92471</td></tr>
<tr><td>C10</td><td></td><td>0.17847</td><td>0.59342</td><td>0.82270</td></tr>
<tr><td>C11</td><td></td><td>0.18105</td><td>0.66051</td><td>0.85648</td></tr>
<tr><td>C12</td><td></td><td>0.19445</td><td>0.69982</td><td>0.88876</td></tr>
<tr><td>C13</td><td></td><td>0.14787</td><td>0.66215</td><td>0.82128</td></tr>
<tr><td>C14</td><td></td><td>0.11948</td><td>0.70407</td><td>0.80654</td></tr>
<tr><td>N15</td><td></td><td>0.27116</td><td>0.53783</td><td>0.90716</td></tr>
<tr><td>N16</td><td></td><td>0.27082</td><td>0.45860</td><td>0.88939</td></tr>
<tr><td>N17</td><td></td><td>0.14580</td><td>0.61972</td><td>0.80032</td></tr>
<tr><td>N18</td><td></td><td>0.20036</td><td>0.61734</td><td>0.85747</td></tr>
</table>

Table 6) Properties of isoreticular ZIF series.

ZIF #	**-25**	**-71**	**-93**	**-96**	**-97**
Topology	RHO	RHO	RHO	RHO	RHO
Formula	$Zn(C_5N_2H_7)_2$	$Zn(C_3N_2Cl_2H)_2$	$Zn(C_5N_2OH_5)_2$	$Zn(C_5N_4H_3)_2$	$Zn(C_5N_2OH_7)_2$
Surface area (m^2/g)	1110	651	864	960	564
Density (g/cm^3)	0.856	1.183	0.991	0.974	0.997
Pore size (Å)	19.6	16.4	17.9	15.6	18.7
Initial Q_{st} CH_4 Experimental (Simulated)	16.1 (20.6)	15.6 (17.7)	18.5 (23.0)	15.6 (18.2)	18.5 (21.8)
Initial Q_{st} CO_2 Experimental (Simulated)	18.7 (16.9)	19.7 (22.7)	29.3 (28.2)	25.6 (29)	28.5 (24.7)

References

1) Quadrelli, R.; Peterson, S. Energy Policy, **2007**, *35*, 5938.

2) Cejka, J.; Corma, A.; Zones, S. Zeolites and Catalysis: Synthesis, Reactions and Applications; Wiley-VCH: Weinheim, Germany, **2010**.

3) Rochelle, G. T. Science **2009**, *325*, 1652.

4) Phan, A.; Doonan, C.; J. Uribe-Romo, F.; Knobler, C. B.; O'Keeffe, M.; Yaghi, O. M. *Acc. Chem. Res*, **2009**, 43, 58-67.

5) Park, K. S.; Ni, Z.; Cote, A. P.; Choi, J. Y.; Huang, R. D.; Uribe-Romo, F. J.; Chae, H. K.; O'Keeffe, M.; Yaghi, O. M. *Proc. Natl. Acad. Sci. U.S.A.* **2006**, *103*, 10186.

6) Banerjee, R.; Furukawa, H.; Britt, D.; Knobler, C.; O'Keeffe, M.; Yaghi, O. M. *J. Am. Chem. Soc.*, **2009**, *131*, 3875-3877 b) Wang, B.; Côté, A. P.; Furukawa, H.; O'Keeffe, M.; Yaghi, O. M. *Nature*, **2008**, *453*, 207-211

7) Banerjee, R.; Phan, A.; Wang, B.; Knobler, C.; Furukawa, H.; O'Keeffe, M.; Yaghi, O. M. *Science*, **2008**, *319*, 939-943

8) Materials studio version 5.0, 2009, Accelrys Software Inc.

9) A. K. Rappe, C. J. Casewit, K. S. Colwell, W. A. Goddard-III, W. M. Skiff. *J. Am.Chem. Soc*. **1992,** *114,* 10024-10035.

10) TOPOS version 3.0 Bruker, 2001.

Chapter Seven

Conclusions

Porous materials have been used for thousands of years. The Egyptians were one of the first groups of people to use porous adsorbants for medical applications. Within the last fifty years activated carbons and zeolites have been extensively studied, finding applications in water filters and household detergents, respectively. MOFs, a recent addition to the field of porous materials, are highly ordered crystalline frameworks constructed from organic links and metal oxide units. MOFs offer controlled domains on the angstrom and nanometer level, and they can be appended with many different functionalities. Control of pore size and function will allow this new class of porous materials to be used in many new applications, including catalysis, gas adsorption, and separations. To achieve the best use of these new materials, MOFs and ZIFs, extensive studies of stability and functionality must be carried out, and desirable attributes must be recognized. In this thesis attempts to enhance functionality and stability of a range of MOFs are described; a broader understanding of structure and function will enable the most efficient use of these materials.

To expand the applications of MOFs and ZIFs, one must overcome the limitations of solvothermal synthesis. Solvothermal synthesis only allows the incorporation of certain functionalities and metal oxide units within the MOF; these metal centers are often pivotal to structure. Unlike other porous materials, MOFs offer highly ordered domains, which can be decorated with certain organic functionalities. These highly ordered porous domains decorated with organic functionalities make them ideal for the study of postmodification. Postmodification utilizes extensive knowledge of small molecule chemistry, applying this chemistry to MOFs at the heterogeneous interface between the MOFs and the solution. Postmodification has been extensively evaluated in this thesis; several key aspects of the MOF have been considered including pore size, MOF stability, and pore volume.

ZIFs were selected for the first investigation of postmodification because of their high chemical stability, which would allow a greater range of organic reactions to be carried out in a topotactic manner. Two reactions were chosen to modify the aldehyde functionality of ZIF-90, imine formation and reduction of the aldehyde to the corresponding alcohol. These postmodification reactions proceeded in high yield with retention of crystallinity. However, one key limitation was observed; during imine formation the pores of the ZIF became blocked. This pore blockage was due to the small pore apertures of the ZIF, limiting the size of the organic functionality that could be incorporated. Therefore the method was modified; the postmodification of a MOF with large pores was evaluated, UMCM-1-NH_2.

When open metal sites are incorporated into MOFs they offer exceptional gas adsorption and catalytic properties; for example, the open metal sites in MOF-74 greatly enhance CO_2 adsorption in this MOF. However, most metal sites are saturated within the MOF with tightly bound organic units; the discovery of open metal site MOFs often depends on luck, rather than design. Metalation by postmodification offers an alternative route to the incorporation of new metal centers into MOFs. Metalation produced bimetallic systems, in which one metal offers structure function and the second metal can act to enhance catalytic or gas adsorption activity within the MOF. Postmodification of UMCM-1-NH_2 was evaluated. The large pores of this MOF are suitable for metalation. A two-step postmodification process was selected to successfully achieve metalation; imine formation is followed by metalation. Metalation proceeded in a quantititative manner with retention of porosity. However, the PXRD data showed a loss of long-range order indicating the limits in chemical stability of the zinc-based MOF. The studies of ZIFs and UMCM-1-NH_2 pointed out the need for large pored chemically stable MOFs.

In 2008 the first zirconium-based MOFs, UiO-66, were reported, offering pore sizes up to one nanometer in size coupled with high chemical stability. To make these zirconium-based MOFs suitable for postmodification we functionalized them with amine functionalities, producing a MOF with high chemical stability and large pores. These MOFs were postmodified with acetylaldehyde which led to hemiaminal and aziridine functionalities isolated in the pores of UiO-66-A, with retention of porosity and crystallinity.

The discovery of new MOFs remains paramount in this field, especially in the area of chemically stable functionalizable MOFs. Therefore, the design of new MOFs based on zirconium metal oxide units was addressed. To form this new zirconium MOF an organic unit with four points of extension, containing predefined metal binding sites was employed. By combining this organic unit with zirconium sources, three new MOFs were isolated, MOF-525, MOF-545, and MOF-565, with three new zirconium MOF topologies, **ftw**, **csq**, and **shp**, respectively. The synthesis of these materials greatly expanded our knowledge of zirconium MOFs; three new topologies and two new metal oxide units were discovered. In addition, these MOFs broke records for surface area and pore sizes in zirconium MOFs. These MOFs successfully incorporated porphyrin sites which were quantitatively metalated by pre- and post-metalation, leading to potential applications in catalysis. Unlike ZIF-90 and UMCM-1-NH_2, these frameworks were neither blocked nor damaged during the metalation reaction, maintaining crystallinity and porosity.

Throughout this thesis new techniques in synthesis and characterization of MOFs and ZIFs have been described. In the synthesis of new ZIFs, room temperature techniques were developed to form frameworks that did not form by solvothermal methods. In addition, methods to determine crystals structures of microcrystalline powders were undertaken, including structure determination from modeling and refinement of structures based on topological information. Furthermore, techniques for characterizing postmodification reactions were developed, EXAFs provided insight about transformation around metal centers and ^{15}N solid state NMR provided information about organic transformation around nitrogen centers.

For MOFs and ZIFs to fully realize their potential their characteristics must be known. As highly porous structures with surface areas regularly exceeding 1000 m^2/g, MOFs and ZIFs are commonly assessed for their gas adsorption properties. Gas adsorption was investigated in a series of **rho** ZIFs, to gain understanding of the effect of functionality on gas adsorption. By carrying out experimental measurements coupled with computations we showed that functionality is a key to enhancing CO_2 adsorption. CO_2 adsorption is enhanced through direct interactions between CO_2 and the functionalities that decorate the pores; it is important to know whether multiple functionalities would further enhance gas adsorption. Furthermore, we investigated ammonia adsorption in a series of chemically stable zirconium MOFs; ammonia is a gas that has led to the breakdown of other MOFs. Zirconium-based MOFs with high chemical stability were shown to retain crystallinity and porosity upon reversible ammonia adsorption, highlighting the advantage of these chemical stable MOFs.

The discovery of MOFs over fifteen years ago was a significant step forward for porous materials, offering highly ordered crystalline domains, which can be functionalized. This ability to increase function in MOFs was further realized by the potential to carry out postmodification of MOFs, overcoming the limitations of solvothermal synthesis. The postmodification of ZIF-90, UMCM-1-NH_2, and UiO-66-A, offers techniques which can be applied to a wide range of MOFs and ZIFs. To produce frameworks suitable for application via postmodification, one must consider chemical stability of the framework, pore size, and pore volume.

Most exciting was the discovery of MOF-525, MOF-545, and MOF-565; these zirconium-based MOFs combine large pores with high chemical stability. The study of zirconium-based MOFs is truly in its infancy, but these are a crucial set of frameworks because of their high chemical stability and variable pore metrics. The discovery of new zirconium-based MOFs will bring exciting developments to MOF chemistry allowing the realization of further applications. In addition, the potential applications of MOF-525, MOF-545, and MOF-565 are still to be realized, as they contain porphyrin sites, which can be freely metalated. The incorporation of porphyrins into MOFs has been fully realized in this series of zirconium-based MOFs, which combine high surface area and large pore sizes. Homogeneous porphyrin catalysis is a promising subject, which can now be investigated in a heterogeneous reaction between framework and solution.

MOFs and ZIFs are a rapidly expanding group of materials, and many chemists are working on the synthesis and applications of frameworks worldwide. The results and conclusion described in this thesis can be applied to a wide series of MOFs and ZIFs. By considering postmodification and framework stability, one may expect to see frameworks realize heir full potential more quickly.